Stability of a two-volume MRxMHD model in slab geometry

Li Huey Tuen

A thesis submitted for the degree of
Master of Philosophy
of The Australian National University

2 August 2017

Except where otherwise indicated, this thesis is my own original work.

Li Huey Tuen
2 August 2017

Acknowledgments

> No man is an island, entire of itself.
>
> *John Donne*

This work could not have been completed without the guidance of my supervisors Associate Professor Matthew Hole and Emeritus Professor Robert Dewar who have been extremely helpful and and supportive throughout my time here at ANU.

Here I record my everlasting gratitude for their valuable insights, their aid with getting my ideas across in a succinct manner, introducing me to researchers across the globe, and providing advice about life and future goals in general. Dr. Graham Dennis provided the idea for this thesis and generously dispensed much-needed feedback through email correspondence.

The other members of our research group, Dr. Brett Layden, George Bowden, Sebastian Cox and Adelle Wright have my gratitude as well for answering mundane physics questions, entertaining my stranger ones, and generally being fantastic colleagues. Sorry for barging into your offices all the time. Special thanks to Zhisong Qu for being an unofficial supervisor and carpool buddy.

I have achieved far more than I could have expected when I first started this research, met many amazing people and conversed with brilliant minds. While I cannot list all the individuals who fall into these categories, I am most thankful for their contribution to my life experiences over the past two years.

There are a few puns included in this Thesis, helpfully contributed by our research group members; I hope you enjoy them as much as we have groaned at them.

Abstract

Ideal MHD models are known to be inadequate to describe various physical attributes of a toroidal field with non-continuous symmetry, such as magnetic islands and stochastic regions. Motivated by this omission, a new variational principle MRXMHD was developed; rather than include an infinity of magnetic flux surfaces, MRxMHD has a finite number of flux surfaces, and thus supports partial plasma relaxation. The model comprises of relaxed plasma regions which are separated by nested ideal MHD interfaces (flux surfaces), and can be encased in a perfectly conducting wall. In each region the pressure is constant, but can jump across interfaces. The field and field pitch, or rotational transform, can also jump across the interfaces. Unlike ideal MHD, MRxMHD plasmas can support toroidally non-axisymmetric confined magnetic fields, magnetic islands and stochastic regions.

In toroidally non-axisymmetric plasma, the existence of interfaces in MRxMHD is contingent on the irrationality of the rotational transform of flux surfaces. That is, the KAM theorem shows that invariant tori (flux surfaces) continue to exist for sufficiently small perturbations to an integrable system (which describes flux surfaces), provided that the rotational transform is sufficiently irrational. Building upon the MRxMHD stability model, we study the effects of irrationality of the rotational transform at interfaces in MRxMHD on plasma stability.

We present an MRxMHD equilibrium model to investigate the effects of magnetic field pitch within the plasma and across the aforementioned flux surfaces within a chosen geometry. In this model, it is found that the 2D system stability conditions are dependent on the interface and resonant surface magnetic field pitch at minimised energy states, and the stability of a system as a function of magnetic field pitch destabilises at particular values of magnetic field pitch. We benchmark the treatment of a two-volume system, along with the calculations for background and perturbed magnetic fields to existing cylindrical working.

An expression is formulated for the stability eigenvalues by creating a model for the slab geometry system. The eigenvalues for system stability at a minimum energy state are found to depend upon the rationality of the magnetic field pitch at resonant surfaces. Various system parameter scans are conducted to determine their affect upon system stability and their implications. While tearing instabilities exist at low order rational resonances, investigating the instability of high-order rationals requires study of pressure-driven instabilities.

Contents

Chapter 1

Overview

Plasma is defined as the fourth state of matter; solid, liquid, gas and plasma, making up 99.9% of our universe. Objects such as the Sun generate energy via nuclear fusion at its core from the vast amounts of hydrogen stored within it. While nuclear fusion occurs due to quantum tunnelling in the large mass of the Sun [19], scientists have been utilising magnetic fields in confinement devices to study the physics of plasmas, from fusion technology on Earth to astrophysical systems. Through nuclear fusion, a viable, clean, and limitless, source of energy has been the driving goal of fusion energy.

1.1 Ideal MHD, Taylor Equilibria, and MRxMHD

In the 21st century, the main toroidal magnetic confinement fusion devices are the tokamak[1], which is an axisymmetric torus, and the stellarator which allows 3-dimensional and non-axisymmetric magnetic fields that are used to confine the plasma within. While the stellarator has benefits over the tokamak configuration, such as the lack of a toroidal plasma current and its associated instabilities, it introduces a higher level of complexity in terms of construction and magnetic topology [20].

Fig. 1.1 shows the differently shaped flux surfaces within both devices, and so stellarators require additional mathematics and physics than tokamaks for analytical study of their magnetic topology. Nested flux surfaces, island chains and regions of chaos within the plasma where flux surfaces do not form may exist due to toroidal magnetic fields without symmetry [20], as exhibited by this stellarator cross-section in Fig. 1.2. Flux surfaces are magnetic surfaces tangential to magnetic fields, and chains of nested magnetic surfaces each with its own magnetic axis are called magnetic islands [4].

Ideal MHD theory allows us to analytically study the macroscopic behaviour of plasma. The fundamental idea in ideal MHD is that the magnetic fields are frozen in place; breakage and reconnection of field lines is prohibited. While this is not a perfect representation of the nature of plasmas, it allows valid mathematical analysis across a wide range of plasma phenomenon such as kink instabilities. Utilising Maxwell's equations and the equations of gas dynamics, a set of ideal MHD equations are obtained [15]:

---

[1] Reverse Field Pinch (RFP) experiments allow magnetic field reversal at a certain internal point, and are physically similar to tokamaks [3].

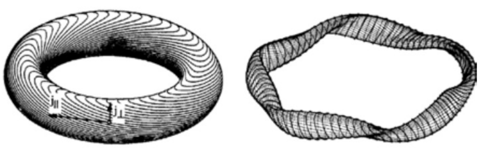

Figure 1.1: Flux surfaces of a tokamak on the left and stellarator on the right. HARTMANN, D., 2004. Stellarators. *Fusion Science and Technology*, 45, 2T (2004), 64–76.

$$
\begin{aligned}
&\frac{\partial \rho}{\partial t} + \nabla \cdot (\rho \boldsymbol{v}) = 0 && \text{continuity,} && (1.1)\\
&\rho(\frac{\partial \boldsymbol{v}}{\partial t} + \boldsymbol{v} \cdot \nabla \boldsymbol{v}) + \nabla p - \frac{1}{\mu_o}(\nabla \times \boldsymbol{B}) \times \boldsymbol{B} = 0 && \text{momentum,} && (1.2)\\
&\nabla \cdot \boldsymbol{B} = 0 && \text{solenoidal constraint,} && (1.3)\\
&\frac{\partial p}{\partial t} + \boldsymbol{v} \cdot \nabla p + \gamma p \nabla \cdot \boldsymbol{v} = 0 && \text{internal energy,} && (1.4)\\
&\frac{\partial \boldsymbol{B}}{\partial t} - \nabla \times (\boldsymbol{v} \times \boldsymbol{B}) = 0 && \text{Faraday,} && (1.5)\\
&\boldsymbol{E} + \boldsymbol{v} \times \boldsymbol{B} = 0 && \text{Ohm.} && (1.6)
\end{aligned}
$$

Frequencies, or eigenvalues, from the conservation of energy at equilibrium using ideal MHD can inform about the stability of the system with a choice of initial perturbation, and provides information on marginal stability.

Resistivity has been excluded from the above equations; Eq. (1.6) shows perfect conductivity. The inclusion of resistivity modifies the following equations from Eq. (1.4) and Eq. (1.6):

$$
\begin{aligned}
\frac{\partial p}{\partial t} + \boldsymbol{v} \cdot \nabla p + \gamma p \nabla \cdot \boldsymbol{v} &= (\gamma - 1)\eta \left|\boldsymbol{j}^2\right|, && (1.7)\\
\boldsymbol{E} + \boldsymbol{v} \times \boldsymbol{B} &= \eta \boldsymbol{j}. && (1.8)
\end{aligned}
$$

In 1974, Taylor [38] published a new theory explaining the spontaneous existence of reversed fields in toroidal plasmas in terms of plasma relaxation; after a fusion device is initiated, the plasma is turbulent and after a certain timescale, the plasma enters a relaxed state in which the energy of the system is at a minimum with certain boundary conditions.[2] Following this theory, plasma can only relax via reconnection of field lines which requires non-zero resistivity in the plasma. For a plasma surrounded by a perfectly conducting surface, the sum of magnetic energy, M and overall magnetic helicity, K,

$$
\begin{aligned}
M &= \int \frac{\boldsymbol{B} \cdot \boldsymbol{B}}{2\mu_o} \, d^3\tau, && (1.9)\\
K &= \int \boldsymbol{A} \cdot \boldsymbol{B} \, d^3\tau = \int \frac{1}{2}\mu H \, d^3\tau, && (1.10)
\end{aligned}
$$

---

[2] Without a defined boundary condition, the minimum energy in a system would be zero, i.e. no plasma, only vacuum exists.

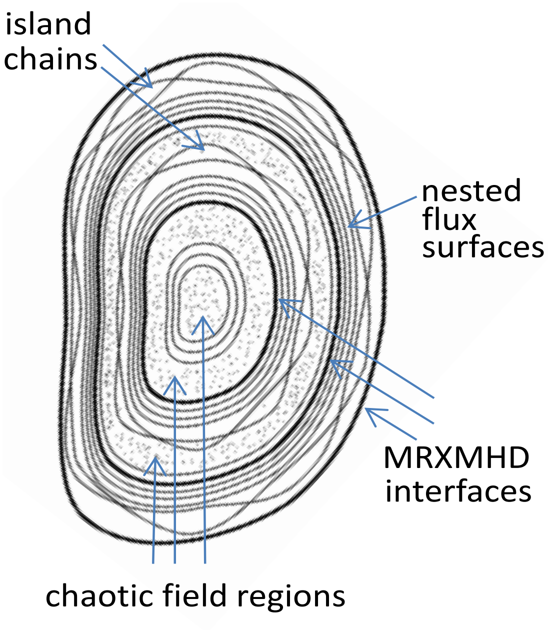

Figure 1.2: Characteristics of flux surfaces and various regions in a stellarator.

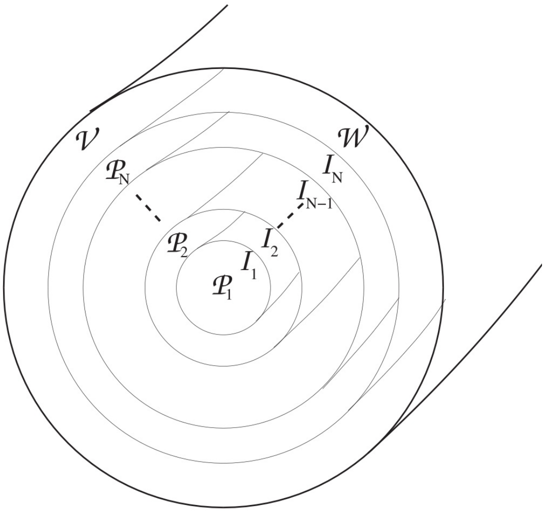

Figure 1.3: Cylindrical model of a tokamak with concentric flux tubes, with perfectly conducting wall W, ideal MHD barriers I_i, plasma regions P_i and the vacuum region V. Hole, M.; Hudson, S.; and Dewar, R., 2007. Equilibria and stability in partially relaxed plasma-vacuum systems. *Nuclear Fusion*, 47, 8 (2007), 746.

are minimised with the total helicity being invariant, with $\boldsymbol{B} = \nabla \times \boldsymbol{A}$, Lagrange multipler μ, magnetic helicity in each region H, $\boldsymbol{A}$ the vector potential, and $d^3\tau$ for a volume element. Equilibrium is satisfied with the Beltrami equation, $\nabla \times \boldsymbol{B} = \mu \boldsymbol{B}$; for a vacuum region, helicity, H is nonexistent and so $\mu = 0$. A general solution to the Beltrami equation can be derived for an axisymmetric system [6], which provide expressions for $\boldsymbol{B}$ in the poloidal and toroidal direction, or in this thesis, the y and z directions.

Taylor's minimum energy principle, or variational principle, demonstrated that system stability is dependent upon the relaxed state of the plasma, and this was extended [21, 25, 36] to a plasma-vacuum system. This work resulted in a set of equations with a solution of an eigenvalue problem which is utilised in this thesis. From this eigenvalue, λ, the stability of a plasma-vacuum system can be determined by a sign difference; positive λ signifies system stability, while negative λ implies instabilities exist. In this work, nonlinear evolution of unstable states, beyond the linear secular growth phase, is not addressed. That is, we do not address or identify the state to which an unstable equilibrium evolves.

Instead of assuming continually nested flux surfaces for ideal MHD models, a finite number of flux surfaces are assumed to exist in a relaxed plasma system. With the origins of relaxed plasma theory now clarified, we introduce the Multi-Region Relaxed Magnetohydrodynamics (MRxMHD) theory [21]. It is based on a generalisation of Taylor's relaxation principle, whereby total system energy is minimised subject to a finite number of magnetic flux, helicity, and thermodynamic constraints [9]. Fig. 1.3 shows the number of concentric flux surfaces are finite, where pressure is constant in each concentric flux tube, and pressure jumps are across interfaces. MRxMHD theory has been shown to converge back to ideal MHD when the amount of flux surfaces becomes infinite [9] and supports the use of the theory as a tool to understand plasma-vacuum systems in a minimum-energy state. It also provides the flexibility of increasing or decreasing plasma regions as necessary for analysis, and provides the capability to describe 2D and 3D MHD structures such as island chains and chaotic field regions, as described in Fig. 1.2.

We further concentrate our work onto the field lines and wave vectors. Field line bending is concluded to be a driving force for instabilities around rational magnetic field lines in many experimental plasma systems, i.e. internal kink modes and ballooning modes [14]. In 2D tokamaks, equilibrium flux surfaces are guaranteed and fill the plasma volume; in 3D stellarators (or real-life tokamaks), equilibrium flux surfaces can exist if the field line is sufficiently irrational[3] and survive perturbations [32].

---

[3] Irrationals, or rationality of field lines are in the context of rational numbers; see Sections 3.5.3 - 3.6.

1.2 Thesis Outline

This thesis aims to utilise Taylor's method of energy relaxation via the MRxMHD theory in terms of system stability, and its dependence, if any, on the rotational transform rationality of flux surfaces. The twist of field lines in toroidal magnetic system confinements are known as magnetic rotational transforms, shown in Fig. 1.4. Field lines with rational rotational transforms traverse around a given system, ultimately 'biting its own tail' and are of finite length. Field lines with irrational rotational transforms are of infinite length as they will never arrive at its original point as it travels around its confinement system.

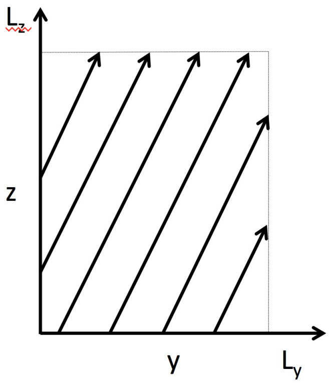

Figure 1.4: Field lines traversing a physical region where L_y and L_z are periodic lengths in the y and z directions. Depending on its rotational transform, each line may or may not meet its original starting point in the confinement system.

The motivation of the work presented here starts with the understanding that much of the literature in plasma theory and experimental fusion exhorts the reader to use rotational transforms at interfaces that are of an irrational nature, as these irrational surfaces are most resistant to perturbations. The work of McGann et al. [32] is one such study, using a Hamiltonian formulation in which the coordinates are free variables, allowing study of 3D systems such as stellarators as a simpler 2D system without losing information of the original non-axisymmetric configuration.

In the Kolmogorov-Arnold-Moser (KAM) theory [8], flux surface existence is dependent upon the irrationality of the rotational transforms at particular surfaces. However, this theory only applies for non-axisymmetric 3D systems in which the flux surfaces are non-integrable, i.e. the magnetic field line continuously loops around the axis of the 3D system without encountering its starting point. Therefore, a direct comparison to a simpler axisymmetrical Euclidean space (without any mapping of configuration space[4], or phase space[5]) is not possible as the fields are now integrable.

The Stepped Pressure Equilibrium Code (SPEC) [1] which is based on MRxMHD provides a solution with individual flux surfaces within a chosen system equilibria, as shown in Fig. 1.5. The effects of rotational transform on flux surfaces and pressure gradients can be studied in great detail. McGann et al. [32] which used SPEC and the pressure jump condition of MRxMHD:

$$\left[\left[p+\frac{B^2}{2}\right]\right]=0, \tag{1.11}$$

---

[4] Poloidal and toroidal directions.

[5] 4-dimensional.

found that the flux surfaces do indeed require a measure of irrationality to not be destroyed by perturbations in 3D systems, thus being consistent with KAM theory, but this work was done by investigating the robustness of flux surface to perturbations locally around a fixed flux interface. While this work can be extended to multiple interfaces, it does not utilise the minimisation of energy as postulated by Taylor [39], but studies flux surface formation in equilibrium subject to a stepped pressure jump condition across the interface.

Another body of work by Loizu et al. [30] has shown that SPEC requires a rotational transform discontinuity to calculate MRxMHD equilibria in a slab geometry in both pressureless and nonzero pressure scenarios. Magnetic islands around a resonant rational surface vanished as the rotational transforms ι, on the internal surfaces around the magnetic island approached the resonant value $\iota = 0$ and retrieving the ideal MHD limit. Interestingly, the value of ι vanishes (for pressureless scenarios) or becomes discontinuous (for nonzero pressure scenarios) when the magnetic island has completely dissappeared.

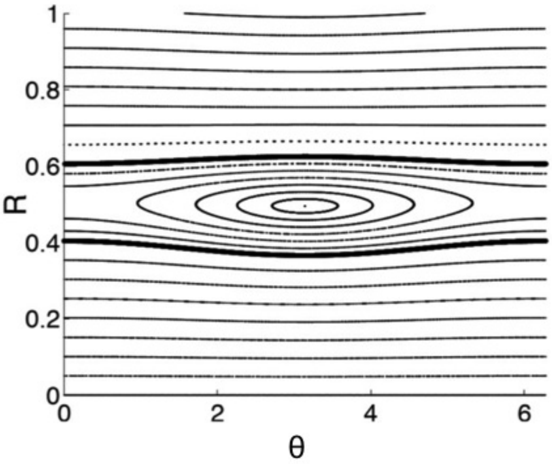

Figure 1.5: Poincaré plot generated by SPEC for a 3 plasma volume system shows the existence of a magnetic island. Loizu, J.; Hudson, S.; Bhattacharjee, A.; and Helander, P., 2015. Magnetic islands and singular currents at rational surfaces in three-dimensional magnetohydrodynamic equilibria. *Physics of Plasmas (1994-present)*, 22, 2 (2015), 022501.

The work in this thesis takes a step further from equilibrium states and studies the relationship of a minimised energy state with flux surface rotational transform in the simplest 2D system. In essence, instead of assigning a rotational transform to the flux surface of interest and calculating energy states, this work focuses on minimising energy and observe the behaviour of the flux surface rotational transform.

MRxMHD is used as it is the basis of SPEC, applicable for both 3D and 2D configurations and allows pressure jump conditions. The choice of using a periodic slab model is due to the axisymmetry of cylindrical and slab models; the Cartesian system of a slab is the most fundamental model which allows rigorous analytical study of the effects of rotational transforms within the plasma and at the interface of the plasma-vacuum boundary using the MRxMHD method. In Chapter 2, we introduce the two main methods used to analyse the stability of our chosen slab model. In Chapter 3, the results of both methods are presented together, showing the instabilities that appear in the variational method are confirmed by the tearing instability results. Section 3.5 details the slab model minimum energy dependency upon a range of variables such as helicity and wavenumbers.

Existing ideal MHD and resistive MHD theories are also shown to be unified under MRxMHD in Section 3.8, by comparing stability conditions and underlying theory principles. The MRxMHD plasma-vacuum slab is shown to only exhibit tearing instabilities with no ideal instabilities present. Lastly, we extend our work into the realm of non-zero pressure (Section 3.9); the discrepancy between the variational method and tearing instability calculations identified in Hole et al. [22] is confirmed, and may be resolved by a new MRxMHD method that allows for pressure perturbations within the plasma (Section 4.1).

In this work, we will answer in detail the following questions:

1. How is the minimised energy state of a plasma-vacuum slab system driven by flux surface rotational transforms?

2. Marginally stable solutions of $\lambda = 0$ at $\boldsymbol{k} \cdot \boldsymbol{B} = 0$, or $\boldsymbol{b} = 0$ have the smallest p and q integers, which are the lowest-order rationals and represent the interface rotational transform. In contrast, a 3D equilibria requires irrational interface rotational transforms (see Section 1.2).

3. How will the tearing instabilities in a plasma-vacuum slab be confirmed, and what effects will be seen in a zero and non-zero pressure system?

4. How will multiple resonances within the system affect stability calculations? What differences will be found between a plasma-only and plasma-vacuum slab in terms of system stability calculations, and the reason for discrepancies?

5. Does the inclusion of plasma pressure affect system stability for a slab model, and how does it compare to the results found for cylindrical models?

6. Does the discrepancy between MRxMHD and tearing instability theory previously found for a cylindrical model in Hole et al. [22] also exist in a plasma-vacuum slab model?

Chapter 2

Second Variation of Energy and Tearing Instability Models

The variational principle outlined in this Chapter originates from Taylor's relaxed plasma theory [38] and was built upon by Spies and Lortz [36], Kaiser and Uecker [25], and Hole et al. [21], among others to obtain a solution for the minimum energy of a plasma-vacuum system. The principle of minimised energy utilises the first and second variation of the total energy, and can be written as:

$\mathcal{W}$ = Thermal Energy + Magnetic Energy - Fixed Helicity - Total Mass,

$$\mathcal{W} = \sum_{i=1}^{N} \int \left(\frac{p}{\gamma - 1} + \frac{\boldsymbol{B} \cdot \boldsymbol{B}}{2\mu_o} - \frac{1}{2}\mu H - \nu p^{\frac{1}{\gamma}} \right) \, d^3\tau, \tag{2.1}$$

where $\mathcal{W}$ is the total potential energy of the system, p is pressure, $\boldsymbol{B}$ is the magnetic field, γ is the ratio of specific heats, and H is helicity. The variables μ and ν are Lagrangian multipliers, and μ_o is the vacuum permeability constant.

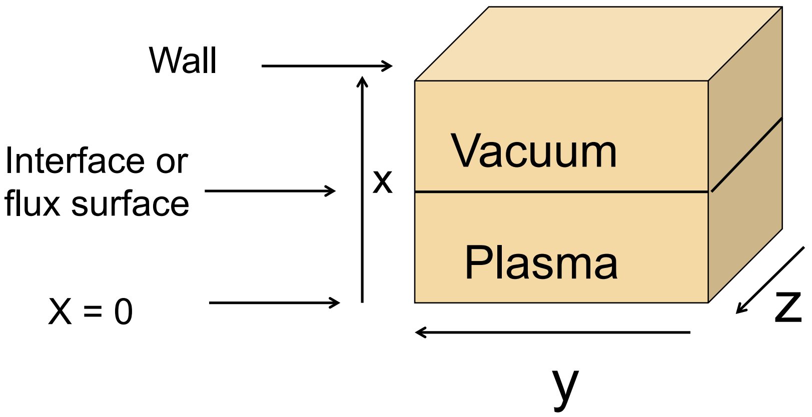

Figure 2.1: Slab model used for analysis.

The variational method used in the analysis of the plasma-vacuum system is applied to a 2-dimensional slab model with equilibrium quantities independent of its periodic y and z coordinates. Fig. 2.1 shows the slab model consisting of a plasma and vacuum region separated by an interface or flux surface. Both ends of the slab ($x = 0$ and $x = wall$) are perfectly conducting ideal MHD surfaces, such that $\boldsymbol{n} \cdot \boldsymbol{b} = 0$, where $\boldsymbol{n}$ is the outward-pointing unit normal vector and $\boldsymbol{b}$ is the perturbed magnetic field. This model allows the study of interface perturbations in this singular interface model. Linking the slab model to the cylindrical models utilised in aforementioned literature, the bottom of the slab and the interface are analogous to the inner tori, I_i of the 2-dimensional cylindrical model shown in Fig. 1.3. Due to the difference in co-ordinate systems, the magnetic field solutions are similar yet greatly simplified. Instead of working with Bessel solutions, the background magnetic fields and its perturbations become sinusoidal equations.

The variational method provides a set of equations from which an eigenvalue, λ is computed, and from this solution, a parametric scan is conducted to analyse the effects of the rotational transforms on the minimised energy of the system. To understand the stability results from the variational model, another treatment based upon tearing mode instability (Section 2.2) has been conducted. The main differences between the variational MRxMHD model and the tearing mode instability treatment are,

1. The tearing mode instability treatment uses a helical perturbation around a prescribed resonant surface.

2. The variational MRxMHD model treatment uses magnetic perturbations and does not require a resonant surface to be explicitly provided.

The variational model analyses the behaviour of the system energy under perturbation, but has implicit information regarding existing instabilities and resonant surfaces within the plasma-vacuum slab. It does not require or provide information as to the location of resonant surfaces, unlike the tearing instability calculations. As MRxMHD consists of relaxed resistive MHD in the regions between interfaces and ideal MHD at the interfaces, the tearing instability which is based upon resistive MHD theory contributes greatly to the discussion on the nature of the instabilities in the MRxMHD results.

Once both models are constructed, calculation of the rotational transform at the interface and the minimum value of λ for the variational model are available for analysis. Further analysis shows that high and low values of minimum energy are dependent on the rationality of the rotational transforms of their respective tearing instabilities, or tearing modes. The rotational transform at resonance surfaces and the plasma-vacuum interface can be identified as $\iota\!\!\!-$, and $\iota\!\!\!-$ of high-order and low-order rationals are linked to the behaviour of minimum λ in Chapter 3.

2.1 Variational Model

We introduce the variational model equations of MRxMHD, an eigenvalue problem of the second-order variation as discussed in Spies and Lortz [36] and Hole et al. [21] for a plasma-vacuum slab model.

Setting the first variation to zero, $\delta\mathcal{W} = 0$, produces the following equations:

$$Plasma : \nabla \times \boldsymbol{B} = \mu \boldsymbol{B}, \tag{2.2}$$

$$Interface : \left[\left[p + \frac{B^2}{2} \right]\right] = 0, \tag{2.3}$$

$$Vacuum : \nabla \times \boldsymbol{B} = 0. \tag{2.4}$$

The multiplier μ dimension is of inverse length. With constant p in plasma and $p = 0$ in vacuum, $\delta^2\mathcal{W}$ is minimised via the functional,

$$L = \delta^2 \mathcal{W} - \lambda N_A, \tag{2.5}$$

where λ is a Lagrange multiplier. The normalisation $N_A = \int d^2\sigma |\xi_i|^2$ [21], where $\xi_i = \boldsymbol{\xi_i} \cdot \boldsymbol{n}$ represents the normal interface displacement and $d^2\sigma$ is a surface element. With the constraint of $N_A = 1$, and setting $\delta L = 0$, the following equations are obtained:

$$
\begin{align}
&Plasma : \nabla \times \mathbf{b} = \mu \mathbf{b}, \tag{2.6a}\\
&Interface : \xi_i^* [[\boldsymbol{B} \cdot \boldsymbol{b}]] + \xi_i^* \xi_i [[B(\boldsymbol{n} \cdot \nabla)B)]] - \lambda \xi_i^* \xi_i = 0, \tag{2.6b}\\
&\boldsymbol{n} \cdot \boldsymbol{b}_{i,i+1} = \boldsymbol{B}_{i,i+1} \cdot \nabla \xi_i + \xi_i \boldsymbol{n} \cdot \nabla \times (\boldsymbol{n} \times \boldsymbol{B}_{i,i+1}), \tag{2.6c}\\
&Vacuum : \nabla \times \boldsymbol{b} = 0, \tag{2.6d}\\
&\nabla \cdot \boldsymbol{b} = 0, \tag{2.6e}\\
&Wall : \boldsymbol{n} \cdot \boldsymbol{b} = 0. \tag{2.6f}
\end{align}
$$

Eq. (2.6c) and (2.6f) are boundary conditions and do not originate from $\delta L = 0$. The subscripts $i, i+1$ denote different regions of plasma as shown in Fig. 1.3. The term ξ_i^* is the complex conjugate. In the slab model case, they refer to both sides of the interface. The energy term $\delta^2 \mathcal{W}$ is reformulated as λ; by setting $\delta L = 0$ one identifies λ as an eigenvalue which can be calculated from Eq. (2.6b).

Using a Cartesian system, $\xi_i \boldsymbol{n} \cdot \nabla \times (\boldsymbol{n} \times \boldsymbol{B}_{i,i+1})$ and $\xi_i^* \xi_i [[B(\boldsymbol{n} \cdot \nabla)B)]]$ reduce to zero. The Fourier decomposition of the perturbation of magnetic field, $\boldsymbol{b}$ and ξ_x, where m and κ represent the wavenumbers in the y and z direction respectively [21], gives,

$$\boldsymbol{b} = \hat{b} e^{i(my+\kappa z)}, \qquad \xi_i = A e^{i(my+\kappa z)}, \tag{2.7}$$

where $\hat{b}$ and A are complex Fourier amplitudes, related via:

$$\boldsymbol{b} = \nabla \times (\boldsymbol{\xi} \times \boldsymbol{B}). \tag{2.8}$$

As the slab model used in this work has only one interface, solving for λ becomes a single eigenvalue problem; multiple interfaces will result in a matrix eigenvalue problem. Using the variational model equations, a solution for the Beltrami equation is found for both the magnetic field, $\mathbf{B}$ and the perturbed magnetic field, $\mathbf{b}$. The variables that remain for parametric analysis are the constant pressure p, the wavenumbers m and κ, and the Lagrange multiplier μ that originates from the conservation of helicity in the MRxMHD model and also dictates the q-profile of the system.

Other than the boundary conditions described by Eq. (2.6c) and (2.6f), another criteria for the perturbation $\boldsymbol{b}$ is zero at the plasma edge, $x = 0$. Working in the Cartesian coordinate system, the equilibrium solutions of the Beltrami equation, $\nabla \times \boldsymbol{B} = \mu \boldsymbol{B}$ are found to be in the form of $\boldsymbol{B} = \{B_x, B_y, B_z\}$:

$$Plasma : \boldsymbol{B} = \{0, \alpha\cos(\theta+\mu x), -\alpha\sin(\theta+\mu x)\}\,, \tag{2.9}$$

$$Vacuum : \boldsymbol{B} = \left\{0, \sqrt{\left|\frac{\alpha^2}{1-\beta}\right|}\cos(\delta+\mu L+\theta), -\sqrt{\left|\frac{\alpha^2}{1-\beta}\right|}\sin(\delta+\mu L+\theta)\right\}, \tag{2.10}$$

where B_y and B_z of the vacuum region are constants, α is the magnetic field magnitude, and δ is the pitch angle by which the magnetic field in the vacuum can be offset from the magnetic field in the plasma, thereby creating a jump in the angle of magnetic field across the interface. Interface location for vacuum $\boldsymbol{B}$ is $L = 1$, β is related to the pressure term p via $\beta = \frac{2p}{B_V^2}$ and $B_V^2 - B_P^2 = 2p$ [25], where $B_P = \pm\alpha$ and $B_V = \pm\sqrt{\left|\frac{\alpha^2}{1-\beta}\right|}$.

The term θ represents the angle of $\boldsymbol{B}(x = 0)$ and is detailed in Sections 2.2.2 and 3.5.2. The variable μ is a Lagrangian multiplier, but also represents plasma helicity. In the vacuum region, Ampere's Law, $\nabla \times \boldsymbol{B} = \mu_o \boldsymbol{J}$ reduces to $\nabla \times \boldsymbol{B} = 0$ as there is no current, $\boldsymbol{J}$, and so $\mu = 0$ to represent this state.

Calculating the expression for $\boldsymbol{b}$ via the variational principle method also results in the term $\sqrt{-m^2-\kappa^2+\mu^2}$, and plays a role in stability conclusions for ideal MHD and resistive MHD work extensively studied by Goedbloed et al. [14]. This term will be revisited in Section 3.8. For some choices of m, κ, and μ, imaginary terms are introduced into λ and tearing instability parameter, Δ' (Section 2.2). This issue only exists in the plasma region as the vacuum region only has the term $\sqrt{m^2+\kappa^2}$. To circumvent this problem, the following equations were substituted in the course of deriving equations for perturbations in both λ and Δ':

$$F_p^2 = m^2 + \kappa^2 - \mu^2, \qquad\qquad F_n^2 = -m^2 - \kappa^2 + \mu^2, \tag{2.11}$$

where F_p represents the possible values of $\kappa^2 + m^2$ that are larger than μ^2, while F_n covers the the region of values where $\kappa^2 + m^2$ is less than μ^2. By using the above substitution, two solutions for λ, Δ', and its components are created; the parameter range is no longer constricted as $\sqrt{m^2+\kappa^2-\mu^2}$ is always in the real domain.

The resulting solution for $\boldsymbol{b}$ in the F_p domain calculated via the second variation Equations are as follows:

$$
\begin{aligned}
&b_x : i\alpha\operatorname{csch}\left(\frac{F_p x_{\text{int}}\sqrt{-F_p^2+m^2+\kappa^2}}{\mu}\right)\sinh\left(\frac{F_p x\sqrt{-F_p^2+m^2+\kappa^2}}{\mu}\right)\\
&(m\cos(\theta+\mu x_{\text{int}})-\kappa\sin(\theta+\mu x_{\text{int}})), \qquad (2.12)\\
&b_y : \frac{\alpha\mu}{(F_p^2-m^2-\kappa^2)(m^2+\kappa^2)}\operatorname{csch}\left(\frac{F_p x_{\text{int}}\sqrt{-F_p^2+m^2+\kappa^2}}{\mu}\right)(m\cos(\theta+\mu x_{\text{int}})\\
&-\kappa\sin(\theta+\mu x_{\text{int}}))F_p m\sqrt{-F_p^2+m^2+\kappa^2}\cosh\left(\frac{F_p x\sqrt{-F_p^2+m^2+\kappa^2}}{\mu}\right)\\
&+\kappa(-F_p^2+m^2+\kappa^2)\sinh\left(\frac{F_p x\sqrt{-F_p^2+m^2+\kappa^2}}{\mu}\right), \qquad (2.13)\\
&b_z : \frac{\alpha\mu}{(F_p^2-m^2-\kappa^2)(m^2+\kappa^2)}\operatorname{csch}\left(\frac{F_p x_{\text{int}}\sqrt{-F_p^2+m^2+\kappa^2}}{\mu}\right)(m\cos(\theta+\mu x_{\text{int}})\\
&-\kappa\sin(\theta+\mu x_{\text{int}}))F_p\kappa\sqrt{-F_p^2+m^2+\kappa^2}\cosh\left(\frac{F_p x\sqrt{-F_p^2+m^2+\kappa^2}}{\mu}\right)\\
&-m(-F_p^2+m^2+\kappa^2)\sinh\left(\frac{F_p x\sqrt{-F_p^2+m^2+\kappa^2}}{\mu}\right), \qquad (2.14)
\end{aligned}
$$

where x_{int} is the abbreviation for $x_{\text{interface}}$, representing the interface position at equilibrium. The solution of $\boldsymbol{b}$ in the F_n domain sees a difference in terms of non-hyperbolic functions.

With the expressions of $\boldsymbol{b}$ and various other variables stipulated above, an expression and numerical result for λ via Eq. (2.6b) can be obtained. The stability of the system can be found with a sign change, i.e. when λ is positive, the system is stable. Negative values indicate instability and $\lambda = 0$ is marginal stability.

2.2 Tearing Instability

> Magnetic Island, Queensland? Sounds like an unstable place.
>
> *Li Huey*

The tearing instability is best described as the breaking of magnetic field lines from their flux lines. In ideal MHD theory, the magnetic field lines are assumed to be frozen in place; reconnection and breaking of these trajectories are not allowed. An example of flux breakage can be seen in coronal ejections of the Sun and this class of instability was able to be modelled with the inclusion of resistivity into existing theory which allows an energy relaxation process. Tearing instabilities also allow the formation of magnetic islands, and can become 'chaotic' at large sizes [17], affecting the performance of a fusion device; in Nazikian et al. [34], tearing-like structures affect edge-localised modes (ELM), where the structures are formed by external magnetic coils in the effort to maintain the formation of pedestals in ELM suppression[1].

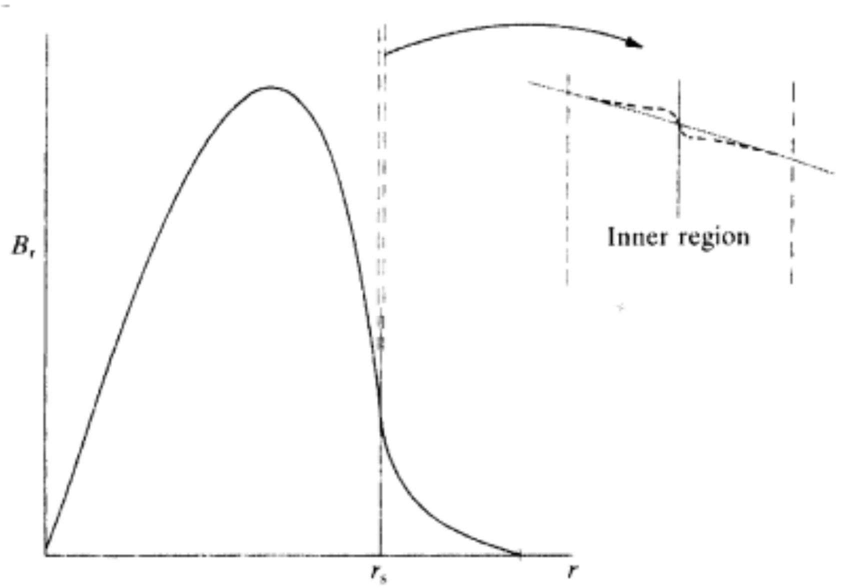

Figure 2.2: Depiction of the resistive layer around the resonant surface in the plasma. Unterberg, E. *Accesing High Normalized Current in an Ultra-low-aspect-ratio Torus.* ISBN 9780549385226.

Fig. 2.2 depicts the resistive layer in a plasma region, concentrated around a resonant surface. This inclusion of resistivity is the basis of tearing instability theory. Away from the resistive layer, ideal MHD approximations still hold, but at the resistive layer, tearing instabilities can occur. The resonant surface is due to the magnetic field line topology resonating with wave perturbations in the model. Resonant surfaces are flux surfaces that are of modes decided by the q-profile (or safety factor) (further discussed in Section

---

[1] Although the method of creation and application of the tearing structures are not related to the work in this thesis, the effects of tearing modes and magnetic islands can be found in many research areas of fusion.

2.2.2) which can be anywhere within the system and can be a location of destabilisation or formation of instabilities.

The tearing instability parameter, Δ' is the logarithmic derivative of the helical perturbation around a given resonant surface (Eq. (2.15a)). The solution for Δ' is computed using Eqs. (2.15a) - (2.15g) [37], this gives marginal stability ($\Delta' = 0$) and the sign of Δ'. To compute an Ohm's Law growth rate for tearing modes, it must be solved in a resistive layer around the resonant surface (as depicted in Fig. 2.2) and related to the outer region solutions.

The solution for Δ' is determined by the equations relevant to the outer region:

$$\text{Tearing instability parameter, } \Delta' = \left(\frac{\partial \tilde{\chi}}{\partial x_s^+} - \frac{\partial \tilde{\chi}}{\partial x_s^-}\right), \tag{2.15a}$$

$$\text{Equation of Motion : } \rho\left(\frac{\partial \boldsymbol{v}}{\partial t} + \boldsymbol{v}\cdot\nabla\boldsymbol{v}\right) = \boldsymbol{j}\times\boldsymbol{B} - \nabla p, \tag{2.15b}$$

$$\text{Velocity field : } \boldsymbol{v}(x,u) = \nabla\varphi(x,u)\times\boldsymbol{h} + v_h(x,u)\,\boldsymbol{h}, \tag{2.15c}$$

$$\text{Magnetic field : } \boldsymbol{B}(x,u) = \nabla\chi(x,u)\times\boldsymbol{h} + g(x,u)\,\boldsymbol{h}, \tag{2.15d}$$

$$\text{Helical perturbations : } \tag{2.15e}$$

$$\chi(x,u,t) = \chi_{\text{eq}}(x) + \tilde{\chi}(x)\,e^{\Gamma t + iu}, \tag{2.15f}$$

$$g(x,u,t) = g_{\text{eq}}(x) + \tilde{g}(x)\,e^{\Gamma t + iu}, \tag{2.15g}$$

where $u = m\theta + \kappa z$ and $\boldsymbol{j} = \frac{\nabla\times\boldsymbol{B}}{\mu_o}$. In the magnetic field equation, χ is the helical flux, and g is the helical field [12]. The incompressible velocity field is similarly written as the magnetic field equation, and thus φ and v_h represent the perpendicular and parallel components respectively. For a cylindrical model, $\boldsymbol{h}$ of Eq. (2.15c) and (2.15d) is defined as $f(r)\nabla r\times\nabla u$ and is a cylindrical vector orthogonal to ∇u. The metric term $f(r)$ is represented as $\frac{1}{r(\nabla u)^2} = \frac{r}{m^2+k^2r^2}$ [12]. The subscript eq refers to equlibrium quantities, while Γ represents the growth rate of the helical perturbations.

The helical perturbation terms are of interest, and following the methodology of Tassi et al. [37], the projections of the linearised equation of motion provides an equation representing $\tilde{\chi}$ (Section 2.2.1). Thus, the tearing instability parameter Δ' can be calculated and compared with the variational principle eigenvalue parameter; $\Delta' < 0$ indicates stability, and $\Delta' > 0$ indicates instability of the resistive tearing mode.

2.2.1 Solving for $\tilde{\chi}$, the perturbation of the helical flux

In a Cartesian system, $u = my + \kappa z$ and $f = \frac{1}{(\nabla u)^2} = \frac{1}{m^2+k^2}$. With the equations,

$$\nabla\times\boldsymbol{B} = \mu\boldsymbol{B}, \tag{2.16}$$

$$\nabla\cdot\boldsymbol{B} = 0, \tag{2.17}$$

and projecting the linearised equation of motion (Eq. (2.15b)) along $\boldsymbol{h}$ and ∇r, the resulting equations are:

$$g_{\text{eq}}(x) = \frac{\tilde{\chi}(x)}{\chi'_{\text{eq}}(x)}g'_{\text{eq}}(x), \tag{2.18}$$

and

$$\frac{\partial\tilde{\chi}(x)^2}{\partial x^2}+\left[\frac{g_{\text{eq}}(x)}{\chi_{\text{eq}}'(x)}\left(\frac{g_{\text{eq}}'(x)}{\chi_{\text{eq}}'(x)}\right)'+\left(\frac{g_{\text{eq}}'(x)}{\chi_{\text{eq}}'(x)}\right)^2-\frac{1}{f}\right]\tilde{\chi}(x)=0. \tag{2.19}$$

This differential equation has its counterpart in Eq. (28) of Tassi et al. [37]. The term μ is constant in the plasma and a step function across the plasma-vacuum interface; with the relationship $\mu=\frac{g_{\text{eq}}'}{\chi_{\text{eq}}'}$ from the linearising process, $\left(\frac{g_{\text{eq}}'(x)}{\chi_{\text{eq}}'(x)}\right)'$ is zero everywhere except at the interface.

The final differential equation is then of the form:

$$(-m^2-\kappa^2+\mu^2)\tilde{\chi}(x)+\tilde{\chi}''(x)=0. \tag{2.20}$$

With F_p and F_n substitutions, $\tilde{\chi}$ exhibits hyperbolic terms *sinh* and *cosh* for the F_p terms, and *sin* and *cos* using F_n. The new expressions for $\tilde{\chi}$ are:

$$\tilde{\chi}(x)=e^{F_p x}C_1+e^{-F_p x}C_2, \tag{2.21}$$

$$\tilde{\chi}(x)=\cos(F_n x)C_1+\sin(F_n x)C_2, \tag{2.22}$$

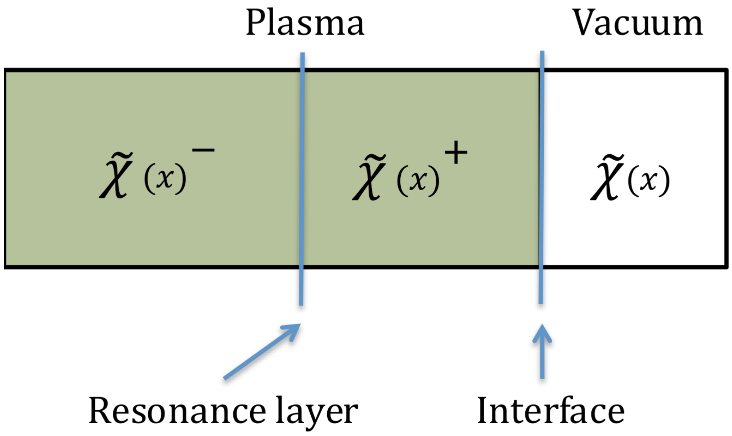

Figure 2.3: Diagram depicts the location of $\tilde{\chi}$ with respect to the resonance layer and plasma-vacuum interface. Each region has a different solution for $\tilde{\chi}$ due to different coefficient values.

as shown in Fig. 2.3 where $\tilde{\chi}(x)^-$ represents the helical perturbation before a resonant surface, $\tilde{\chi}(x)^+$ is after the resonant surface, and $\tilde{\chi}(x)$ in the vacuum region. The constants C_1 and C_2 are determined by setting continuity of $\tilde{\chi}$ at the resonant surface and interface, the jump condition between plasma and vacuum, as well as the boundary conditions $\tilde{\chi}(x=0)=0$ and $\tilde{\chi}(x=x_{wall})=0$. One coefficient will be undefined due to the existence of 6 coefficients with 5 boundary equations, and this should be a coefficient of the vacuum perturbation to allow the perturbations in the plasma to be pressure dependent (Section 3.9). From Eq. (2.15a), the undefined coefficient is carried into the expressions for $\tilde{\chi}$ and will cancel out, providing a numerical solution for a given set of variables.

2.2.2 Rotational transform, q-profiles and resonant surfaces

The rotational transform is defined as the number of rotations of the poloidal magnetic field per toroidal magnetic field rotation in a cylindrical coordinate system. As the current model used in this work is a Cartesian system, the rotational transform becomes:

$$\iota\!\!-= \frac{L_z}{L_y}\frac{B_y}{B_z}, \tag{2.23}$$

where L_y and L_z are periodic lengths in the y and z directions. The q-profile of the system, also known as the safety factor, is :

$$q = \frac{1}{\iota\!\!-} = \frac{L_y}{L_z}\frac{B_z}{B_y}. \tag{2.24}$$

From the Beltrami solution Eq. (2.9) and (2.10) for plasma and vacuum, the rotational transform and q-profile of both regions in the slab model are obtained. The q-profile utility is illustrated in the calculation for tearing instabilities, as a resonant surface is required to obtain a Δ' value. Fig. 2.4 shows a plotted q-profile across the plasma-vacuum region for a choice of μ. The q-profile equation can also written as:

$$q = -\tan(x\mu + \theta). \tag{2.25}$$

For any location in the plasma volume, x of Eq. (2.25) may be replaced by the resonant surface x_{rs} to find a corresponding q value.

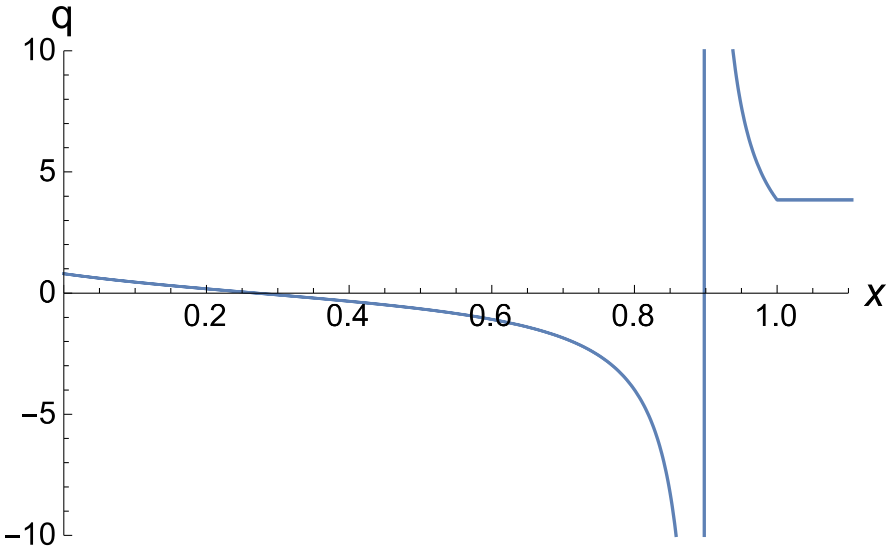

Figure 2.4: A q-profile selection plotted across the plasma-vacuum region with $\mu = 2.5, \theta = -\cot^{-1}\frac{\mu}{2}$ and $\delta = 0$. Plasma-vacuum interface is at $x = 1$.

The rotational transform value at the core of a cylindrical co-ordinate system, θ can be selected as $\iota\!\!-_o = \frac{L_z\mu}{4\pi}$, where L_z is periodic in the z direction [21]. Equating this value to the slab model Eq. (2.24), $\theta = -\cot^{-1}\frac{\mu}{2}$ by allowing $L_y = 2\pi a$, where $a = 1$, the minor radius of the plasma region. Another option is $\theta = -\cot^{-1}\frac{\mu}{4\pi}$ if the slab is assumed to have equal dimensions in the y and z direction, but with an arbitrarily chosen initial rotational transform, which is set to the $\iota\!\!-$ of a cylinder. It is shown in Sections 3.5.2 and 3.5.4 that the choice of θ does not affect stability conclusions. From the expressions above, it is shown that the q-profile and rotational transform of the interface itself can be obtained by setting the appropriate value of x for the interface location. The relation between the q-profile and wavenumbers can be seen in the equation $\boldsymbol{k} \cdot \boldsymbol{B} = 0$, where,

$$k = m\hat{y} + \kappa\hat{z}, \tag{2.26}$$

$$\boldsymbol{B} = B_y\hat{y} + B_z\hat{z}, \tag{2.27}$$

along with Eq. (2.24) and $L_y = L_z$ provides

$$q = -\frac{m}{\kappa}. \tag{2.28}$$

Thus by plotting a q-profile across the plasma-vacuum region, $\iota\!\!\!-$, m and κ values can be obtained for any choice of x_{rs}, or resonant surface.

2.3 $k \cdot B$ Resonant Line

The function $\boldsymbol{k} \cdot \boldsymbol{B}$ presents frequently in subsequent analysis, and its function for stability analysis is described in this Section. The equation describing the relationship between $\boldsymbol{k} \cdot \boldsymbol{B}$ and λ stems from the ideal MHD shear Alfvén wave dispersion relation [2, 4, 15],

$$\omega^2 = k_{\|}^2 \upsilon_A^2 = \frac{\boldsymbol{k} \cdot \boldsymbol{B}}{\sqrt{\mu_o \rho_o}}. \tag{2.29}$$

The term $k_{\|}$ is k along $\boldsymbol{B}$, υ_A is the shear Alfvén speed which propagates along $\boldsymbol{B}$, and $\omega^2 = \lambda$ for the case of a constant density ρ_o plasma. It is then easily seen that $k_{\|} = 0$ causes $\omega^2 = 0$.

To obtain the wavenumbers required for $\lambda(x_{\text{interface}}) = 0$, calculating $\boldsymbol{k} \cdot \boldsymbol{B} = 0$ in lieu of $\lambda(x_{\text{interface}}) = 0$ drastically reduces computational time due to the complexity of the λ solution. As λ is parabolic in the region of interest, i.e. marginal stability, there are two solutions for $\lambda = 0$, and thus $\boldsymbol{k} \cdot \boldsymbol{B} = 0$ is ideal to obtain $\lambda(x_{\text{interface}})$ wavenumber information.

Finally, in Section 3.8, it is shown that $\boldsymbol{k} \cdot \boldsymbol{B}$ plays a major role in unifying ideal MHD, resistive MHD and MRxMHD theories cohesively in terms of Newcomb's stability analysis [35].

Results

> You don't look very relaxed.
>
> *Brett*

In this Chapter, the variational and tearing instability results will be discussed in tandem, as the variational method results require the tearing instability theory to shed light on the instabilities found, and why they exist.

3.1 Variational Method Results

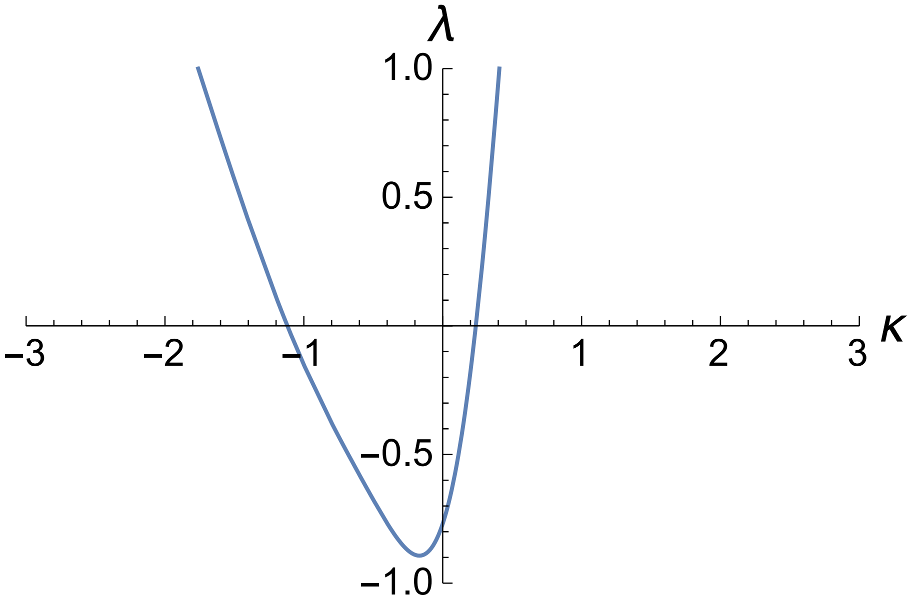

Figure 3.1: Dependence of λ on κ showing values of stability and instability, with normalisation $N_A = \int |\xi|^2 d^2\sigma = 1$, $\theta = -\cot^{-1}(\frac{\mu}{2})$ and $m = 1$, $\mu = 3$.

Fig. 3.1 shows the stability plot for a fixed value of μ and m over a range of κ. As seen in the plot, there is a narrow region of κ for which λ is negative (system unstable). The marginal stability points are when $\lambda = 0$ along the κ-axis.

Fig. 3.2 depicts how magnetic perturbations shape λ. The perturbation b_x is in the imaginary domain and is solved by considering the boundary conditions, $b_{x=0} = 0$ and $b_{x_{\text{wall}}} = 0$ where its coefficients apply to b_y and b_z, both of which are in the real domain. The term $\boldsymbol{k} \cdot \boldsymbol{B} = 0$ occurs at the plasma-vacuum interface ($x = 1$), and when $\lambda = 0$ with $\boldsymbol{b} = 0$ as introduced in Section 2.3.

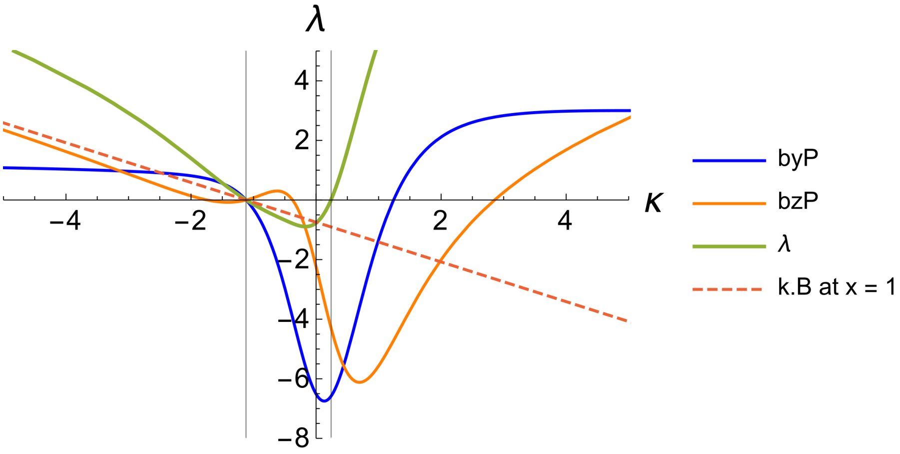

Figure 3.2: Plot of $\lambda(N_A = 1)$ and plasma region magnetic perturbations $\boldsymbol{b}$ (byP and bzP), and $\boldsymbol{k} \cdot \boldsymbol{B}$ at $x = 1$. Variables used are $\theta = -\cot^{-1}(\frac{\mu}{2})$, $m = 1$, $\mu = 3$, and $x_{\text{interface}} = 1$.

By calculating for $\boldsymbol{k} \cdot \boldsymbol{B} = 0$ with the variable values provided, the κ value is found to be -1.11833 for this particular choice of variables shown in Fig. 3.2. Using the Mathematica function *FindRoot*, $\lambda = 0$ results in an identical κ value where $\boldsymbol{k} \cdot \boldsymbol{B} = 0$. The same Mathematica function with a starting search value closer to the other zeroth point of λ provides the κ value of 0.238404. These two values are indicated by the grey vertical lines in Fig. 3.2.

It is shown in Fig. 3.2 that when the magnetic perturbations are both zero, λ is zero, but the converse is not always true. The second zeroth point does not correspond to a vanishing perturbation and the unstable region is theorised at this point to be a tearing instability, which is subsequently proven by incorporating the tearing instability model to test for result correlation (Section 3.2). Fig. 3.3 shows the behaviour of the magnetic perturbations on the vacuum side of the interface also intersecting at the $\lambda = 0$ line, thereby confirming when all perturbations in the model are zero, the system is marginally stable.

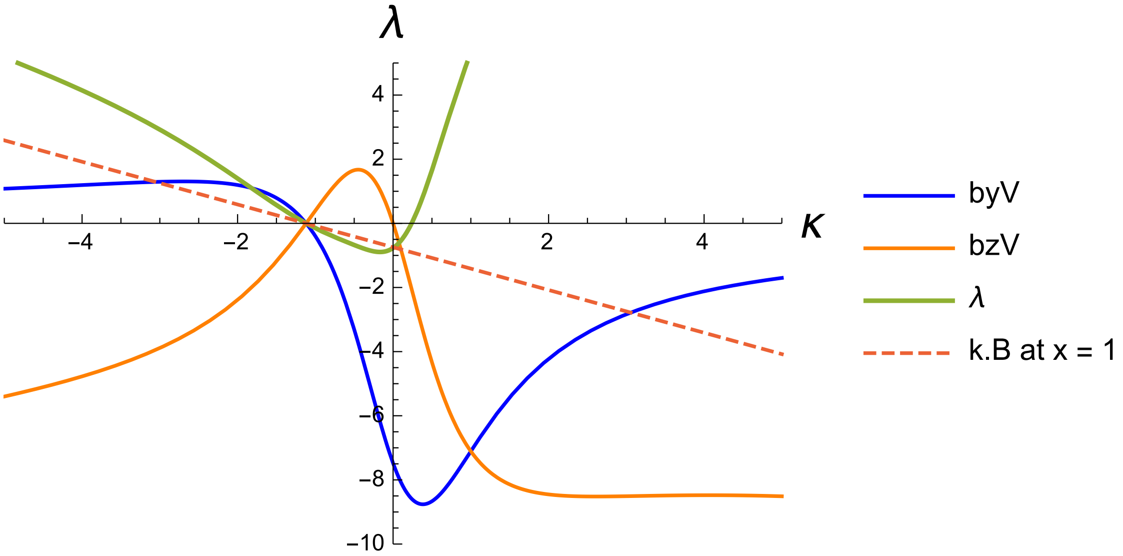

Figure 3.3: Plot of $\lambda(N_A = 1)$ and vacuum region magnetic perturbations $\boldsymbol{b}$ (byV and bzV), and $\boldsymbol{k} \cdot \boldsymbol{B}$ at $x = 1$. Variables used are $\theta = -\cot^{-1}(\frac{\mu}{2})$, $m = 1$, $\mu = 3$, and $x_{\text{interface}} = 1$.

3.2 Tearing Instability Results

As described in Section 2.2.1, the solution of Eq. (3.1a) - (3.1e) is dependent upon its boundary conditions. These equations describe the perturbation in each region of the plasma-vacuum model for F_p and F_n, where x_{rs} denotes the resonant surface:

$$\tilde{\chi}(x) = e^{-F_p x}C_{1P} + e^{F_p x}C_{2P} \qquad 0 < x < x_{\text{rs}}, \tag{3.1a}$$

$$\tilde{\chi}(x) = \cos(F_n x)C_{1N} + \sin(F_n x)C_{2N} \qquad 0 < x < x_{\text{rs}}, \tag{3.1b}$$

$$\tilde{\chi}(x) = e^{-F_p x}C_{3P} + e^{F_p x}C_{4P} \qquad x_{\text{rs}} < x < 1, \tag{3.1c}$$

$$\tilde{\chi}(x) = \cos(F_n x)C_{3N} + \sin(F_n x)C_{4N} \qquad x_{\text{rs}} < x < 1, \tag{3.1d}$$

$$\tilde{\chi}(x) = e^{x\sqrt{m^2+\kappa^2}}C_{1V} + e^{x\sqrt{m^2+\kappa^2}}C_{2V} \qquad 1 < x < x_{\text{wall}}. \tag{3.1e}$$

Fig. 3.4 verifies the continuity calculations for $\tilde{\chi}$ at the resonant surface and plasma-vacuum interface, and the perturbation is zero at the vacuum wall and the plasma edge. The plasma-vacuum interface equation required to obtain a coefficient is found in Hole et al. [22]:

$$\left[\left[\chi_0' \frac{\tilde{\chi}'}{\tilde{\chi}}\right]\right] = \left[\left[\chi_0' \frac{g_0}{\chi_0}\mu\right]\right]. \tag{3.2}$$

Thus, all the coefficients denoted with C in Eq. (3.1a) - (3.1e) are solved and the tearing instability can be calculated. To ensure the perturbation of the helical flux, $\tilde{\chi}$ of Eq. (2.21) and Eq. (2.22), are continuous across the plasma-vacuum region, Fig. 3.4 displays $\tilde{\chi}$ plotted with respect to the plasma length.

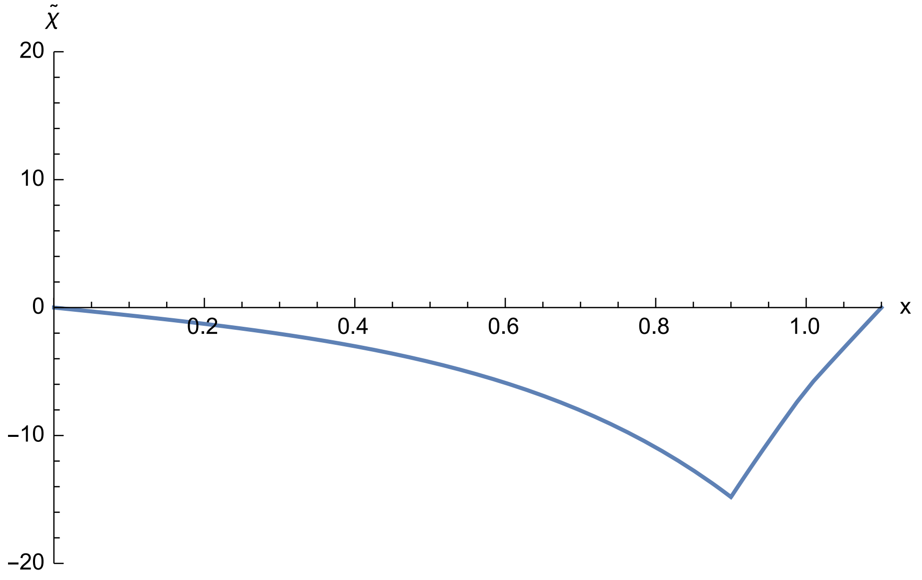

Figure 3.4: Plot of $\tilde{\chi}$ demonstrating continuity across the plasma-vacuum region, with a resonant surface located at $x_{\text{rs}} = 0.9$, with $x_{\text{wall}} = 1.1$.

The tearing instability calculation requires a resonant location within the chosen model, as described in Section 2.2. This is achieved by choosing a q-profile for the plasma-vacuum region, and obtaining m and κ values from the q-profile.

Fig 3.5 illustrates the method of finding κ; if the resonant surface is chosen to be at

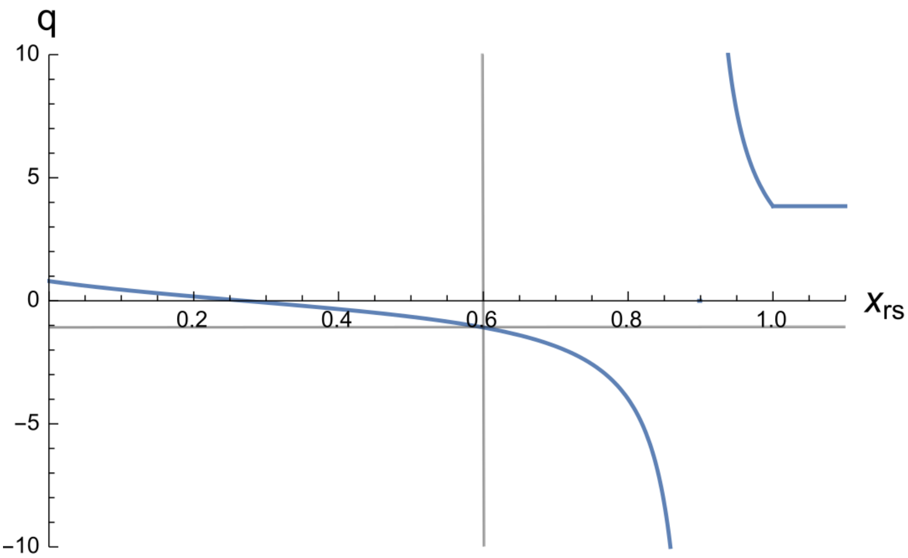

Figure 3.5: Q-profile plot for $\theta = -\cot^{-1}(\frac{\mu}{2})$ and $\mu = 2.5$ across the plasma-vacuum region illustrates the method for finding κ.

$x_{\mathrm{rs}} = 0.6$, the value on the q-profile axis is -1.08308. With Eq. (2.28), and a chosen value for m, i.e. $m = 1$, $\kappa = 0.923295$ is calculated. This method can be used to calculate m for a given κ as well. The chosen wavenumber for benchmarking purposes is $m = 1$. Calculating the components of logarithmic differentiation of the tearing mode equation, Eq. (2.15a), we compute $-\Delta'$ across the plasma region for any value of resonant location, where the positive region signifies stability and the negative region is unstable.

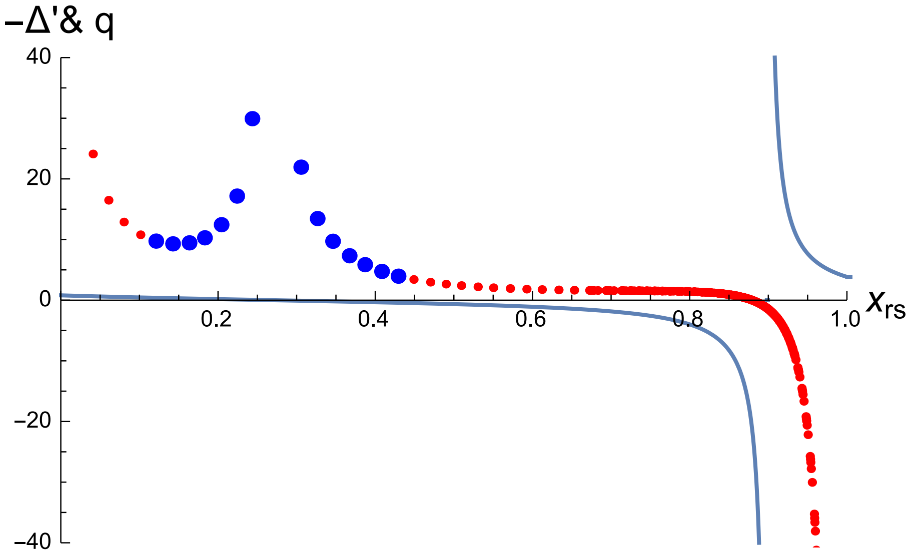

Figure 3.6: Plot of Δ' across the plasma region. Note a singularity at the equilibrium field reversal point around the blue datapoints, and another singularity as x_{rs} approaches the step in μ at the plasma-interface of $x = 1$.

In Fig. 3.6, the red data points denote the F_n region (where $\kappa^2 + m^2 < \mu^2$), and the blue data points denote the F_p region. The first singularity of $-\Delta'$ is when the q-profile is zero at the magnetic field line reversal radius, $x_{\mathrm{rs}} = 0.269896$, where $B_z = 0$. The q-profile goes to infinity when $B_y = 0$. The second singularity of $-\Delta'$ is when the resonant surface approaches the interface from the left where the μ value changes as a step function; this tearing instability behaviour is documented in Fig. 6. of Tassi et al. [37]. We then compare the variational model to the tearing instability model. Fig. 3.7 compares $-x_{\rm rs}\Delta'$ and λ as a function of κ; stability regions are indicated by a positive magnitude and vice versa. The instability seen in the variational or minimum energy plot is a tearing instability with the resonant surface located within the plasma region, and $-x_{\rm rs}\Delta'$ approaches negative infinity as the resonant surface approaches the plasma-vacuum interface, marked by the vertical line.

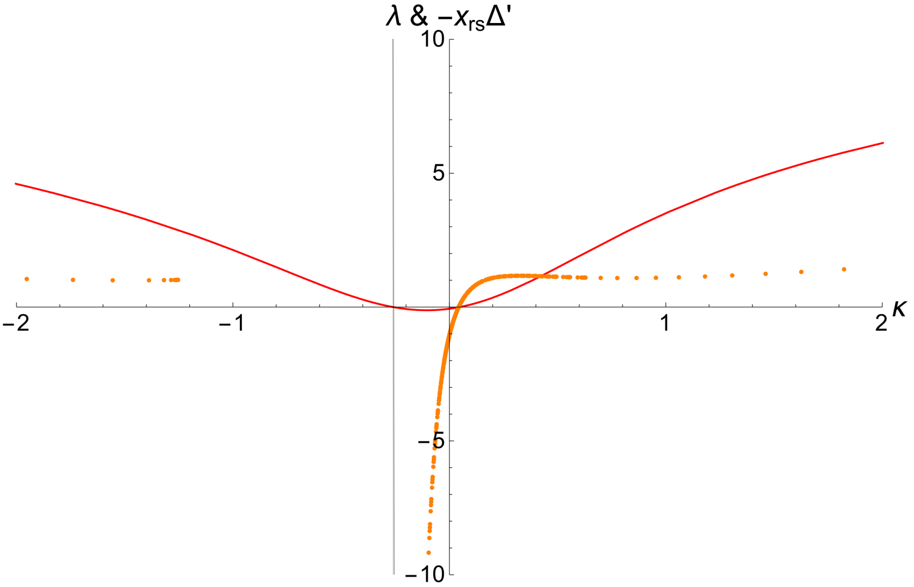

Figure 3.7: Tearing mode parameter, $-x_{\rm rs}\Delta'$ (orange dots) and variational parameter λ (solid red line) as a function of κ, $m = 1$, and $\mu = 2.5$.

Note that the $-\Delta'$ data points do not cover a region of the κ axis to the left of the vertical gridline in Fig. 3.7 which we will call *Region A*; this is due to the lack of resonant surfaces in the plasma-vacuum slab for *Region A*. To illustrate this point, we select two κ values; $\kappa = -0.260101$ at $\lambda = 0$ (marked by the vertical gridline in Fig. 3.7), and $\kappa = -1$ which is in *Region A*.

Fig. 3.8 shows the $\mu = 2.5$ q-profile with marked q-profile values for $\kappa = -0.260101$ and $\kappa = -1.0$ found by Eq. (2.28). As expected, $q_{\kappa=-0.260101}$ corresponds to a resonant surface at the plasma-vacuum interface, while $q_{\kappa=-1.0}$ does not correspond to any resonant surface along the plasma-vacuum slab.

When there are no resonant surfaces observed in the plasma-vacuum slab for a given choice of m and κ, tearing instabilities cannot develop, and so λ can only be stable which is shown in *Region A*. The existence of other instability types such as external kink instabilities does not exist in the slab configuration and is elaborated in Goedbloed and Dagazian [16] and the work in Section 3.8.

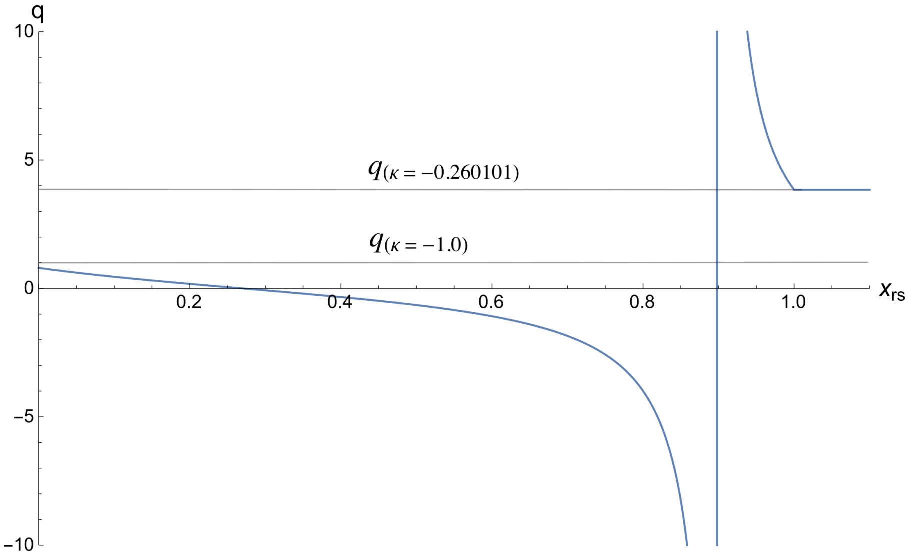

Figure 3.8: Eq. (2.25) with respect to x_{rs}. $q_{\kappa=-0.260101}$ corresponds to a resonant surface, while $q_{\kappa=-1.0}$ does not correspond to any resonant surface.

3.3 Normalisation

In Section 2.1, the normalisation is based upon interface displacement, $N_A = \int |\xi_i|^2 d^2\sigma$ where $d^2\sigma$ is a surface element, and we set this to a constant 1 for our initial calculations for λ. $N_A = 1$ enables evaluation of minimum system stability from the sign of $\lambda > 0$ being stable and $\lambda < 0$ representing the unstable regions. This choice of normalisation is independent of volume and plasma helicity, as the interface displacement is only dependent upon displacement magnitude and wavenumbers, m and κ [21].

After λ is obtained from second variation equation Eq. (2.6b), a different normalisation [39] may be multiplied to the eigenvalue to provide a physical definition to the eigenvalue in terms of plasma volume and helicity which are dependent upon the dimensions of the slab and μ. The following work explains the approach and the results of different normalisation choices.

In Spies and Lortz [36], the functional,

$$L = \delta^2 \mathcal{W} - \lambda N_B, \tag{3.3}$$

is used to evaluate the eigenvalue λ with $N_B = \int \boldsymbol{b}^2 \; d^3\tau = 1$ and $\boldsymbol{b} = \nabla \times \boldsymbol{a}$. For comparison in the region of instability across a range of μ, the constant volume integral of N_B is instead retained as a function of μ. Replacing $N_A = 1$ with μ-dependent N_B normalisation requires the following equations:

$$L = \delta^2 \mathcal{W} - \lambda_1 N_A = 0, \tag{3.4}$$

$$L = \delta^2 \mathcal{W} - \lambda_2 N_B = 0, \tag{3.5}$$

$$\lambda_2 = \lambda_1 \frac{N_A}{N_B}. \tag{3.6}$$

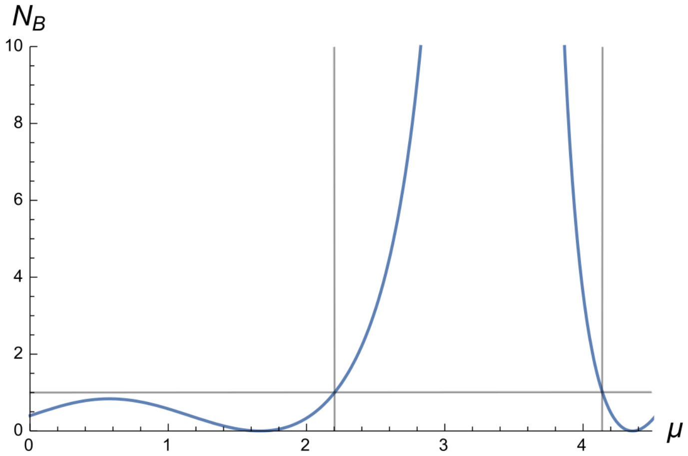

Figure 3.9: Plot of N_B showing the behaviour of this normalisation choice over the μ-range.

Fig. 3.9 shows N_B over a μ range, and Fig. 3.10 shows the effect of N_B upon the magnitude of λ; magnitude of λ is dependent upon a chosen normalisation. Using the volume integral normalisation provides an identical λ result with a scaling factor difference. By inspection of Fig. 3.10, the zero crossing points are more distinct with $N_A = 1$, hence further discussion will feature stability results based upon $N_A = 1$, unless stated otherwise, namely in Section 3.5 and Section 3.6. The κ values at minimum and marginal stability also have not been modified by the change in normalisation. This is a key piece of information as the minimum stability of the slab system will ultimately depend on the m and κ values at resonant surfaces (Section 3.6).

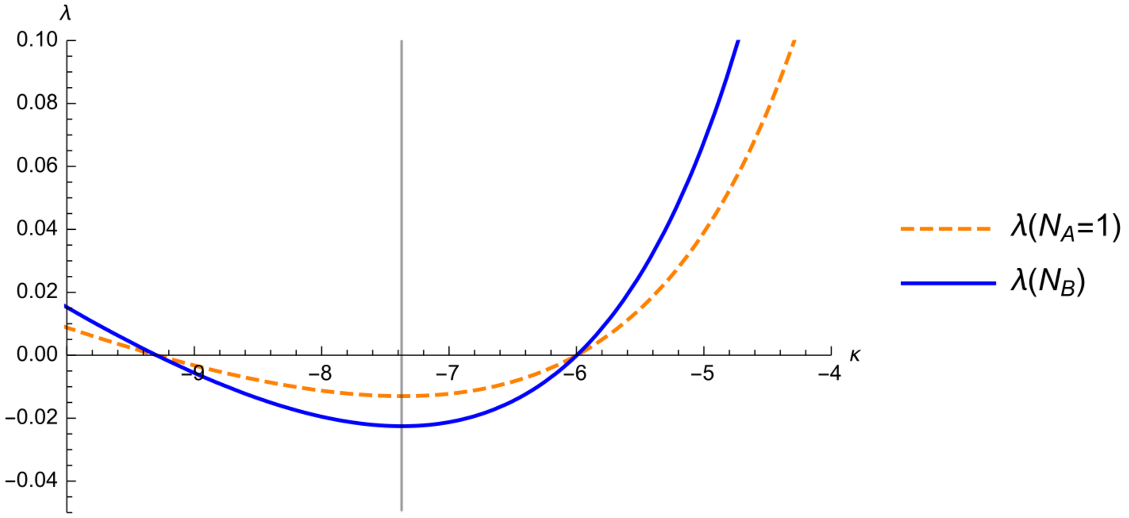

(a) $\mu = 1$

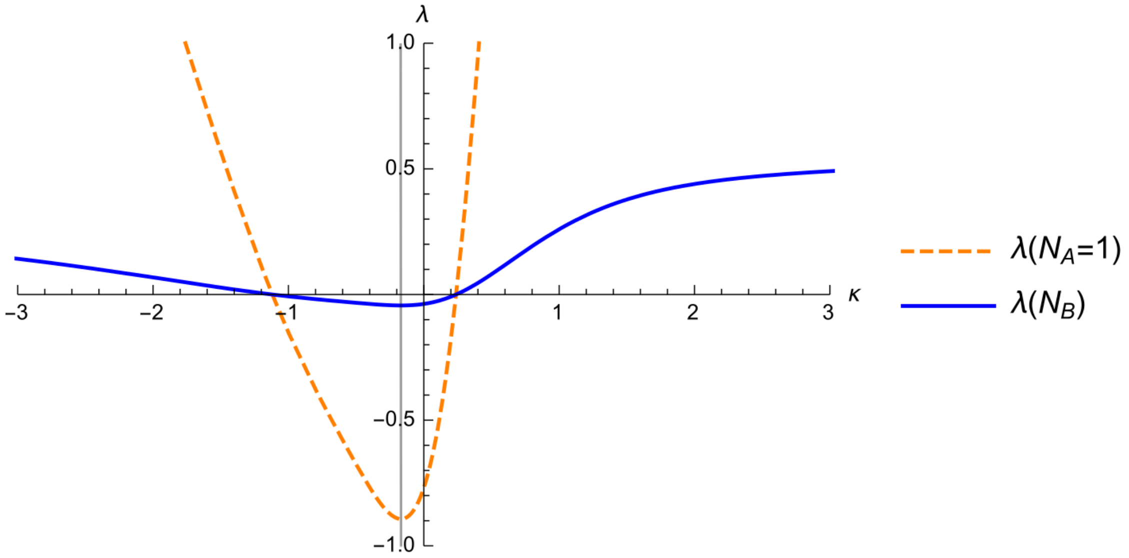

(b) $\mu = 3$

Figure 3.10: Overlaid λ plots with a grey vertical line denoting the κ value for minimum stability on both plots.

Fig. 3.11 displays λ of different normalisations across a range of μ. The zeroth points of λ in Fig. 3.11a are now singularities and vice versa in Fig. 3.11b; in Section 3.8, the importance of the singularities are shown to be related to the μ limit value of resistive MHD instability as described in Gibson and Whiteman [13].

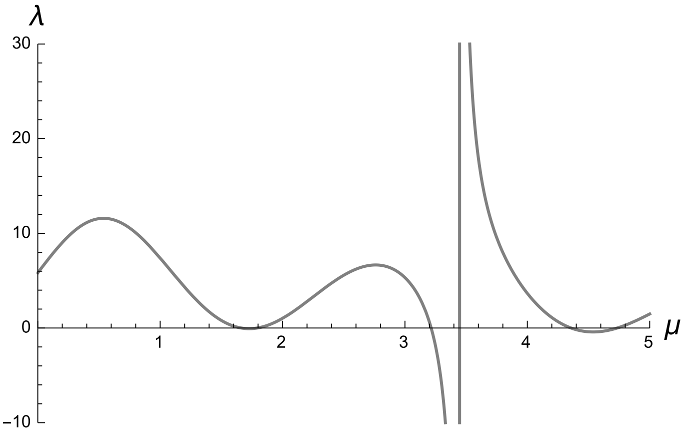

(a) λ with $N_A = 1$.

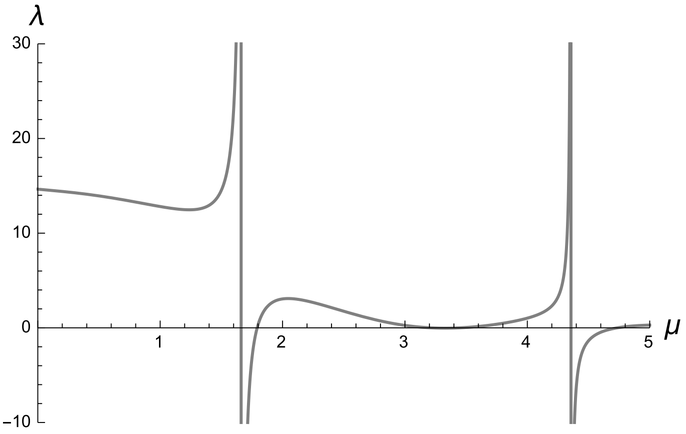

(b) λ with N_B.

Figure 3.11: The effect of different normalisation choices on λ over a μ range, with $\kappa = 1$, $m = 1$, $\theta = -\cot^{-1}(\frac{\mu}{2})$.

3.4 Multiple Resonances

It is remarked that the tearing instability, $-\Delta'$ calculation only assumes one resonant surface exists within the plasma. Fig. 3.12 shows that the choice of μ for the q-profile dictates the presence of single or multiple resonant surfaces within the plasma. The tearing model can be extended to account for multiple resonant surfaces with identical wavenumbers, but requires additional terms to reflect the additional resonances, while the variational model requires no change. Therefore, as shown in Fig. 3.13, $-\Delta'$ calculations would no longer completely agree with the variational model for multiple resonant surfaces.

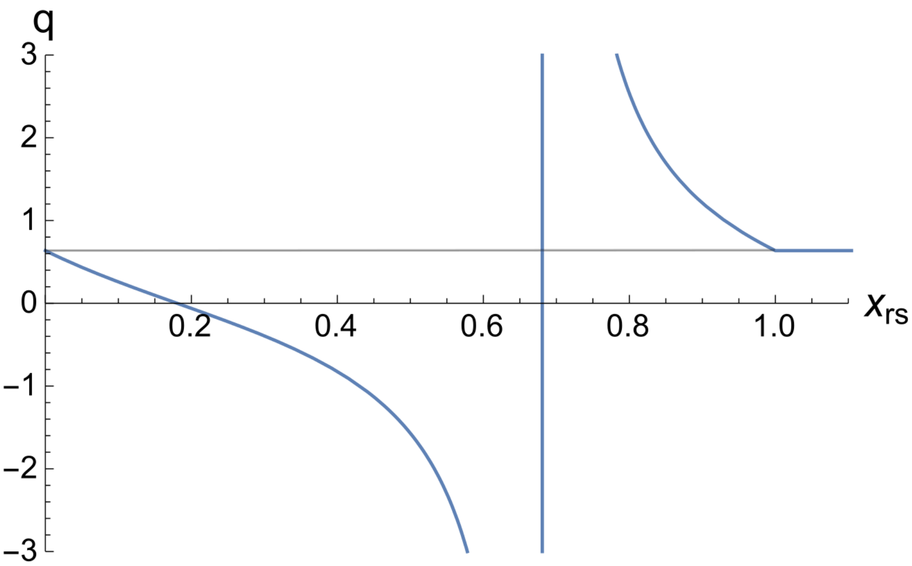

(a) $\mu = \pi$ is maximum μ before multiple resonances occur in the q-profile.

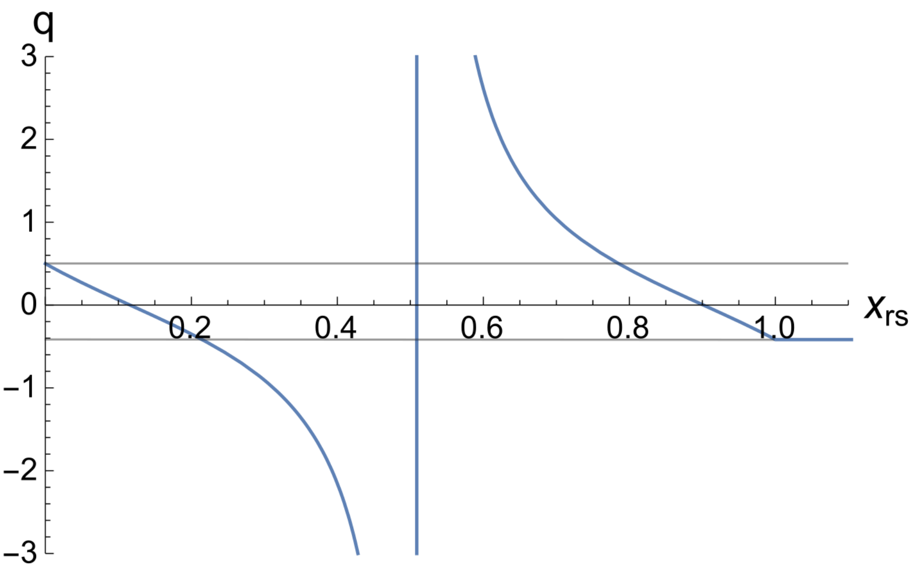

(b) At $\mu = 4$, multiple resonances form as there are two identical values of q but at different resonant locations.

Figure 3.12: The existence of multiple resonant surfaces at higher μ values.

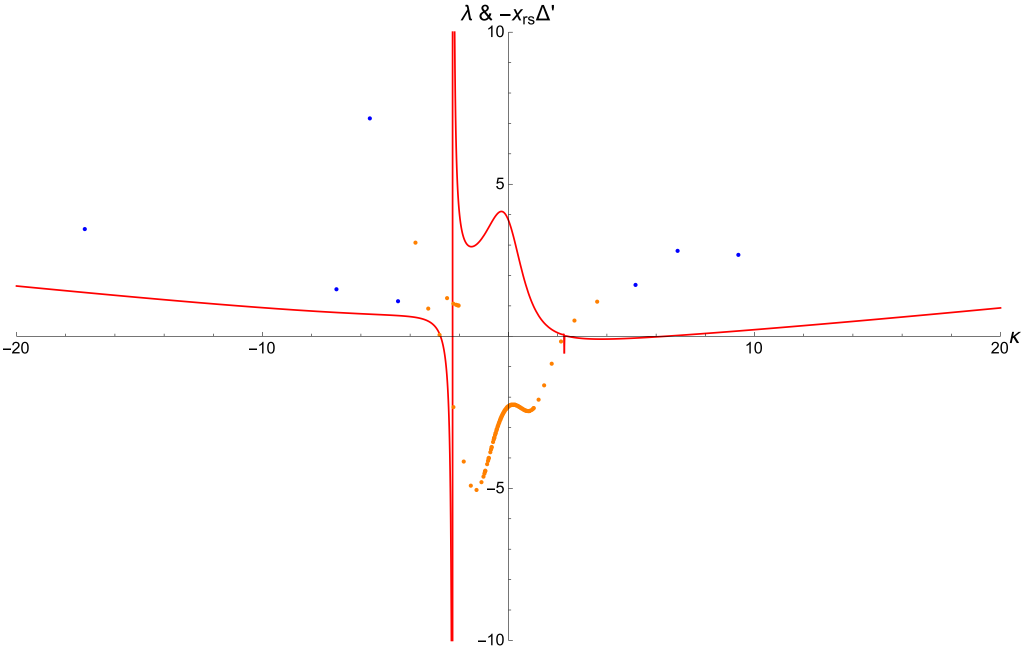

Figure 3.13: λ (solid red line) and $-\Delta'$ (dots) plot comparison at $\mu = 4$.

3.5 Minimum Stability

> Perhaps you will find relaxation from an activity that resonates with you.
>
> *Li Huey*

This Section explains how the minimised energy state of a plasma-vacuum slab system is driven by flux surface rotational transforms, as mentioned before in Section 1.2. To understand the relationship between slab model minimum stability and interface rationality, the minimum stability of a variable set is sought, instead of the marginal stability point, which we know to be $\boldsymbol{k} \cdot \boldsymbol{B} = 0$.

The lowest-energy relaxed state of the system occurs at minimum λ which can have a sign of positive or negative, and a physical interpretation of λ is supplied in Section 3.7. This minimum stability calculation is dependent upon various global parameters, such as pressure and the magnitude of $\boldsymbol{B}$ but the most crucial components are μ, m and κ. As rotational transform can be calculated from wavenumbers, rotational transform rationality that correspond with system minimum stability and marginal stability can be studied.

The initial chosen ranges for minimum stability calculation are $0 < \mu < \pi$, $-20 < m < 20$ and $-20 < \kappa < 20$ with μ step size, $\Delta\mu = \frac{\pi}{800}$ and wavenumber step size $\Delta m = 0.3$ and $\Delta\kappa = 0.3$. For each μ value, a spectrum of λ is calculated and tabulated by sweeping across the κ and m range. The minimum λ value is then selected via the Mathematica function Min, alongwith its corresponding m, κ, and μ values. The rotational transform of the interface is calculated from each μ and plotted against its minimum λ as $\iota\!\!\!-_{\text{interface}}$. This process takes approximately 3 hours and 18 minutes for a full run and calculation time correlates linearly with wavenumber step sizes.

While the choice of μ range is discussed in Section 3.4, the choice of wavenumber range is for comparability purposes with Hole et al. [21], while the step size choice is a matter of computational time cost and accuracy in finding true minimum stability of λ as presented in Section 3.5.1. ‘Mirrored wavenumbers’ may also occur, where two combinations of wavenumbers are found to be identical, but sign inversed, i.e. $m = 1, \kappa = -1$ for $\lambda = 0.1$ and $m = -1, \kappa = 1$ for an identical λ value. The sign change of the wavenumbers reflects magnetic fields travelling in opposite directions, thus producing the same stability results but with mirrored wavenumber values.

A sample from the dataset for the aforementioned variable settings appear in Table 3.1.

$\iota\!\!\!-_{\text{interface}}$	μ	κ	m	Minimum λ
0.560461	0.341648	1.9	-3.5	-0.00197053
0.568153	0.345575	1.6	-2.9	-0.00218405
0.575895	0.349502	-1.4	2.5	-0.00230282

Table 3.1: Dataset sample of minimum λ results using $\theta = -\cot^{-1}\frac{\mu}{2}$.

Fig. 3.14 is produced by plotting the minimum λ values with respect to $\iota\!\!\!-_{\text{interface}}$ where the normalisation, once again, only affects the magnitude of minimum λ as discussed in Section 3.3.

Fig. 3.15 demonstrates the effect of the normalisation value changing between < 1 to > 1 upon minimum λ; the changeover point is marked by the vertical gridlines in Fig. 3.9, one of which corresponds to $\mu = 2.20256$ or $\iota\!\!\!-_{\text{interface}} = -0.105865$ for $\theta = -\cot^{-1}\frac{\mu}{2}$. The

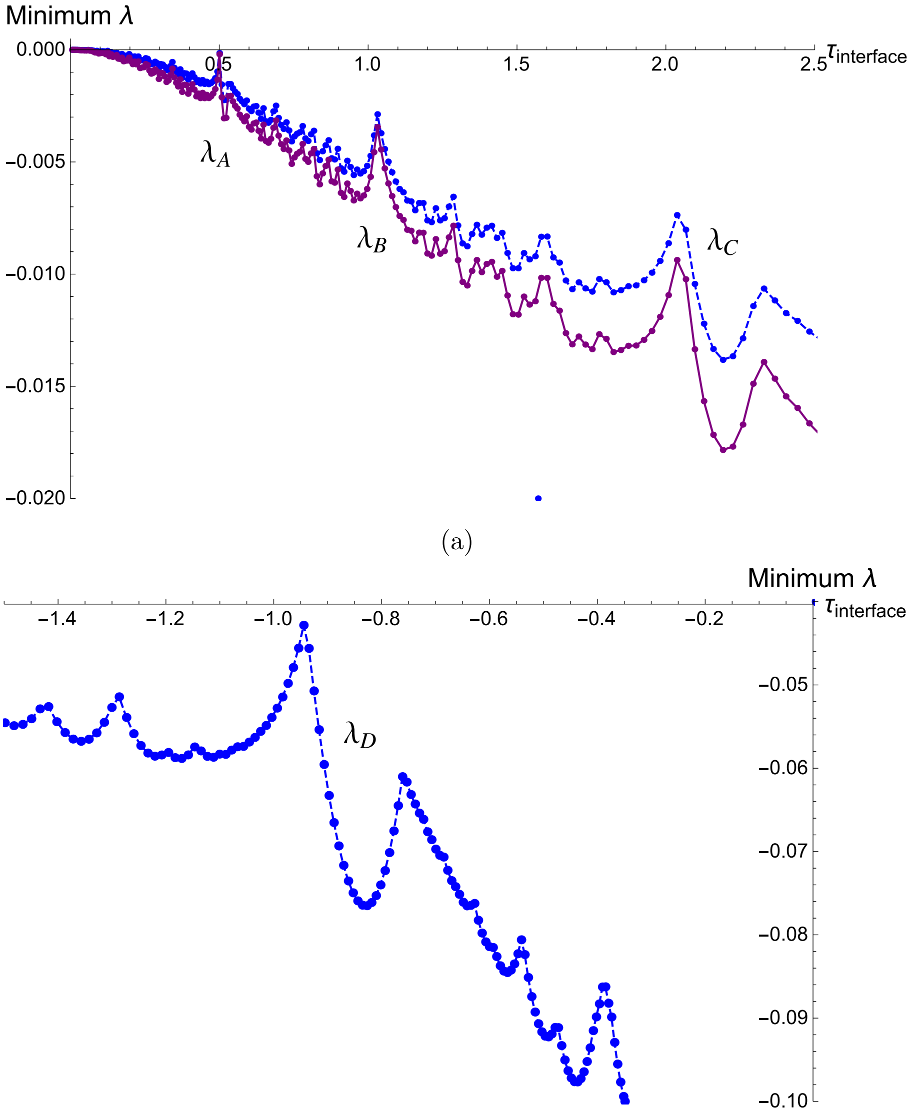

(a)

(b)

Figure 3.14: Minimum $\lambda(N_A)$ (dashed line) and $\lambda(N_B)$ (solid line) for $\pm t_{\text{interface}}$. $\lambda(N_B)$ out of plot range in (b) due to singularity of N_B. $\lambda_A, \lambda_B, \lambda_C, \lambda_D$ denote the conspicuous peak and trough regions, and are investigated further in Section 3.5.3.

change in normalisation value affects the overall trend of minimum λ shown by Figs. 3.14 - 3.15 and does not account for minimum λ magnitude spikes in Fig. 3.14.

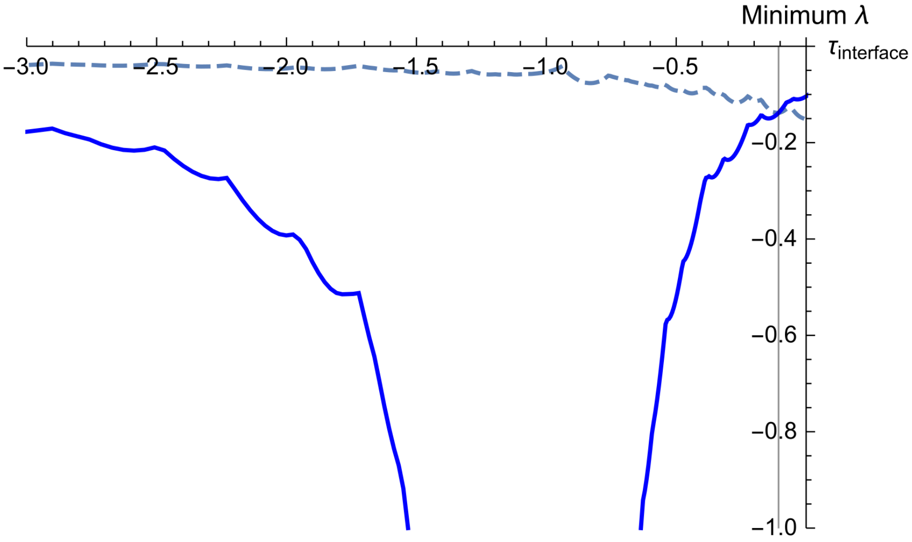

Figure 3.15: Effect of normalisation on minimum $\lambda(N_A)$ (dashed line) and $\lambda(N_B)$ (solid line) in the $-t_{\text{interface}}$ range. The $t_{\text{interface}} = -0.105865$ value is denoted by the grey vertical line.

3.5.1 Wavenumber step size effect on minimum λ

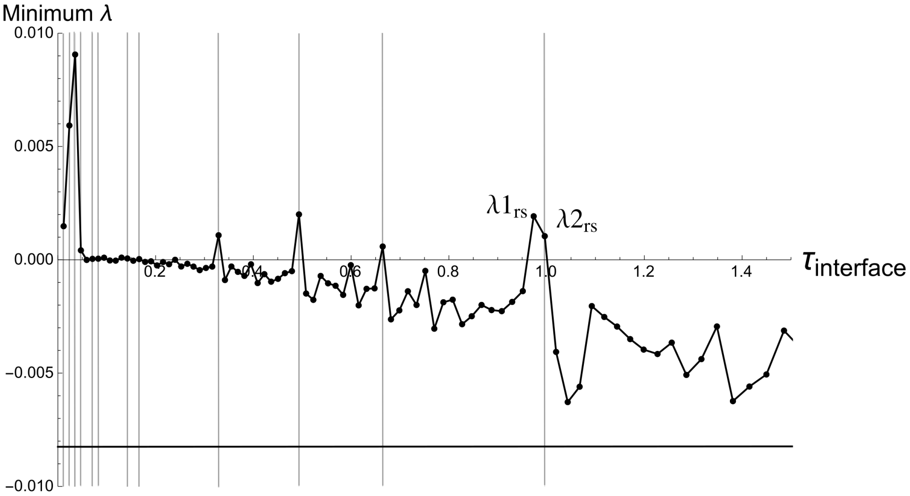

Figure 3.16: Dependence of minimum λ datapoints on wavenumber step sizes shown by $\lambda 1_{\mathrm{rs}}$ and $\lambda 2_{\mathrm{rs}}$, with $\Delta m = 1, \Delta\kappa = 1$.

In Section 3.5, the wavenumber step size used was $\Delta m = 0.3, \Delta\kappa = 0.3$. Using larger step sizes results in less accurate minimum λ values, and is demonstrated in Fig. 3.16 by using $\Delta m = 1, \Delta\kappa = 1$ to obtain minimum λ.

From initial scans of λ across a κ range with nonzero m and varying μ shown by Fig. 3.1, it was found that an unstable λ exists for all non-zero μ values and so minimum λ must be negative[1]; this is corroborated by Fig. 3.14a. However, a lower wavenumber resolution (or larger Δm and $\Delta\kappa$), may result in minimum λ data points which are positive as displayed in Fig. 3.16; this indicates an inaccurate representation of minimum stability due to the low resolution.

To illustrate this claim, the values of $\lambda 2_{\mathrm{rs}}$ are ascertained to be $\mu = 0.526217, \kappa = -1$, and $m = 1$. Fig. 3.17a plots λ for the choice of μ and m associated with $\lambda 2_{\mathrm{rs}}$ across a range of κ. The position of $\lambda 2_{\mathrm{rs}}$ is marked by the vertical gridline. Similarly, Fig. 3.17b plots the location of $\lambda 1_{\mathrm{rs}}(\mu = 0.518363, \kappa = -19$, and $m = 20)$. The positive values of $\lambda 1_{\mathrm{rs}}$ and $\lambda 2_{\mathrm{rs}}$ indicates the chosen Δm and $\Delta\kappa$ in Fig. 3.16 are too large to access the unstable region of their respective λ.

Furthermore, the resonant surfaces of all the data points in Fig. 3.16 are calculated using their associated m, κ, and μ using Eq. (2.25) and Eq. (2.28). The grey vertical lines represent the minimum λ data points with $x_{\mathrm{rs}} > 1$, i.e. resonant surface not within the plasma region. For instance, m and κ of $\lambda 2_{\mathrm{rs}}$ does not correspond to an x_{rs} (Eq. (2.25) and (2.28)) while m and κ of $\lambda 1_{\mathrm{rs}}$ generates $x_{\mathrm{rs}} = 0.976462$.

Tearing instability calculations result in indeterminate $-\Delta'$ for the vacuum region[2], as the vacuum region q-profile is constant and equal to $q_{x_{\mathrm{rs}}=\mathrm{interface}}$. However, λ does not have this limitation as it exists and is stable when there are no associated resonances as explained in Section 3.2.

As the choice of Δm and $\Delta\kappa$ can affect the solution for minimum λ and the existence of resonant surfaces, Δm and $\Delta\kappa$ must ensure minimum λ is negative with $x_{\mathrm{rs}} < 1$ for comparison purposes between λ and $-\Delta'$ models.

---

[1] This is later compared to the work of Goedbloed et. al. in Section 3.8.

[2] To specifically address $x_{\mathrm{rs}} > 1$, $-\Delta'$ must be reformulated again in terms of resonant surfaces existing externally of the plasma region, but will result in the indeterminacy once again.

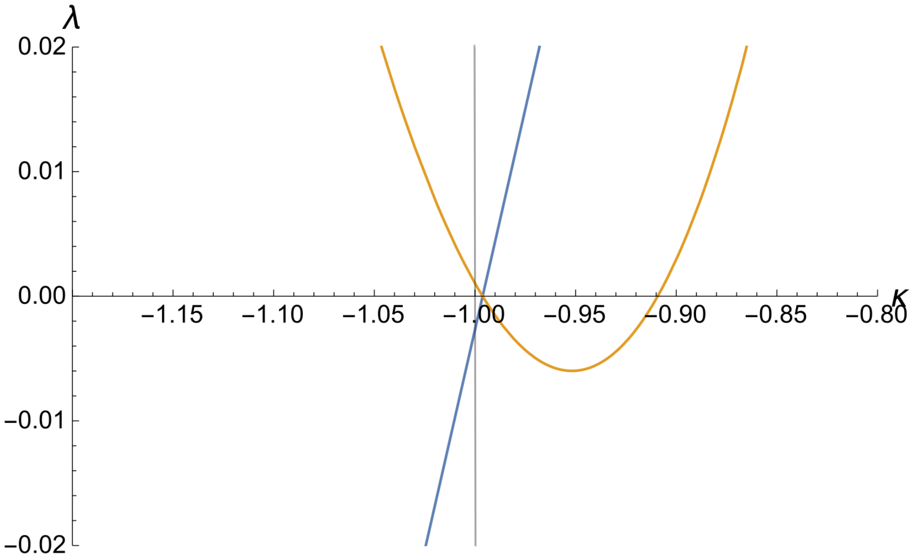

(a) Associated wavenumbers of $\lambda 2_{\text{rs}}$ (vertical gridline) are $\kappa = -1$ and $m = 1$.

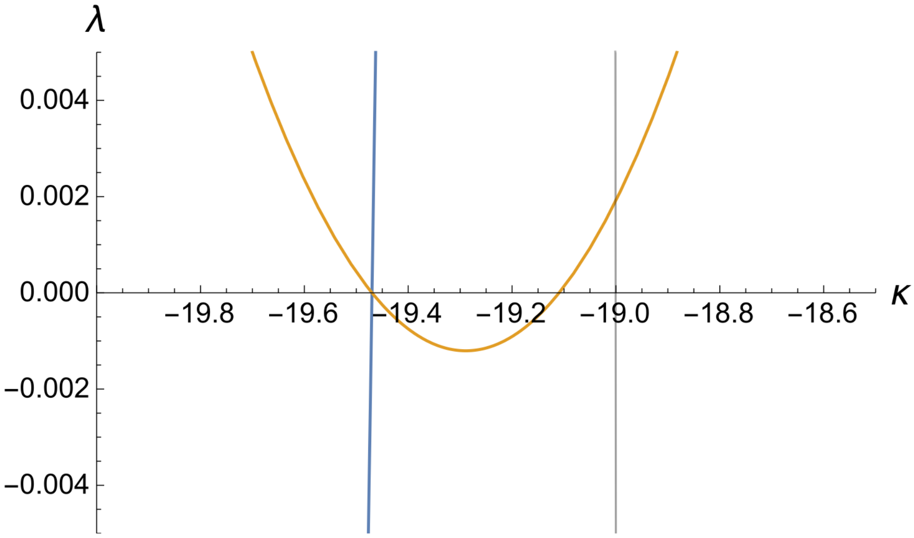

(b) Associated wavenumbers of $\lambda 1_{\text{rs}}$ (vertical gridline) are $\kappa = -19$ and $m = 20$.

Figure 3.17: The locations of $\lambda 1_{\text{rs}}$ and $\lambda 2_{\text{rs}}$ on their respective λ plots and the unstable regions. The linear blue line is $\boldsymbol{k} \cdot \boldsymbol{B}$.

3.5.2 Effects of ι at $x = 0$, or θ

We now analyse the rotational transform $\iota(\theta)$ at $\boldsymbol{B}(x = 0)$, and find that the minimum stability characteristics across a range of ι are essentially independent of θ. This is proven by comparing the two options for $\theta = -\cot^{-1}\frac{\mu}{2}$ and $\theta = -\cot^{-1}\frac{\mu}{4\pi}$ in terms of minimum λ.

By changing θ, the interface rotational transform, $\iota_{\text{interface}}$ is also modified via Eq. (2.24) and (2.25). Fig. 3.18 shows the difference in terms of $\iota_{\text{interface}}$ for the two θ, where $\iota_{\text{interface}}$ is compared at an arbitrary μ, i.e. $\mu = 1.86$ marked by the vertical gridline. The $\iota_{\text{interface}} = -0.583016$ for Fig. 3.18a and $\iota_{\text{interface}} = -2.12374$ for Fig. 3.18b are significantly different values.

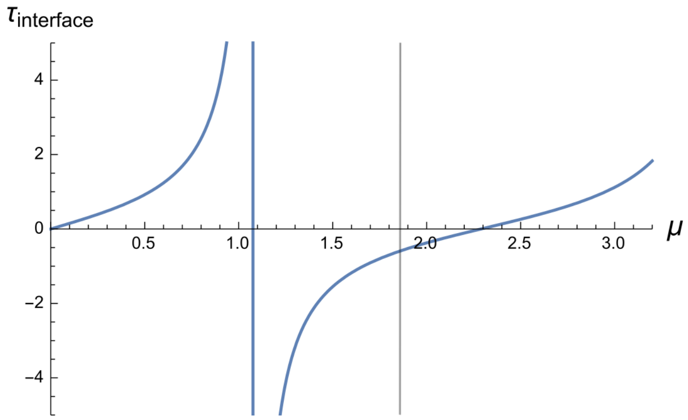

(a) $\iota_{\text{interface}}$ for $\theta = -\cot^{-1}\frac{\mu}{2}$ across a range of μ.

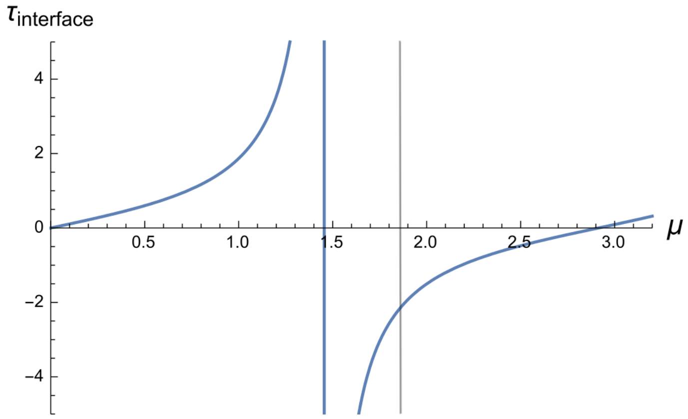

(b) $\iota_{\text{interface}}$ for $\theta = -\cot^{-1}\frac{\mu}{4\pi}$ across a range of μ.

Figure 3.18: Difference in terms of $\iota_{\text{interface}}$ for two θ across a $\mu - range$.

Fig. 3.19 data points result from minimum λ utilising these two θ options, and from inspection, the minimum stability plot values mainly differ in terms of magnitude. This implies the θ, and subsequently, $\iota_{\text{interface}}$ are not criterions for stability, as minimum λ has not significantly shifted along the $\iota_{\text{interface}}$ axis to account for the large difference between $\theta = -\cot^{-1}\frac{\mu}{2}$ and $\theta = -\cot^{-1}\frac{\mu}{4\pi}$.

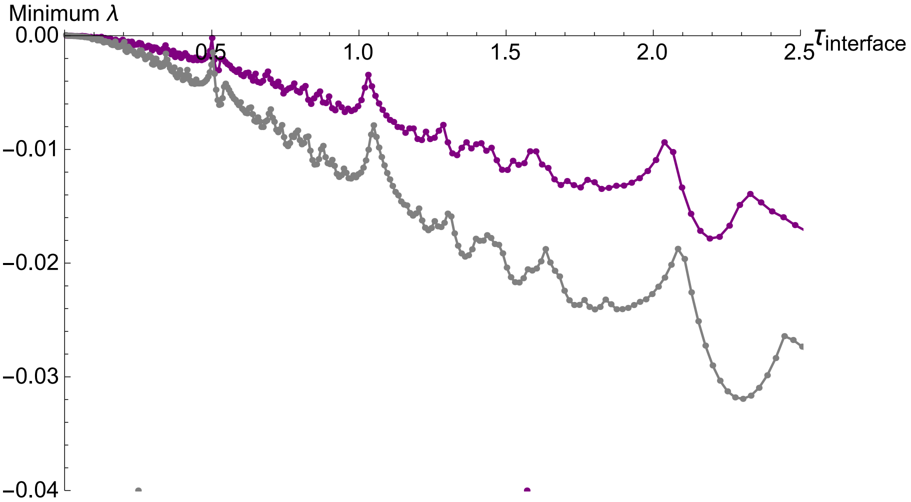

Figure 3.19: Minimum $\lambda(N_B)$ with $\theta = -\cot^{-1}\frac{\mu}{2}$ (purple line), and $\theta = -\cot^{-1}\frac{\mu}{4\pi}$ (gray line).

As $\bar{\iota}$ of minimum λ, represented as $\bar{\iota}_{\mathrm{rs}}$, is not equivalent to interface $\bar{\iota}_{\mathrm{interface}}$ (minimum λ is of $x_{\mathrm{rs}} < 1$), we look to $\bar{\iota}_{\mathrm{rs}}$ for both choices of θ. Fig. 3.20 compares $\bar{\iota}_{\mathrm{rs}}$ from the m and κ for each minimum λ data point. Once again, it is seen there is minimal plot characteristic difference aside from a magnitudinal change. A vertical gridline is provided to enable visual comparison of the minimum λ data points across the two plot lines.

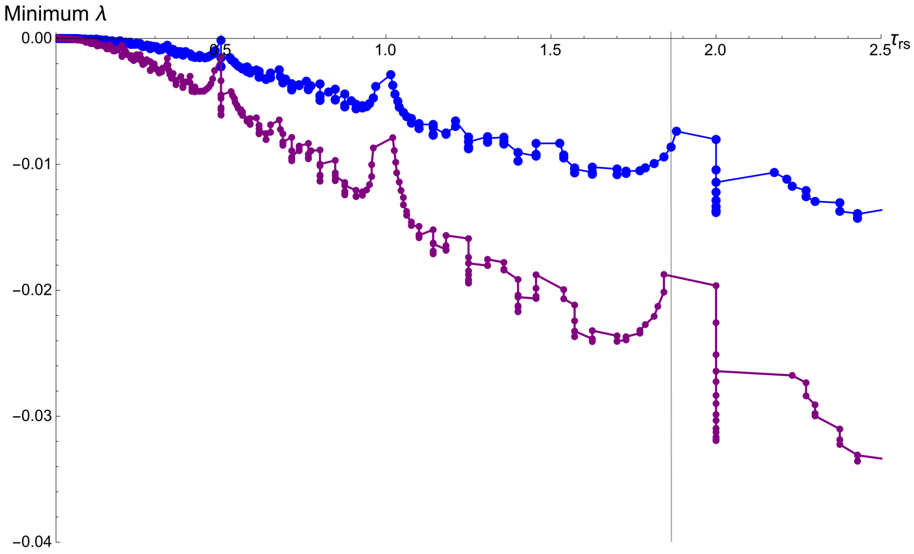

Figure 3.20: $\bar{\iota}_{\mathrm{rs}}$ for $\theta = -\cot^{-1}\frac{\mu}{2}$ (blue line) and $\theta = -\cot^{-1}\frac{\mu}{4\pi}$ (purple line).

This exercise confirms that $\bar{\iota}_{\mathrm{rs}}$ and $\bar{\iota}_{\mathrm{interface}}$ of minimum λ are essentially unchanged with different θ; this is a useful point as $\bar{\iota}$ can be written in terms of wavenumbers m and κ, and later enables the study of its rationality with respect to minimum stability.

The main questions at this point are as follows:

1. What is the relationship between stability characteristics of minimum λ, $\bar{\iota}_{\mathrm{rs}}$ and $\bar{\iota}_{\mathrm{interface}}$?
2. Can the wavenumbers for marginal stability, $\lambda = 0$ assist in investigating the rationality of $\bar{\iota}_{\mathrm{interface}}$?

3.5.3 Peak stability of minimum λ dependence upon the $\iota\!\!\!-_{\mathrm{rs}}$ and $\iota\!\!\!-_{\mathrm{interface}}$

To address the first question, we investigate the behaviour of resonant surfaces in the form of rationals through $\iota\!\!\!-_{\mathrm{rs}} = \frac{-\kappa}{m}$ where m and κ come from the data points of minimum λ. It is found that the minimum λ values correlate to $\iota\!\!\!-_{\mathrm{rs}}$ in terms of high and low-order rationals.

We begin this Section with Fig. 3.21 where the y-axis represents $\iota\!\!\!-_{\mathrm{rs}}$ of all minimum $\lambda(N_A)$ data points in Fig. 3.14. The resulting graph exhibits characteristics of a Cantor function, also known as a Devil's Staircase, due to the monotonically increasing "staircase" at which the plateaus of numbers are rationals while jumps between plateaus are inhabited by irrationals [26, 27]; for our purposes, irrationals are represented as high-order rationals (see Section 3.6).

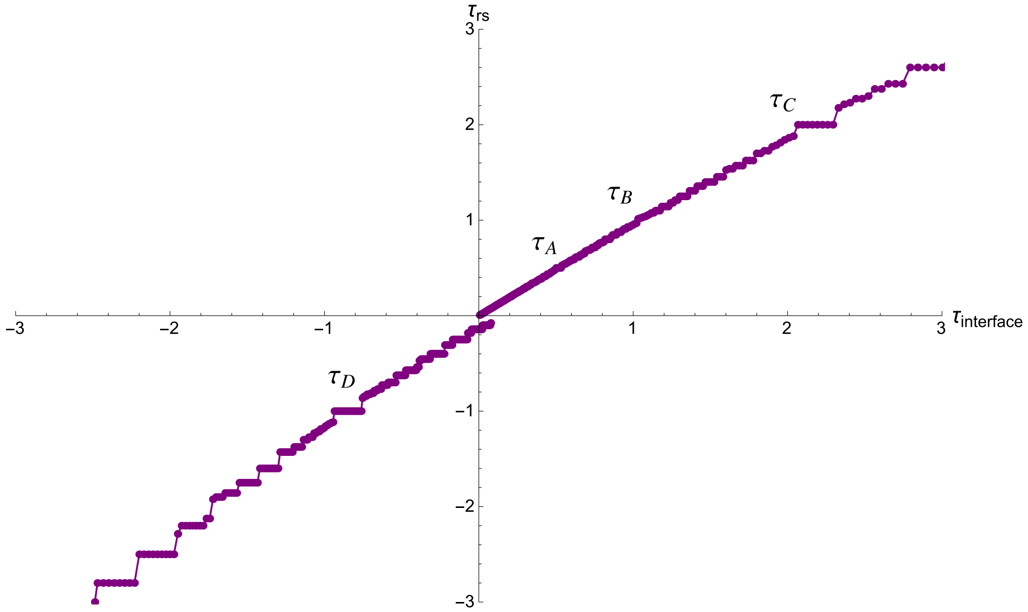

Figure 3.21: $\iota\!\!\!-_{\mathrm{rs}}$ of minimum λ plotted against $\iota\!\!\!-_{\mathrm{surface}}$. Four regions of interest are marked as $\iota\!\!\!-_A$, $\iota\!\!\!-_B$, $\iota\!\!\!-_C$, and $\iota\!\!\!-_D$.

The left column of Fig. 3.22 presents the four regions of interest ($\lambda_A - \lambda_D$) labelled in Fig. 3.14. These regions of minimum λ have a corresponding plot of its $\iota\!\!\!-_{\mathrm{rs}}$ (labelled as $\iota\!\!\!-_A - \iota\!\!\!-_D$ in Fig. 3.21) on the right column of Fig. 3.22.

Data points of interest are marked by vertical gridlines and are related in the following fashion: the first vertical gridline on the left in Fig. 3.22a corresponds to the first vertical gridline in Fig. 3.22b, and so on.

In Table 3.2, $\iota\!\!\!-_{\mathrm{rs}}$ of Fig. 3.22 marked data points are listed in terms of rationals by taking $\iota\!\!\!-_{\mathrm{rs}} = \frac{-\kappa}{m}$ and applying the Mathematica function *Rationalize*. Firstly, note that the peak minimum λ values generally consists of a higher order rational, i.e. large integers for the numerator and denominator, and is larger than its neighbouring data points, with Fig. 3.22a being the outlier.

Secondly, it is found that the peak rationals of Table 3.2 rests just before a plateauing value of $\iota\!\!\!-_{\mathrm{rs}}$ as shown in Figs. 3.22e - 3.22f, and Figs. 3.22g - 3.22h, with Figs. 3.22a - 3.22b as the outlier once again.

The disagreement of data in Figs. 3.22a - 3.22b with the other regions of interest is an example of the importance in using sufficiently high resolution. The discrepancy is proven

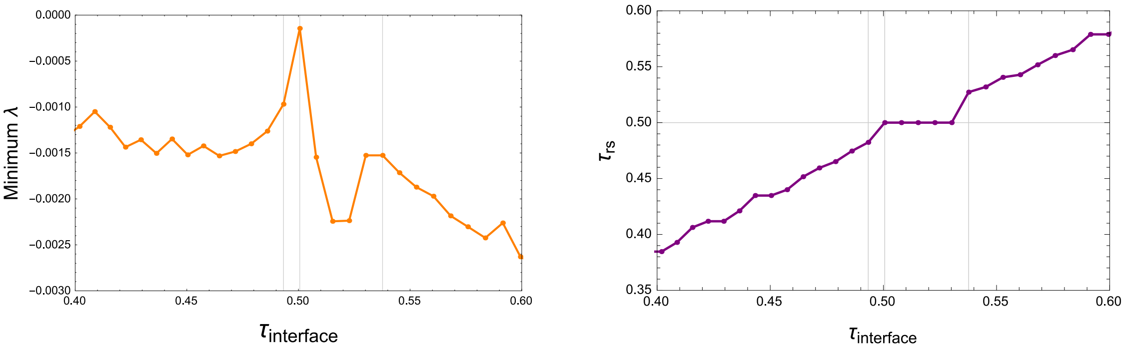

(a) The λ_A region of minimum λ in Fig. 3.14. (b) The $ƚ_A$ region of Fig. 3.21.

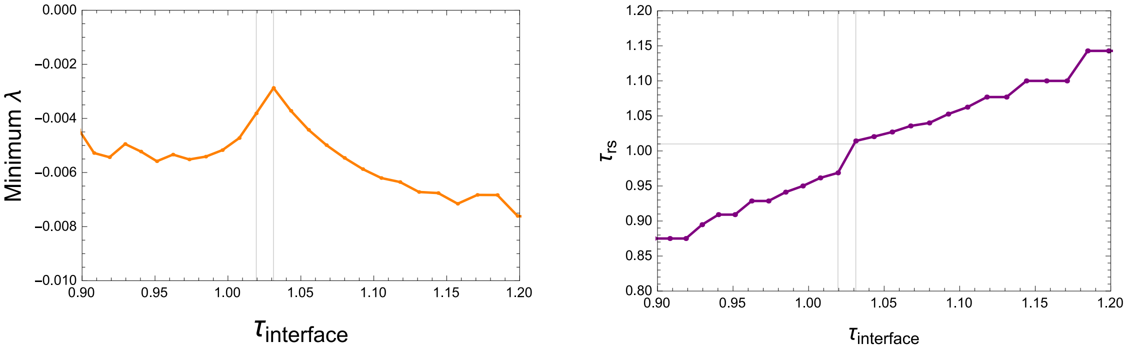

(c) The λ_B region of minimum λ in Fig. 3.14. (d) The $ƚ_B$ region of Fig. 3.21.

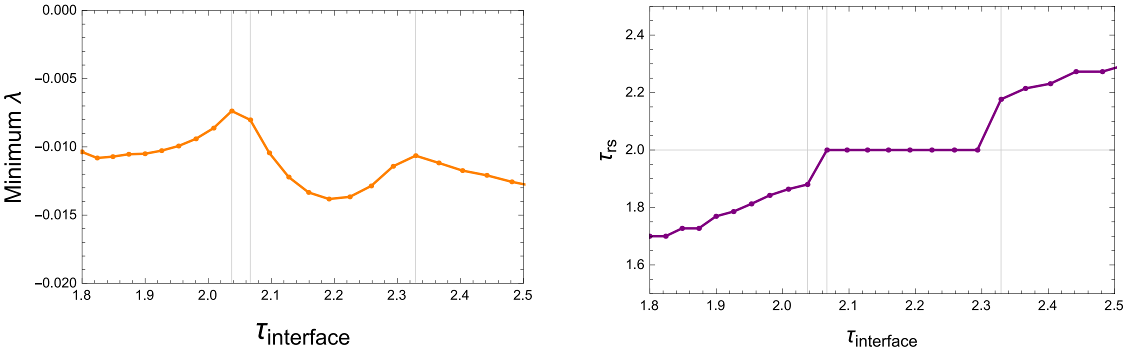

(e) The λ_C region of minimum λ in Fig. 3.14. (f) The $ƚ_C$ region of Fig. 3.21.

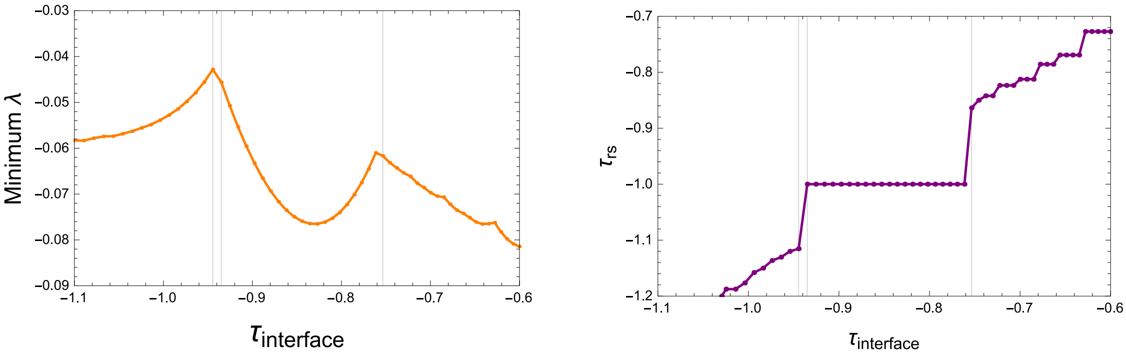

(g) The λ_D region of minimum λ in Fig. 3.14. (h) The $ƚ_D$ region of Fig. 3.21.

Figure 3.22: Peak and trough characteristics of minimum λ and its associated resonant surface.

Fig.	Vertical gridline (left)	Vertical gridline (middle)	Vertical gridline (right)
Fig. 3.22a	$\frac{41}{85}$	2(peak)	$\frac{29}{55}$
Fig. 3.22c	$\frac{31}{32}$	$\frac{71}{70}$(peak)	-
Fig. 3.22e	$\frac{47}{25}$(peak)	$\frac{2}{1}$	$\frac{37}{17}$
Fig. 3.22g	$-\frac{29}{26}$(peak)	$-\frac{1}{1}$	$-\frac{19}{22}$

Table 3.2: Dataset of $\iota\!\!\!-$ at minimum $\lambda(\theta = -\cot^{-1}\frac{\mu}{2})$.

to be an artefact of $\Delta\mu$ choice; in Fig. 3.23, $\iota\!\!\!- \in (0.493305, 0.507923)$[3], is divided into 20 smaller data points for minimum λ recalculation. The dashed gridline denotes the location of the peak in Fig. 3.22a as comparison; the new peak minimum λ value has shifted to the left of this line.

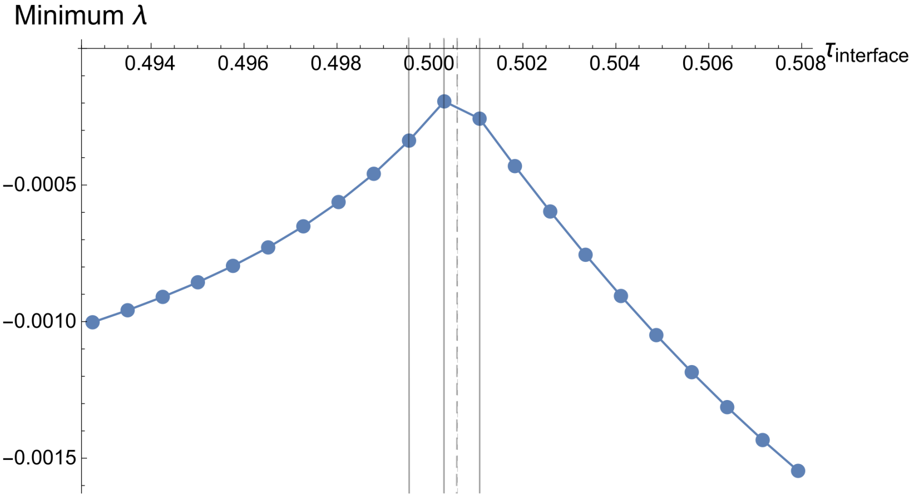

Figure 3.23: Minimum λ_A region with smaller $\Delta\mu$.

The new peak minimum λ value and its neighbouring data points are marked along the vertical solid gridlines of Fig. 3.23 and its rationals are listed in Table 3.3. The new set of data agrees with initial findings where the peak value for a region of interest is of the largest (or highest-order) rational among its neighbouring data points.

Fig.	Vertical gridline (left)	Vertical gridline (middle)	Vertical gridline (right)
3.23	$\frac{73}{149}$	$\frac{76}{155}$(peak)	$\frac{1}{2}$

Table 3.3: Rationals of gridlines in Fig. 3.23

Next, the dips in minimum λ, or troughs, are addressed; these regions of stability appear as plateaus on the right column plots of Fig. 3.22. The plateaus are of low-order rationals, i.e. $\frac{2}{1}$ as seen in Fig. 3.22f, and the wavenumbers of the trough region are all identical, i.e. Fig. 3.24 represents a minimum λ trough, and two arbitrary data points marked within the trough are of $m = 0.1$ and $\kappa = -0.2$.

---

[3] This range consists of three data points around the peak value of Fig. 3.22a, and their μ-values are $\mu = 0.306, 0.310232, 0.314159$.

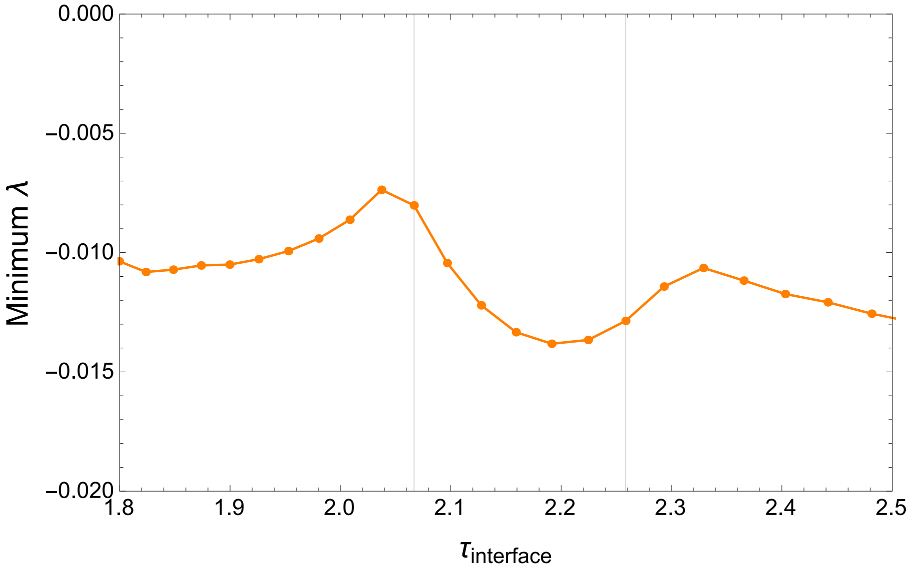

Figure 3.24: A minimum λ trough around $\iota\!\!\!-_{\text{interface}} = 2.0$.

A well-defined trough of minimum λ (and plateau in $\iota\!\!\!-_{\text{rs}}$), supports tearing instability theory where low order resonant wavenumbers are destabilising in a chosen system. The width of the $\iota\!\!\!-_{\text{rs}}$ plateau is reduced by higher order rational approximations with higher wavenumber resolution, while the plateau itself is localised around a low-order rational, later shown in Fig. 3.31.

Fig. 3.25 compares minimum λ with $\Delta m = 0.3$ and $\Delta\kappa = 0.3$, with minimum λ obtained with machine-precision wavenumber values (a labour-intensive manual process!). However, the minimum λ value at the middle of the trough is similar if not identical for both wavenumber resolution choices; this indicates the minimum λ at the middle of troughs are robust against increasing wavenumber resolution and this reasoning also applies to the plateaus of rational $\iota\!\!\!-_{\text{rs}}$. The $\iota\!\!\!-_{\text{rs}}$ at the middle of plateaus have therefore been found at lower wavenumber resolutions and represent lower-order rationals. Put another way, the low-order rationals inhabit the zero slope (plateau) areas of $\iota\!\!\!-$ while lowest-order rationals are in the middle of plateaus.

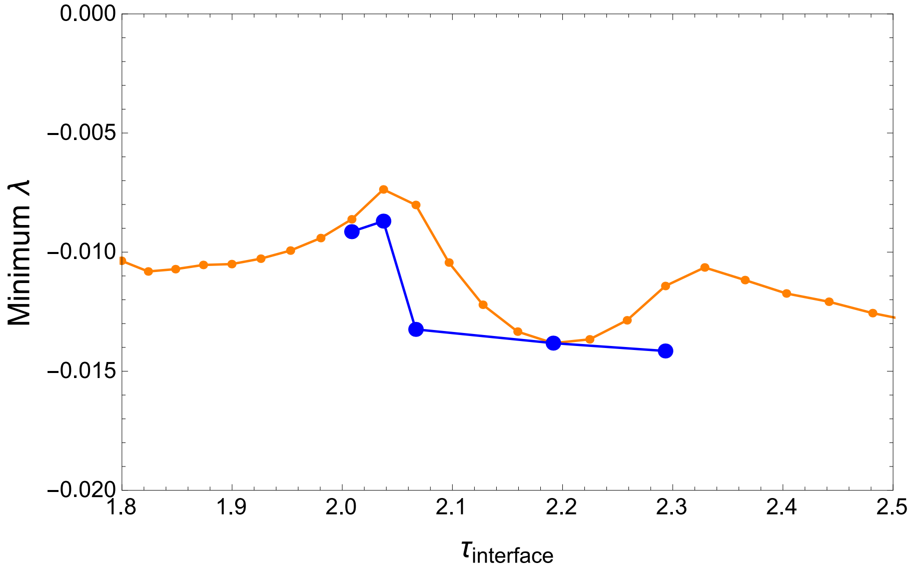

Figure 3.25: λ with $\Delta m = 0.3$ and $\Delta\kappa = 0.3$ (orange line), and λ with machine-precision wavenumbers (blue line).

Finally, we prove that the findings so far in terms of high-order rationals (or large wavenumber values) and least instability are valid for the full dataset of Fig. 3.14. The Mathematica function *Rationalize* is used to obtain $\frac{-m}{\kappa}$ in the form of $\frac{p}{q}; p, q \in integers$. Fig. 3.26 is the result of scanning the wavenumbers associated with all minimum λ data points. Any ι_{rs} rational consisting of a numerator or denominator value of over 10 (dotted gridlines) and 20 (solid gridlines) is marked with a gridline. As expected, Fig. 3.26 demonstrates that higher-order rationals dominate least unstable minimum λ.

In conclusion, least unstable minimum λ values consist of high-order rational resonant surfaces or ι_{rs}, and most unstable minimum λ values are related to low-order rationals.

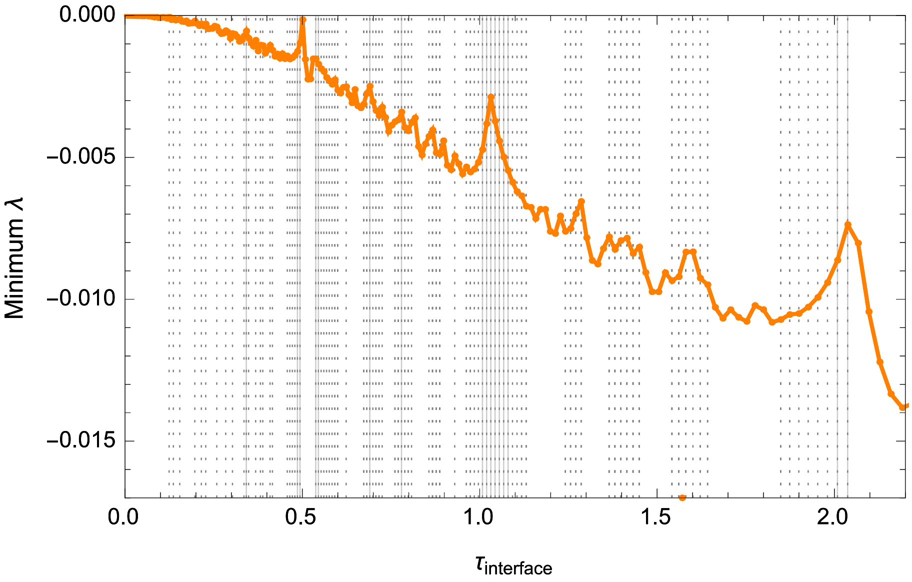

(a) Positive $t_{\text{interface}}$ region.

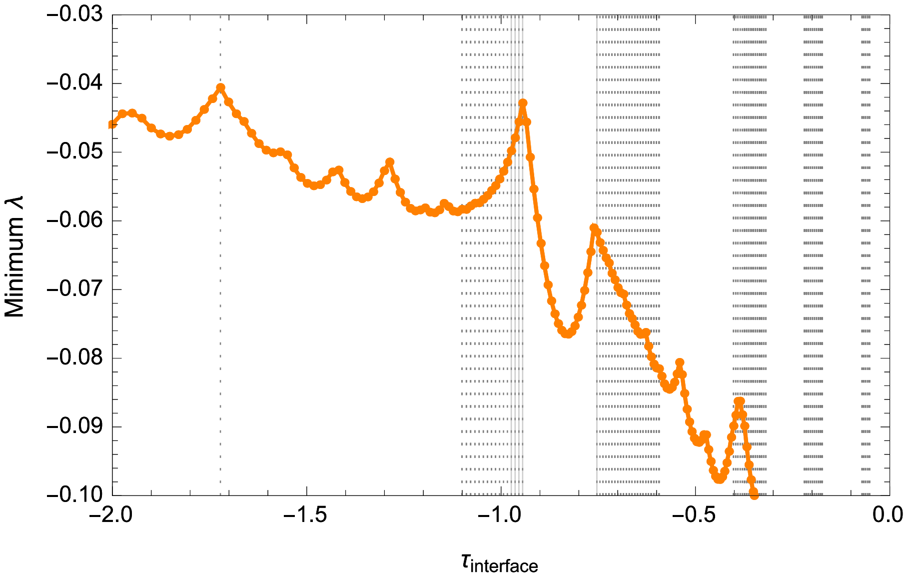

(b) Negative $t_{\text{interface}}$ region.

Figure 3.26: Minimum λ data points of high-order rationals.

3.5.4 Can the wavenumbers for marginal stability, $\lambda = 0$ assist in investigating the rationality of $\iota\!\!\!-_{\text{interface}}$?

From the analysis in previous Sections, minimum stability is determined by the resonant surface rotational transform, where a high-order rational, or large wavenumbers, contribute to a less unstable system. It was also determined that instability seen by the plasma-slab system in the region of minimum λ, is due to tearing instability.

However, both of these observations are linked to resonances within the plasma; we now endeavour to analyse the rotational transform of the interface ($\iota\!\!\!-_{\text{interface}}$) between plasma and vacuum which is an ideal MHD surface. The resulting analysis detailed in this Section will show that system marginal stability correlates with lowest-order rationals in a wavenumber set, while previous findings of minimum λ and its relation to high-order rationals are seen once again. The identification of high and low-order rationals are performed via the plateaus and plateau jumps, or Devil's Staircase theory, which also appear in this Section.

We begin the analysis by using $m = 1$ as a starting point in analysing $\lambda = 0$; a fixed m allows minimum λ to reach marginal stability. Fig. 3.27 shows minimum λ calculated once again with $\Delta\kappa = 0.3$ and $\Delta\kappa = 0.1$. Peak stability points for $\lambda_{\Delta\kappa=0.3}$ are marked as λ_P and marginal stability is λ_Z.

From Fig. 3.27, the property $N(\lambda_z)$ or number of λ_z is dependent upon $\frac{1}{\Delta\kappa}$ and is visually noticeable. The minimum λ peak and trough characteristics, and the number of peaks, are more pronounced when compared to minimum λ using smaller $\Delta\kappa$, i.e. purple data points using $\Delta\kappa = 0.1$.

Fig. 3.28 shows the resonant surfaces for minimum λ going through a transition between $x_{\text{rs}} < 1$ and non-existent x_{rs} (as explained previously by Fig. 3.8) for data points of $\Delta\kappa = 0.3$. The horizontal gridline at $x_{\text{rs}} = 1$ (or $x_{\text{interface}}$) marks the boundary between plasma and vacuum. The lines annotated as λ_P and λ_Z are overlaid from Fig. 3.27. The gaps between λ_P and λ_Z in Fig. 3.28 are due to no x_{rs} in the plasma region, and corresponds with stability (no tearing instability).

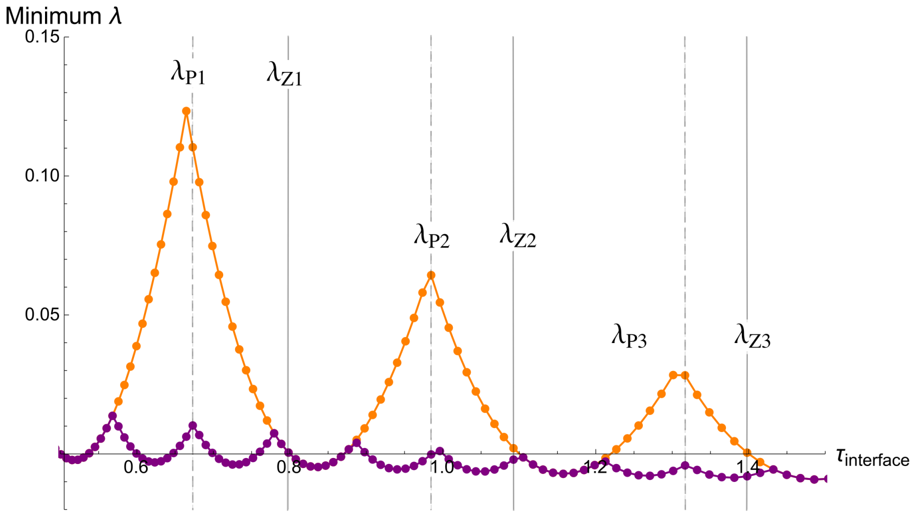

Figure 3.27: Minimum λ for $m = 1$, $\Delta\kappa = 0.3$ (orange points), $\Delta\kappa = 0.1$ (purple points).

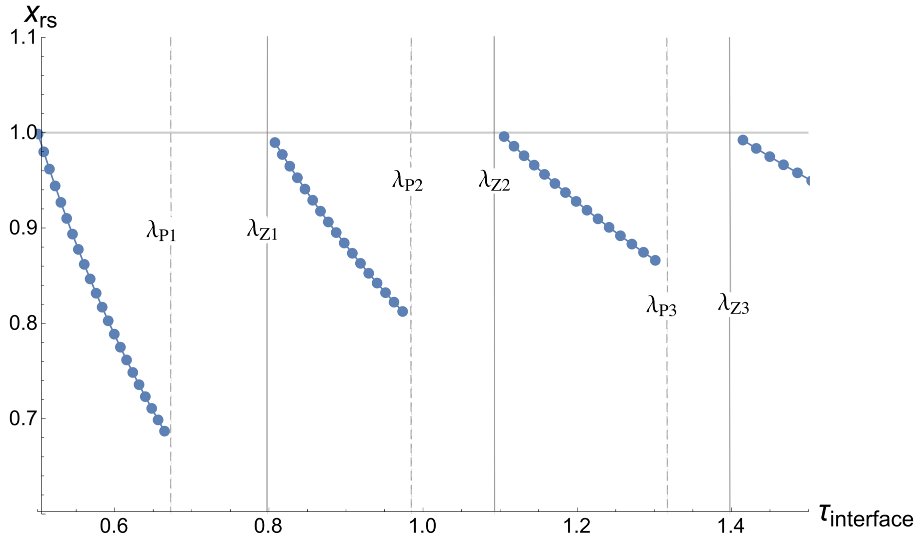

Figure 3.28: Location of resonant surface in the plasma-vacuum model for $m = 1, \Delta\kappa = 0.3$.

Now that minimum λ exhibits marginal stability values and the nature of their resonant surfaces are known, we proceed to utilise $\boldsymbol{k} \cdot \boldsymbol{B} = 0$ for further analysis. It was shown in previous Sections that marginal stability, $\lambda(x_{\text{interface}}) = 0$ is equal to $\boldsymbol{k} \cdot \boldsymbol{B} = 0$. Therefore the wavenumbers and $ɫ_{\text{interface}}$ required for marginal stability can be easily obtained via the latter equation.

Fig. 3.29 displays the relationship between λ and $\boldsymbol{k} \cdot \boldsymbol{B}$, where the lowest magnitude of $\boldsymbol{k} \cdot \boldsymbol{B}$ is calculated for the same choice of μ, m and $\Delta\kappa$ as provided for the minimum λ data points of Fig. 3.27. The $\Delta\kappa$ choice also affects $N(\boldsymbol{k} \cdot \boldsymbol{B} = 0)$ and will later inform upon the number of plateaus and low-order rationals in Fig. 3.31.

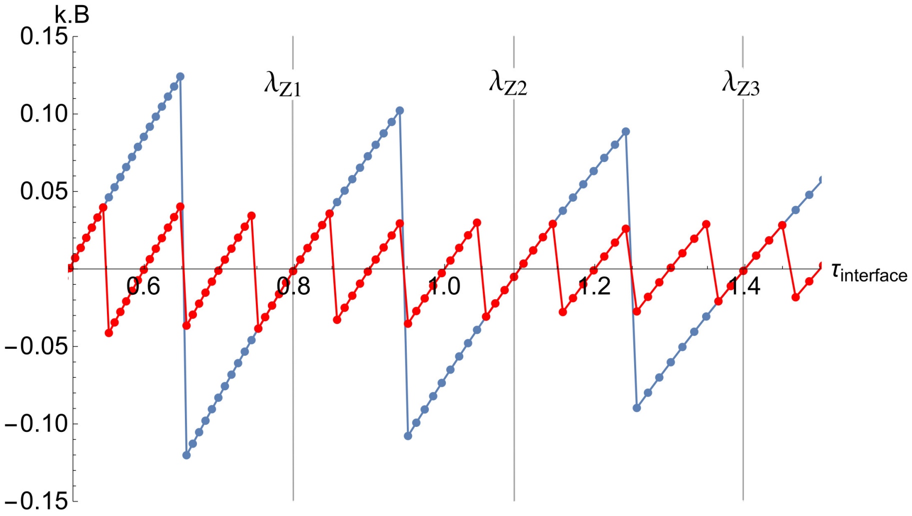

Figure 3.29: $\boldsymbol{k} \cdot \boldsymbol{B}$ for $m = 1$, and κ of each λ_{min} datapoint in Fig. 3.27. The two datasets are represented by the blue ($\Delta\kappa = 0.3$) and red lines ($\Delta\kappa = 0.1$), where $\lambda_z = \boldsymbol{k} \cdot \boldsymbol{B} = 0$.

Fig. 3.29 data points can now provide $ɫ_{\text{interface}}$ via $ɫ_{\boldsymbol{k} \cdot \boldsymbol{B}} = \frac{-\kappa}{m}$. Fig. 3.30a represents these $ɫ_{\boldsymbol{k} \cdot \boldsymbol{B}}$ data points where a clear "staircase" pattern exists. Due to the pronounced peak and trough characteristics seen in Fig. 3.27, predictably, Fig. 3.30b which represents $ɫ_{\text{rs}}$ also reflects a pronounced "staircase" effect.

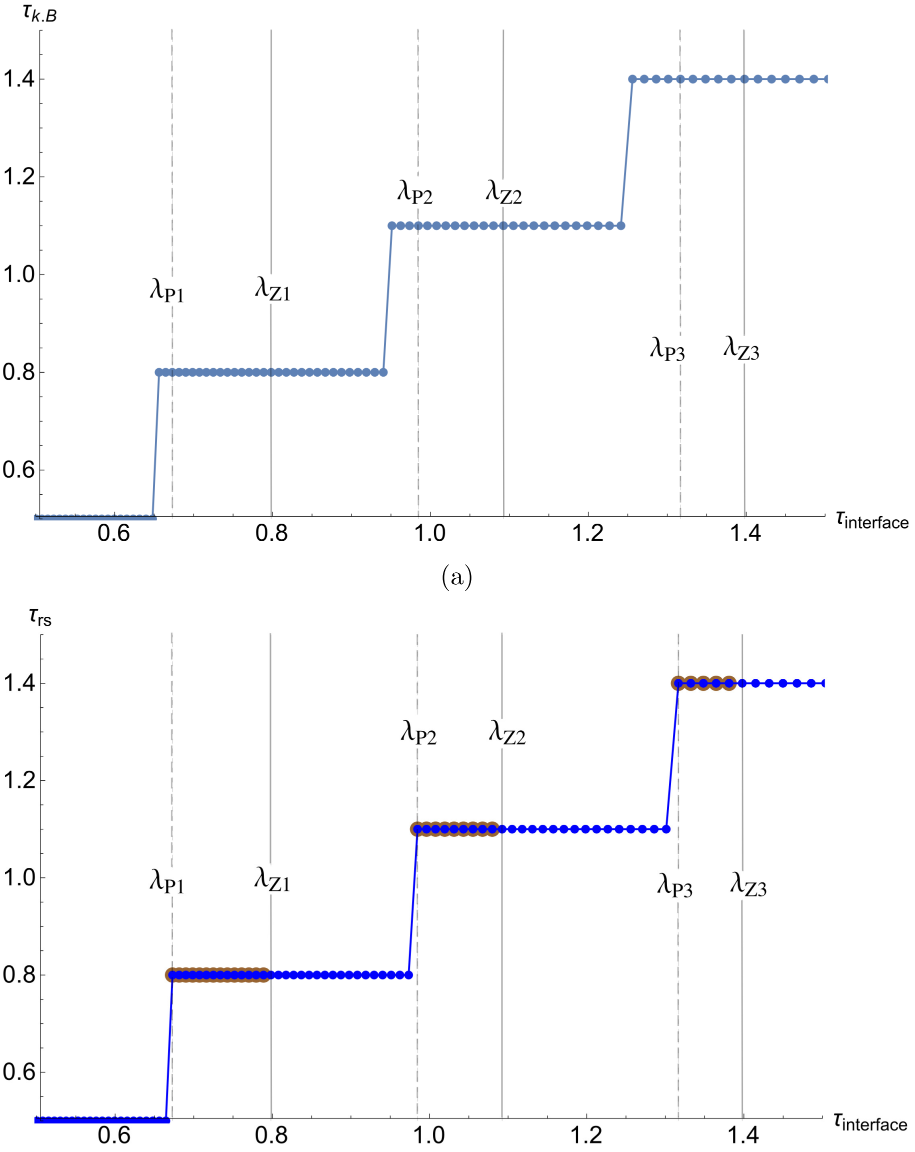

(a)

(b)

Figure 3.30: (a) $\iota_{\boldsymbol{k}\cdot\boldsymbol{B}}$ for the blue $\boldsymbol{k}\cdot\boldsymbol{B}$ datapoints of Fig. 3.29, and (b) ι_{rs} for minimum λ of $m = 1$. The brown data points in (b) have no x_{rs} within the plasma.

Fig. 3.30a exhibits the relationship between $\iota_{\boldsymbol{k}\cdot\boldsymbol{B}}$ and λ_Z, while Fig. 3.30b compares ι_{rs} and λ_P. It is firstly noted that previous minimum λ findings in terms of high-order rationals are supported; the peak stability data points, λ_P, have rotational transforms that are at the edge of ι_{rs} plateaus in Fig. 3.30b, where the jump between plateaus signify a region of high-order rationals.

The second point of interest is that λ_Z is located in the middle of the $\iota_{\boldsymbol{k}\cdot\boldsymbol{B}}$ plateaus in Fig. 3.30a. The $\iota_{\text{interface}}$ of λ_Z is then of the lowest-order rational for its plateau, due to the localisation of plateaus around low-order rationals (see Section 3.5.3). These two findings are also supported by Hudson [23] in which highest-order rationals are furthest from low-order rationals.

As presented in Fig. 3.31, the relationship between $\iota_{\boldsymbol{k}\cdot\boldsymbol{B}}$ and $\lambda = 0$ in terms of rationals is maintained for different $\Delta\kappa$, where the red data points are the $\iota_{\boldsymbol{k}\cdot\boldsymbol{B}}$ of $\Delta\kappa = 0.1$. The λ_Z locations for $\Delta\kappa = 0.3$ are maintained as the middle of the new $\Delta\kappa = 0.1$ plateaus.

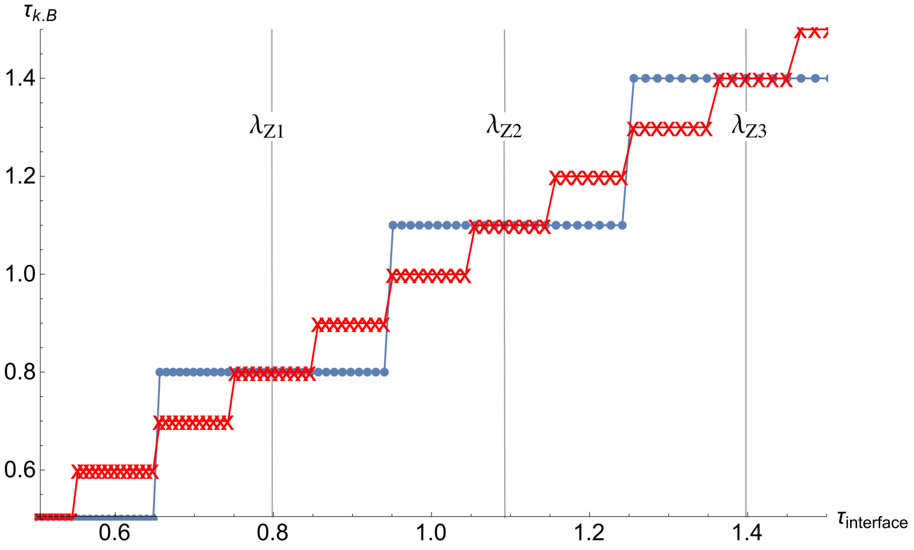

Figure 3.31: $\iota_{k.B}$ for $\Delta\kappa = 0.3$ (blue line) and $\Delta\kappa = 0.1$ (red line).

Fig. 3.31 indicates the number of plateaus, plateau transitions, and plateau widths are determined by $\Delta\kappa$; its fundamental physical significance lies in the increasing κ number set with smaller $\Delta\kappa$, which increases the subset of rationals for resonant surfaces in the plasma-vacuum system both at minimum stability and marginal stability. Nevertheless, even with a larger rational subset, the rotational transform of $\lambda(x_{\text{interface}}) = 0$ is consistently of a low-order rational.

In summary, marginal stability corresponds with low-order rationals, and minimum λ has further confirmation of dependency with high-order rationals.

As it is known that the rotational transform at $x = 0$ (bottom of plasma slab) identified as θ will determine the value for $\iota_{\text{interface}}$, $\theta = \frac{\mu}{4\pi}$ is used in place of $\theta = \frac{\mu}{2}$ to discern if $\iota_{\boldsymbol{k}\cdot\boldsymbol{B}=0}$ conforms to lowest-order rationals. Figs. 3.32 - 3.33 present the resulting minimum λ and $\iota_{\boldsymbol{k}\cdot\boldsymbol{B}}$ data. From the location of λ_Z in these Figures, $\iota_{\boldsymbol{k}\cdot\boldsymbol{B}=0}$ and subsequently, $\lambda(x_{\text{interface}}) = 0$ do not depend on θ, but on lowest-order rationals for the plasma-vacuum interface rotational transform.

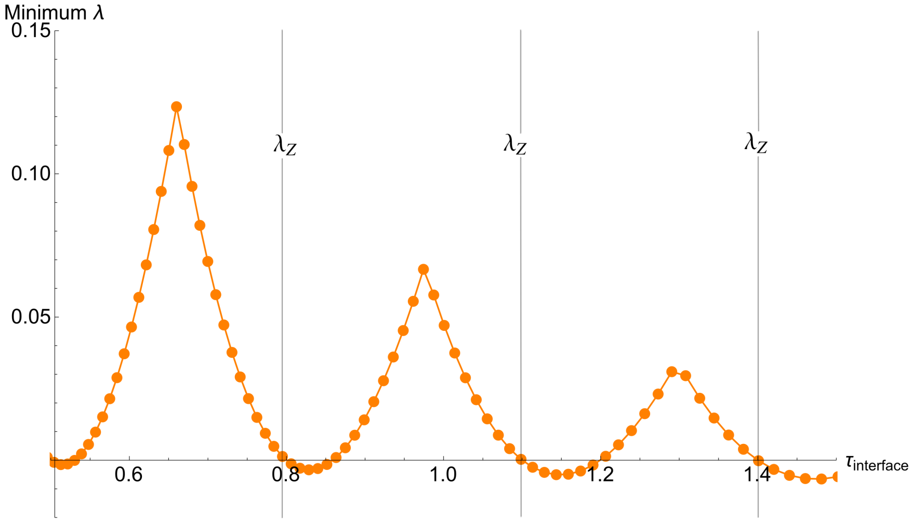

Figure 3.32: Minimum λ with $m = 1$, $\Delta\kappa = 0.3$ and $\theta = \frac{\mu}{4\pi}$.

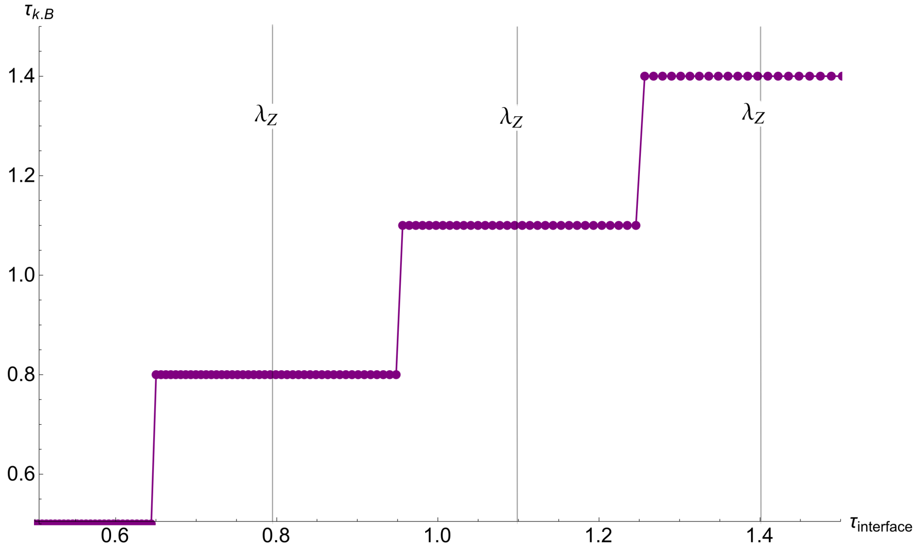

Figure 3.33: $ɨ_{\boldsymbol{k}\cdot\boldsymbol{B}}$ for $\boldsymbol{k}\cdot\boldsymbol{B}$ with m and κ of each Fig. 3.32 $\lambda_{\min}$ datapoints.

To conclude this Section, marginal stability and $ɨ_{\text{interface}}$ are dependent upon low-order rationals, and this is in contrast to minimum λ where its $ɨ_{\text{rs}}$ requires a high-order rational for maximum stability. The staircase pattern in $ɨ_{\text{rs}}$ and $ɨ_{\boldsymbol{k}\cdot\boldsymbol{B}}$ with Devil's Staircase characteristics [27] has proven to be significantly useful in determining high-order and low-order rationals.

Studying the behaviour of $ɨ_{\text{interface}}$ in terms of higher-order rationals requires the addition of pressure, β, for the plasma region of our slab model. This may allow the inclusion of pressure-driven instabilities such as sausage instabilities which contribute to marginal stability conditions in terms of wavenumber values as shown in Fig. 4.24 of Boyd and Sanderson [4], and the effects of $\beta \neq 0$ for the slab system is discussed in Section 3.9.

3.6 Greene's Theorem for Irrational $ɨ_{\mathrm{rs}}$

The usage of $ɨ$ staircase attributes for high and low order rationals seems simple, yet has provided an uncomplicated method to locate desired rationals. As specified in Section 1.2, irrational $ɨ_{\mathrm{interface}}$ contributes to flux surface formations at the interface in 3D systems. While the work in this Thesis does not address flux surface formation, it is of interest to understand how irrationality affects minimised λ. This Section outlines a theorem for identifying irrational numbers and its feasibility for the purposes of this Thesis.

Irrational numbers are classified as real numbers that cannot be represented as a fraction. However, irrationals can be approximated as high order rationals [5], and so with the staircase attribute of $ɨ$, irrationals inhabit the regions of plateau transitions. So while it is now known that $ɨ_{\mathrm{interface}}$ at $\lambda = 0$ is of a low-order rational and furthest away from plateau transitions, this Section will proceed with the study of $ɨ_{\mathrm{rs}}$ in terms of irrationals.

Reaching an irrational number for $ɨ_{\mathrm{rs}}$ is essentially not possible, as *Mathematica* has a fixed digit size as with any computer-dependent program, and so cannot provide a truly continuous irrational number. Greene's theorem is a robust method of obtaining irrational approximations, which is based on continued number fraction theory [23, 32]. Through this theorem, an irrational approximation is characterised by an arbitrary length sequence 1's in its continued fraction representation. For instance, the Golden Mean is the most irrational number (or noble irrational) [31], and its continued fraction representation is $\{1, 1, 1, 1, 1, 1, 1, 1, 1, 1, ...1_{\infty}\}$. Note that the irrational approximations do not require an infinite sequence of 1's.

Greene's theorem, however, has a certain drawback, mainly the increase in computational time required to obtain precise irrational approximations. To demonstrate this claim, a region of data is selected from the minimum λ data points introduced earlier on in this thesis, namely Figs. 3.22c - 3.22d. This choice is due to the lack of a clear trough region for this range of minimum λ, and hence less no clear plateau transition for the identification of irrational approximations.

The analysis begins with Fig. 3.34, in which Fig. 3.34a represents a region of minimum λ selected and denoted by the vertical dashed gridlines. Fig. 3.34b shows the corresponding $ɨ_{\mathrm{rs}} \in (0.909091, 1.03571)$ (marked by the red horizontal gridlines) for this chosen minimum λ range. The solid red vertical gridline passing through the peak data point of Fig. 3.22c is used as a guide to enable visual comparison of data points between the Figures of Fig. 3.34.

Applying Greene's theorem to $ɨ_{\mathrm{rs}} \in (0.909091, 1.03571)$ requires the Mathematica function *ContinuedFraction* which provides the continued fraction representation of a given number. The amount of decimal places in a given number corresponds to the length of the continued fraction representation, i.e. π with its infinite decimals has an infinite continued fraction representation. Ergo, to obtain a satisfactorily long string of 1's in a continued fraction representation, the numbers in a set must have many decimal places and this can be achieved by 'slicing' the $ɨ_{\mathrm{rs}}$ range with a small $\Delta ɨ$ value, or $ɨ$ step size.

Through an iterative process, two continued fraction numbers which qualify as irrational approximations are found in the $ɨ_{\mathrm{rs}}$ range and listed in Table 3.4. The $\Delta ɨ$ required an increase from 10 steps as seen in Fig. 3.22d, to 12,662,338 equidistant steps, a factor of over 1,000,000, to obtain these irrational approximations.

As $ɨ$ can be represented as a rational and hence provide m and κ, Greene's Theorem provides an estimate of the required wavenumber resolution to obtain precise irrational

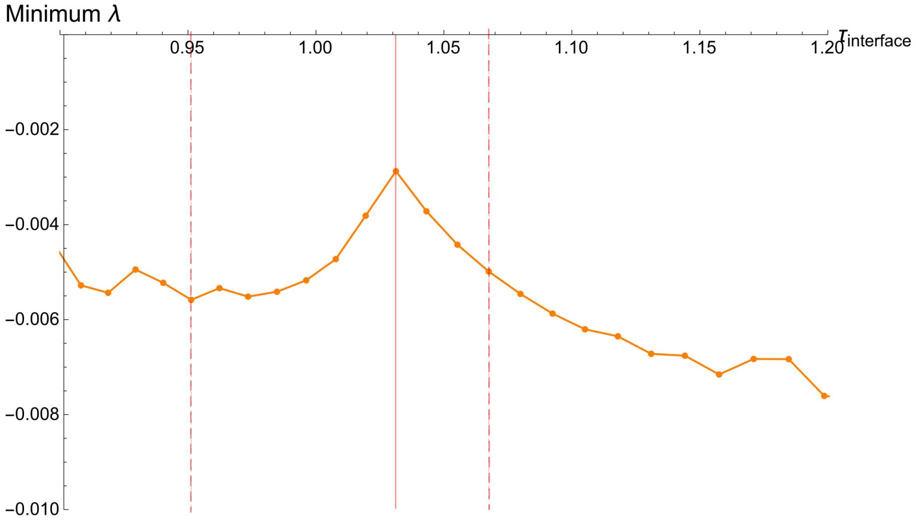

(a) Reproduction of Fig. 3.22c.

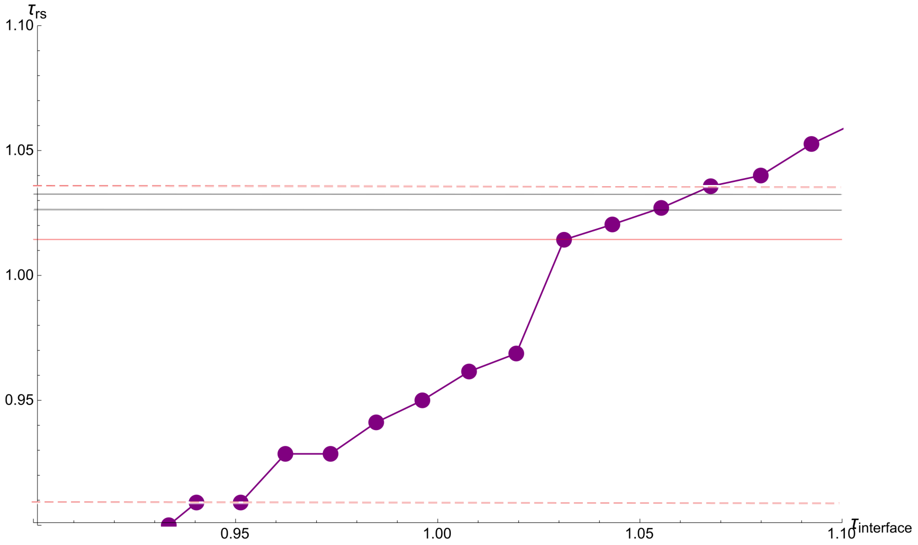

(b) Detailed view of Fig. 3.22d.

Figure 3.34

ι_{rs}	Continued fraction representation
1.0261666790.....	1, 38, 4, 1, 1, 1, 1, 1, 1, 1, 1, 1, 1, 1, 1, 1, 1, 1, 1, 1, 2, 2, 1
1.0324160690.....	1, 30, 1, 5, 1, 1, 1, 1, 1, 1, 1, 1, 1, 1, 1, 1, 1, 1, 1, 1, 1, 2, 11, 1, 2

Table 3.4: Irrational approximations in the $\iota = 0.909091 - 1.03571$ range, marked as horizontal black lines in Fig. 3.34b.

approximations in any given ι range. However, one immediately sees the computational cost of obtaining irrational approximations from the difference in $\Delta\iota$ required to obtain just two ι_{rs} irrational approximations via a simple Mathematica function. As $\Delta\iota$ also translates to wavenumber resolution, the calculation time to obtain minimum λ will undoubtably increase if precise irrational approximations are of interest.

Furthermore, the irrational approximations found with Greene's Theorem is not an input variable to study minimum and marginal λ, rather a naturally occurring system output. This is in contrast to other literature studying the robustness of flux surfaces, e.g. McGann et al. [32], Hudson [24] which require a prescribed ι as a variable input.

In summary, Greene's theorem allows the identification of irrational approximations and estimation of required wavenumber resolution for any given set of real numbers, but the required wavenumber resolution to achieve precise irrational approximations demands a sharp increase in computational time. However, as Greene's Theorem is based upon high-order rationals to locate irrational approximations, it can be cautiously concluded that the current method of identifying high-order rationals from the ι_{rs} characteristics via plateau transitions as implemented in Section 3.5.3 and 3.5.4 is sufficient to guide further study of resonant surfaces with irrational rotational transforms upon minimum λ in a plasma-vacuum slab (see Chapter 4).

3.7 Singularities of λ

In this Section we study the behaviour of λ with multiple resonances within the plasma region as previously introduced in Section 3.4; this is achieved by plotting λ with respect to an appropriately large range of μ as in Fig. 3.35. A periodic pattern emerges, along with points of λ singularities.

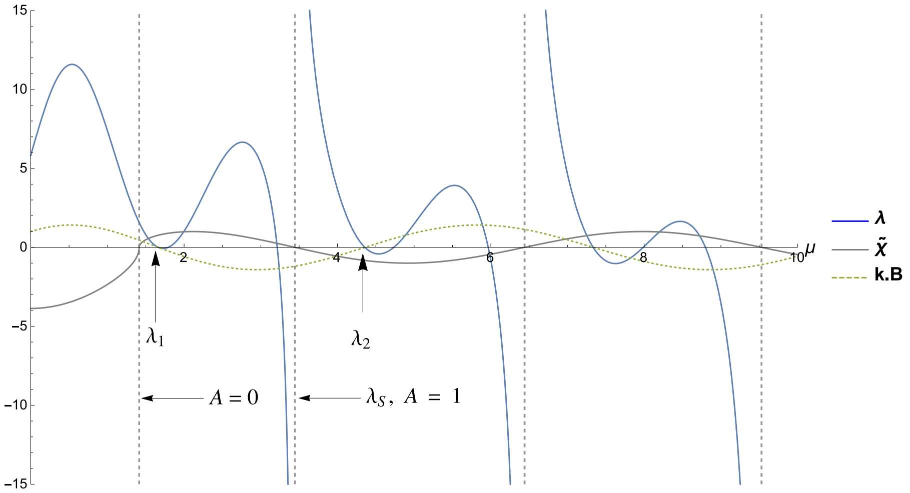

Figure 3.35: Functions λ, $\tilde{\chi}(x_{\text{rs}} \to 1)$, and $\boldsymbol{k} \cdot \boldsymbol{B}$ plotted over μ for $\kappa = 1, m = 1, N_A = 1$, and $\theta = -\cot^{-1}\frac{\mu}{2}$, with marked points of intersection with the x-axis.

We focus our attention to the region of μ denoted by $\lambda_1 - \lambda_2$ in Fig. 3.35 as this region is where the first instances of instabilities and singularities start to develop along the x-axis, and also observe that it is the first region of magnetic field reversal, $\boldsymbol{B}$.

The variable $\tilde{\chi}(x_{\text{rs}} \to 1)$ of $-\Delta'$ is also periodic in nature where $\tilde{\chi} = 0$ occurs at intervals of $\mu = \sqrt{m^2 + \kappa^2 + (A\pi)^2}$, A being an integer constant.[4] Points of $\tilde{\chi} = 0$ are distinguished by vertical grey gridlines in Fig. 3.35; $\tilde{\chi} = 0$ at $A = 0$ is external of the field reversal range and $\tilde{\chi} = 0$ at $A = 1$.

The singularity λ_S at $\mu = \sqrt{m^2 + \kappa^2 + (1\pi)^2}$ is caused by interface perturbations, expounded via the Rayleigh-Ritz method [28] applied upon the Lagrangian of ideal MHD [11]:

$$L = \int \mathcal{L}\, d^3\tau, \tag{3.7}$$

$$\mathcal{L} = \frac{1}{2}\rho(\boldsymbol{v} \cdot \boldsymbol{v}^*) - \frac{p}{\gamma - 1} - \frac{B^2}{2\mu_0}, \tag{3.8}$$

where Eq. (3.8) is the Lagrangian density [29], its terms identified in Eq. (2.1) and also define $\delta^2\mathcal{W}$ (see Section 3.3). The first term represents kinetic energy, where ρ is mass density and $\boldsymbol{v}$ is fluid velocity from the interface perturbation. Rewriting the kinetic energy term with respect to the interface perturbation and ρ as a dyadic tensor [33] produces the following:

---

[4] Although $-\Delta'$ cannot be directly compared to λ in terms of stability in the presence of multiple resonances, its constituent equations can shed light on λ instabilities.

$$\boldsymbol{\rho} = \delta(x-a)\hat{\boldsymbol{x}}\hat{\boldsymbol{x}}, a \text{ is the plasma-vacuum interface,} \tag{3.9}$$

$$\boldsymbol{v} = \frac{d\boldsymbol{\xi}}{dt}, \tag{3.10}$$

$$\boldsymbol{\xi} \propto e^{i\omega t}. \tag{3.11}$$

The choice of $\boldsymbol{\rho}$ has roots in Newcomb's stability analysis [35] (further introduced in Section 3.8) where the radial component of $\boldsymbol{\xi}$[5] is of interest due to the quadratic form of $\mathcal{W}(\xi)$ in Newcomb [35] and thus of L of Eq. (3.7). The kinetic energy term of Eq. (3.7) becomes:

$$\frac{1}{2}\int \rho(\boldsymbol{v}\cdot\boldsymbol{v}^*)\ d^3\tau = \omega^2\ \frac{1}{2}\int |\xi_x|^2\ d^2\sigma, \tag{3.12}$$

where $\omega^2 = \lambda$ and ρ is an arbitrary constant, i.e. 1. In a plasma in which the mass is loaded at the interface and the mass density is unity, $\sqrt{|\lambda|}$ for $\lambda > 0$ is the oscillating frequency, while $\sqrt{|\lambda|}$ for $\lambda < 0$ represents the growth rate. The Rayleigh-Ritz method then produces the following equation from Eq. (3.7):

$$\lambda = \frac{\text{potential energy}}{\text{kinetic energy}}, \tag{3.13}$$

$$\lambda = \mathit{extremum}\frac{\delta^2\mathcal{W}}{\frac{1}{2}\int_{x=a}|\xi_x|^2\ d^2\sigma}. \tag{3.14}$$

The kinetic energy term of interest ξ_x is selected by the dyadic form of ρ; this represents the energy from plasma-vacuum interface perturbations and is described by $\tilde{\chi}(x \to 1)$. The term $\delta^2\mathcal{W}$ is characterised by $\tilde{\chi}(x < 1)$ and so Fig. 3.36 visualises the terms of Eq. (3.14).

The values of $\tilde{\chi}(A = 0) = 0$ and $\tilde{\chi}(x < 1) = 0$ shown in Fig. 3.36a represent $\xi_x = 0$ and $\delta^2\mathcal{W} = 0$ respectively. Therefore λ via Eq. (3.14) is an indeterminate solution and does not result in a singularity at $A = 0$ of Fig. 3.35. Whereas in Fig. 3.36b, $\tilde{\chi}(x_{\text{rs}} \to 1) = 0$ and $\tilde{\chi}(x < 1) \neq 0$ describe $\xi_x = 0$ and $\delta^2\mathcal{W} \neq 0$ respectively; this results in $\lambda_S = \infty$ via Eq. (3.14).

Fig. 3.37 provides a contour plot of λ, varied in terms of κ and μ with $m = 1$, and exhibits the singularity of λ which occurs at $\mu = \sqrt{m^2 + \kappa^2 + (1\pi)^2}$. This equation will be further explored in Section 3.8 as we compare MRxMHD with existing MHD theories.

---

[5] This term ξ_x is identical to ξ_i used in previous Sections, but the radial direction is emphasised here, hence the variable change from i which denotes interface number, to x for the radial component.

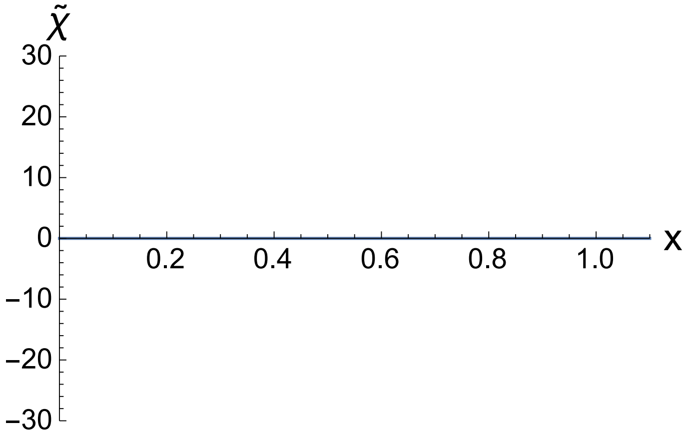

(a) $\tilde{\chi}$ is zero across plasma-vacuum region for $A = 0, \kappa = 1, m = 1, x_{\mathrm{rs}} \to 1$.

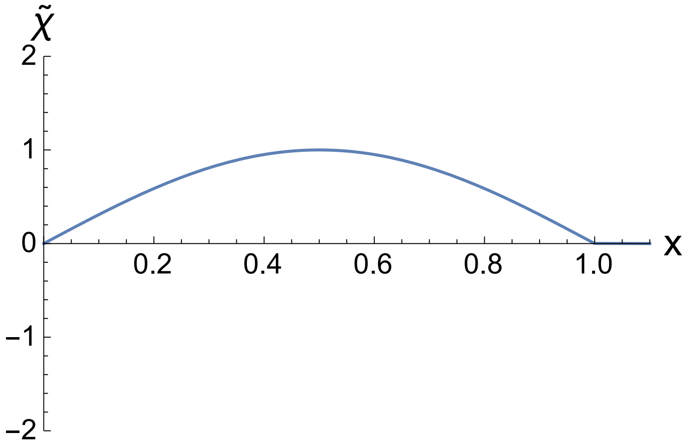

(b) $\tilde{\chi}$ is nonzero across plasma-vacuum region for $A = 1, \kappa = 1, m = 1, x_{\mathrm{rs}} \to 1$.

Figure 3.36: Dependence of $\tilde{\chi}$ on x showing amplitude difference across the plasma-vacuum region for $A = 0$ and $A = 1$ points as marked in Fig. 3.35.

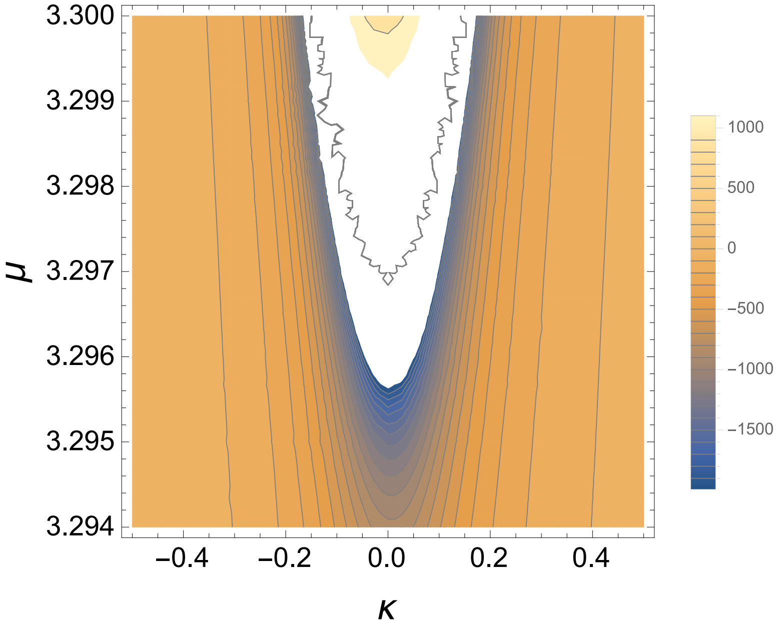

Figure 3.37: Contour plot of λ in the region of λ_S. Due to instabilities approaching $+/-\infty$, the *ContourPlot* function cannot generate contour lines for the white space.

3.8 Comparison of Ideal MHD, Resistive MHD and MRxMHD

3.8.1 Ideal MHD theory

In Goedbloed et al. [14] and Goedbloed and Dagazian [16], the stability of an ideal MHD plasma slab was shown to be dependent upon the inclusion of resistivity to allow for physical perturbations of $\boldsymbol{\xi}$. The work is crucial in demonstrating a unifying relationship between ideal, resistive, and multi-region relaxed MHD.

Starting from the ideal MHD theory perspective, a pressureless plasma slab between two perfectly conducting surfaces is investigated [14, 16]. Minimising the energy, $\mathcal{W}$ with respect to interface perturbations, $\boldsymbol{\xi}$ as prescribed by Newcomb [35] results in a stable $\delta\mathcal{W}$ solution for every $\boldsymbol{\xi}$, implying no instabilities exist.

Reformulating $\delta\mathcal{W}$ in terms of magnetic field perturbations[6], $\boldsymbol{b}$ requires Eq. (2.8) and a Beltrami field $\nabla \times \boldsymbol{B} = \mu \boldsymbol{B}$. The solution for $\boldsymbol{b}$ in an ideal MHD plasma-only slab is shown to be dependent upon $\sqrt{(\mu^2 - k_0^2)}L > A\pi$ which is known as the instability criterion; $k_0^2 = k_y^2 + k_z^2$, from which $k_y = m$ and $k_z = \kappa$ and A is an integer [14, 16]. The wavenumbers can be written as $m = k_0 \cos\phi$ and $\kappa = -k_0 \sin\phi$, with ϕ defined in Fig. 3.38. The plasma region distance between the two perfectly conducting interfaces is L, equal to the plasma-vacuum interface, $x_{\text{interface}}$ in MRxMHD analysis.

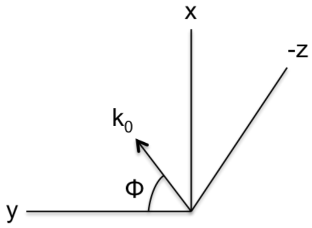

Figure 3.38: Wavenumber directions according to Fig. 2.1 and $\boldsymbol{B}$.

Plotted in Fig. 3.39 is the instability criterion, equivalent to $\mu \geqslant \sqrt{m^2 + \kappa^2 + (A\pi)^2}$, and the λ_S singularity in Section 3.7 occurs when $\mu = \sqrt{m^2 + \kappa^2 + (A\pi)^2}$. Shaded regions of Fig. 3.39 represent regions of instability for different choices of A under the condition $k_0^2 < \mu^2$, but as cautioned by Goedbloed et al. [14] and illustrated in Fig. 3.40, the trial function b_x:

$$b_x = iF\xi_x, \tag{3.15}$$

$$F = \boldsymbol{k} \cdot \boldsymbol{B} = \alpha k_o \cos(\mu x + \theta - \phi), \tag{3.16}$$

of $\delta\mathcal{W}(\boldsymbol{b})$ results in an unphysical ξ_x singularity when $F = 0$. The value of ϕ and θ dictate $F = 0$ radially within the plasma. For instance, $\theta = 0$ and $\phi = \pi/2$ allows $F = 0$ at $x = 0$ and $F = \alpha k_o \sin(\mu x)$. To simplify analysis, all further plots have $\theta = 0$. Hence, the shaded regions of instability shown by Fig. 3.39 are also regions of ξ_x singularity but are incompatible with ideal MHD theory.

---

[6] Variables have been changed to streamline their meaning and usage with MRxMHD equations.

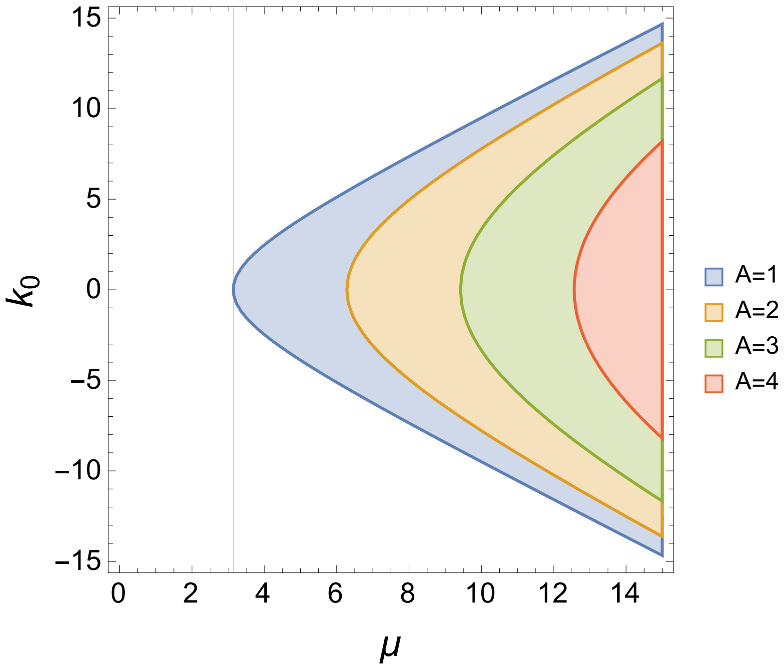

Figure 3.39: Instability criterion diagram for $L = 1$ and varying μ. The vertical gridline labels $\mu = \pi$.

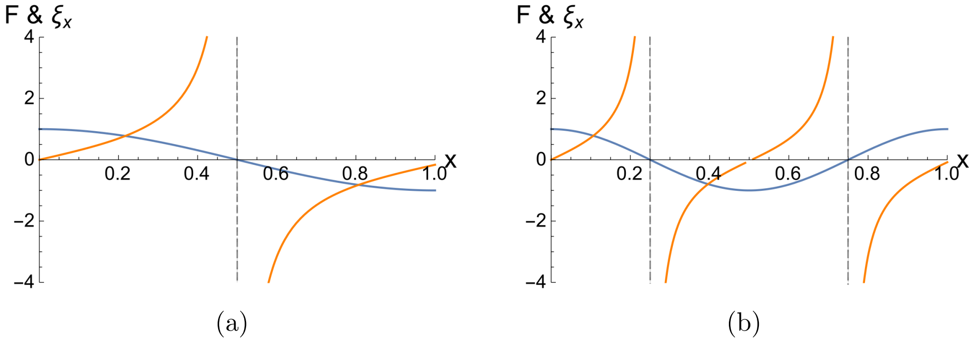

(a)

(b)

Figure 3.40: Behaviour of sinusoidal F (blue line) and ξ_x (orange line) across the plasma region for (a) $A = 1$ or $\mu = \pi$ and (b) $A = 2$ or $\mu = 2\pi$.

3.8.2 Resistive MHD theory

The singular points of ξ_x must be addressed explicitly to make sense of unstable regions in Fig. 3.39, and so we refer back to Newcomb [35]. The singular points of $F = 0$ divide the plasma region into subintervals and so the Euler-Lagrange equation of $\mathcal{W}$, or the Newcomb equation, requires evaluation in these subintervals separately as the equation cannot continue over a singular point[7]. The Frobenius method is then employed to obtain large and small solutions of $\boldsymbol{\xi}$ on either side of the singular point [33]. The separate solutions from the subintervals is analogous to tearing instability theory which requires separate solutions for $\tilde{\chi}$ on both sides of a resonant surface; $\tilde{\chi}''$ is the small solution while $\tilde{\chi}'$ is the large solution.

Indeed, it is shown in Goedbloed et al. [14] that Fig. 3.39 unstable regions can be accessed with tearing instability theory as the displacement becomes physically realisable with resistivity and reconnection across a resonant surface, thus moving away from ideal MHD to resistive MHD theory. As the ideal MHD energy formulation from the Newcomb stability analysis has shown a completely stable system, we will proceed with the tearing instability theory reconstruction in terms of helical flux perturbation for a plasma-only slab. With the boundary conditions of $\tilde{\chi}(x = 0) = 0$ and $\tilde{\chi}(x = x_{\text{wall}}) = 0$, the solution of Eq. (2.19) and (2.15a) for the case of $k_0^2 < \mu^2$, or F_n are:

$$\tilde{\chi} = C \sin(x\sqrt{\mu^2 - m^2 - \kappa^2}), \tag{3.17}$$

$$-\Delta' = \sqrt{-m^2 - \kappa^2 + \mu^2}(-\cot(x\sqrt{-m^2 - \kappa^2 + \mu^2}) + \cot((x - L)\sqrt{-m^2 - \kappa^2 + \mu^2})), \tag{3.18}$$

where C is a coefficient, L is the plasma region length, and $x = x_{\text{rs}} = \frac{L}{2}$. The usage of $x_{\text{rs}} = \frac{L}{2}$ positions $F = 0$ (resonant surface of interest) at the maximum point of b_x as shown in Fig. 14.4 of Goedbloed et al. [14]. Fig. 3.41 plots the comparison between $-\Delta'$ of Goedbloed et al. [14], given as:

$$-\Delta' = 2L\sqrt{\mu^2 - k_0^2}\cot(0.5L\sqrt{\mu^2 - k_0^2}), \tag{3.19}$$

and Eq. (3.18) where the shaded areas represent regions of tearing instability. Both Equations provide identical instability regions and are mathematically equivalent. The regions in Fig. 3.41 are dependent upon $\sqrt{\mu^2 - k_0^2}L \geqslant A\pi$ as $-\Delta'$ changes sign at every $A\pi$, resulting in bands of negative and positive tearing instability regions. The instability criterion of Fig. 3.39 is redefined as a tearing instability diagram from the identical dependence on the stability boundary $\sqrt{\mu^2 - k_0^2}L \geqslant A\pi$ [14].

Fig. 3.41 with its vertical gridlines also show the reduction in L allows for a higher μ limit before the tearing unstable regions are accessed. The plasma length L dictates the μ required for $F = 0$ and the ξ_x singularity to occur radially in the plasma. For $L = 1$ and $\theta = 0$, the tearing instability limit for the plasma-only slab is $\mu > \sqrt{m^2 + \kappa^2 + (\pi)^2}$ (or $\mu > \pi$ for $k_0 \to 0$). In contrast, an $m = 0$ cylindrical, force-free plasma system [13][8] exhibits a symmetrically unstable region for which the tearing instability limit is $\mu > 3.832$.

Fig. 3.42 compares the original plasma-vacuum slab introduced at the beginning of

---

[7] This is further addressed in Dewar et al. [10] which allows continuation of the Newcomb equation across the singularity.

[8] This work also provides the basis of the ideal MHD limit, $\mu > 3.172$, among other works ([39, 41]).

this Thesis to the plasma-only slab in terms of $-\Delta'$. By visual inspection, the regions of tearing instability are qualitatively in agreement for overlapping areas, and some regions that were previously unstable in the plasma-only slab are now stable in the plasma-vacuum slab and vice-versa. The difference is due to the presence of vacuum; the plasma-vacuum interface is not locked to zero, providing additional freedom for the plasma to be unstable. Fig. 3.43 shows the stability region of a plasma-vacuum slab converges to the plasma-only slab stability region by reducing the vacuum region arbitrarily close to the plasma-vacuum interface. This forces $\tilde{\chi}^+$ (Fig. 2.3) at $L = 1$ to be zero, matching boundary conditions imposed on the plasma-only slab.

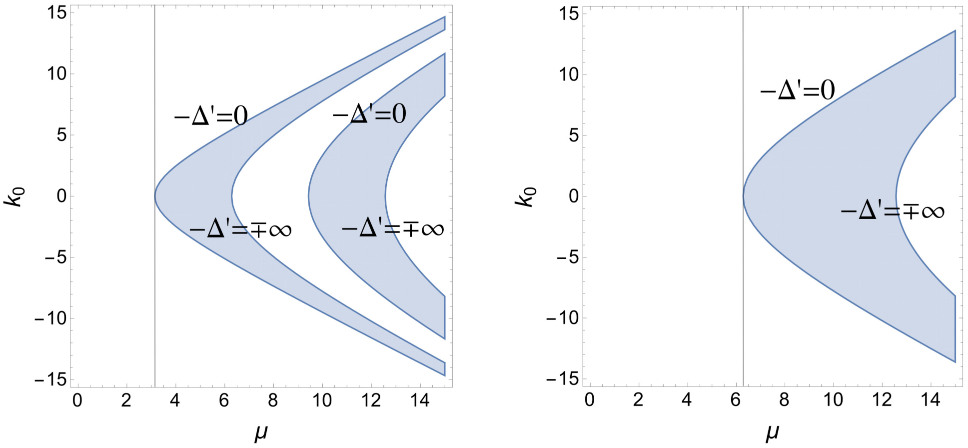

(a) (b)

Figure 3.41: Tearing instability regions for a plasma-only slab with Eq. (3.18) and Eq. (3.19) (a) $L = 1, x_{\mathrm{rs}} \to 0.5$ and (b) $L = 0.5, x_{\mathrm{rs}} \to 0.25$. Both tearing calculations utilise $\phi = \frac{\pi}{2}$ for $F = k_o \sin(\mu x)$. The stability boundaries are marked with their respective $-\Delta'$ values.

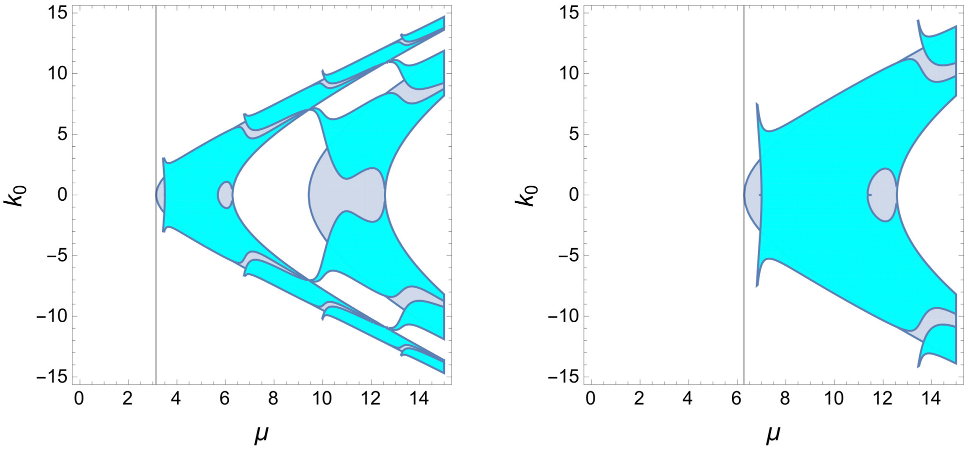

(a) (b)

Figure 3.42: Tearing instability diagrams for plasma-only (grey region) and plasma-vacuum (cyan region) slabs with (a) $L = 1, x_{\mathrm{rs}} \to 0.5$ and (b) $L = 0.5, x_{\mathrm{rs}} \to 0.25$. Both tearing calculations utilise $\phi = \frac{\pi}{2}$ for $F = k_o \sin(\mu x)$.

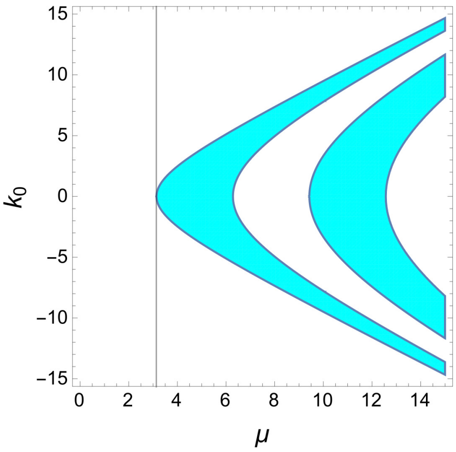

Figure 3.43: The plasma-vacuum stability plot of Fig. 3.42a when $x_{\mathrm{wall}} = 1.0001$. The plasma-vacuum stability plot converges back to the plasma-only stability plot of Fig. 3.41a.

3.8.3 MRxMHD theory

A direct comparison between $-\Delta'$ and MRxMHD for a plasma-only slab is not explored due to MRxMHD boundary conditions. Trivially, the lack of an interface no longer provides the 'multi-region' component required for MRxMHD λ calculations. Indeed, there is no stability problem for MRxMHD with no interface. To circumvent this issue, a MRxMHD plasma-only slab can be constructed by reducing the plasma-vacuum slab vacuum region to zero, resulting in $\lambda \to +\infty$ due to vacuum $\boldsymbol{b}$ boundary conditions of $\boldsymbol{b} = 0$ at the wall, and $\boldsymbol{b} \neq 0$ at the plasma-vacuum interface (see Eq. (2.6c)). With the vacuum region approaching zero, vacuum $\boldsymbol{b}$ becomes infinite to accommodate its boundary conditions, resulting in vacuum $\boldsymbol{B} \cdot \boldsymbol{b} = +\infty$ in Eq. (2.6b), and thus $\lambda = +\infty$. The value of plasma $\boldsymbol{n} \cdot \boldsymbol{b}$ at the MRxMHD interface is also nonzero, inconsistent with boundary conditions imposed on the plasma-only slab perturbed field, and prohibiting comparison of $-\Delta'$ and MRxMHD for a plasma-only slab.

However, the relationship between $-\Delta'$ and λ for a plasma-vacuum slab has been well-analysed in previous Chapters. As both stability models are in agreement for $\mu < \pi$, we proceed to explore the $\mu > \pi$ limit in terms of Newcomb's stability analysis and the $(\mu - k_0)$ stability space for the two models.

In Newcomb [35], the stability analysis for a pressureless plasma-vacuum system is studied; the energy of the vacuum region can be written as:

$$\mathcal{W}_v = \frac{1}{2} \int d^3\tau (\nabla \times \boldsymbol{A})^2, \tag{3.20}$$

with interface boundary condition:

$$\boldsymbol{n} \times \boldsymbol{A} = -(\boldsymbol{n} \cdot \boldsymbol{\xi})\boldsymbol{B}, \tag{3.21}$$

where $\boldsymbol{A} = \boldsymbol{\xi} \times \boldsymbol{B}$, commonly referred to as the *Newcomb gauge* [33] and incorporated into MRxMHD by Eq. (2.8), which defines $\boldsymbol{\xi}$ across both plasma and vacuum regions. With this gauge, $\boldsymbol{\xi}$ is allowed to be singular in MRxMHD as it no longer represents real fluid displacement.

We now proceed to compare λ and $-\Delta'$ in the $\mu > \pi$ limit with the knowledge that $F = \boldsymbol{k} \cdot \boldsymbol{B} = 0$ occurs at $x_{\text{rs}} \to L$, as discussed in previous Sections. Fig. 3.44 shows complete agreement of unstable regions between λ and $-\Delta'$ when $x_{\text{rs}} \to L$; unstable regions begin at $F = 0$ (the vertical region boundaries). Fig. 3.45 also represents a slice of Fig. 3.44a marked by the horizontal black line (note λ_S singularities at $\mu = \sqrt{m^2 + \kappa^2 + (A\pi)^2}$). In Fig. 3.44a, $\mu > \pi$ is the lowest tearing instability limit for the plasma-vacuum slab, while the limit is $\mu > 2\pi$ for Fig. 3.44b.

Firstly, recall that in Section 3.5.1 the initial findings for minimum λ whereby the minimum system energy was unstable for any choice of μ (see Fig. 3.14a). However, this clearly does not hold in Fig. 3.44 where λ is stable in the $\mu < \pi$ region. The physical reasoning is based upon the location of $F = 0$ along the μ-axis dictated by m and κ, or k_o and ϕ (with $\theta = 0$). In the case of Fig. 3.44a, $\phi = \frac{\pi}{2}$ produces the tearing instability limit of $\mu > \pi$. The calculations for minimum λ in Fig. 3.14a utilises a range of m and κ to find a lowest energy state for all μ; λ with fixed ϕ restricts the wavenumber range, i.e. $\phi = \frac{\pi}{2}$ sets $m = 0$, and only some $\lambda(\mu)$ will be unstable.

Secondly, Fig. 3.46 is an overlap of Fig. 3.44a and Fig. 3.42 plasma-vacuum slab $-\Delta'$ stability plots. The stability discrepancy stems from the multiple resonances of the q-profile as discussed in Section 3.4 which begin to occur after the $\mu > \pi$ limit. Only one

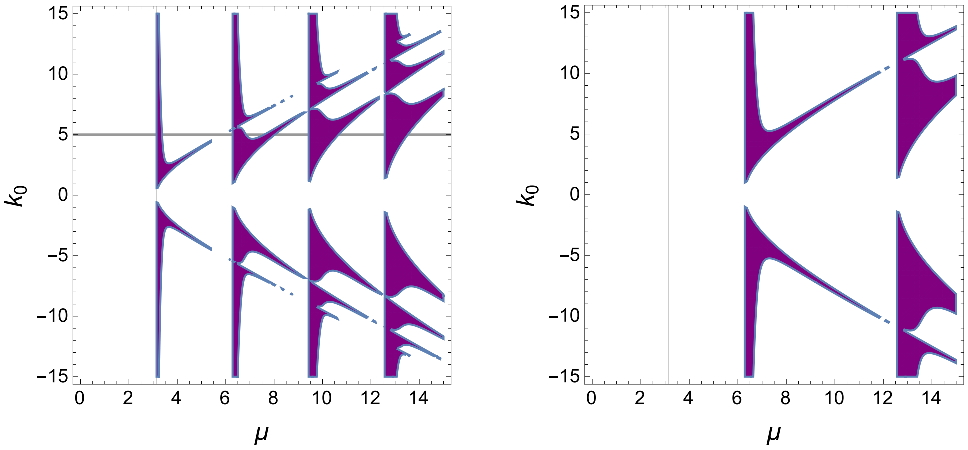

(a) $\lambda(L = 1, \phi = \frac{\pi}{2})$ and $-\Delta'(L = 1, x_{\text{rs}} \to 1, \phi = \frac{\pi}{2})$.

(b) $\lambda(L = 0.5, \phi = \frac{\pi}{2})$ and $-\Delta'(L = 0.5, x_{\text{rs}} \to 0.5, \phi = \frac{\pi}{2})$.

Figure 3.44: Overlapping instability criterion diagrams of λ (purple) and $-\Delta'$ (cyan). λ and $-\Delta'$ show complete agreement of unstable regions.

resonant surface is accounted for the single resonant surface $-\Delta'$ calculation used in this Thesis[9], and so $-\Delta'$ is only in agreement with λ when $x_{\text{rs}} \to L$, as both models exhibit instabilities in this limit (see Figs 3.6 - 3.7).

To understand this finding in depth, the scenario $L = 0.75$, $\phi = \frac{\pi}{4}$ is selected for λ and $-\Delta'$. The choice of ϕ is to ensure m and κ are non-zero values, whereas the special cases $\phi = \pi/2$ or 0 results in either m or κ vanishing. For the $-\Delta'$ model, $L = 0.75$ and two resonant surface choices are selected: $x_{\text{rs}} \to 0.75$, and $x_{\text{rs}} \to 0.25$. Fig. 3.47 shows the latter being the maximum value of F labelled by the dashed vertical gridline.

Fig. 3.48 compares the stability regions of $\lambda(L = 0.75, \phi = \pi/4), -\Delta'(L = 0.75, x_{\text{rs}} \to 0.75, \phi = \frac{\pi}{4})$ and $-\Delta'(L = 0.75, x_{\text{rs}} \to 0.25, \phi = \frac{\pi}{4})$. As expected, the tearing unstable regions match for $x_{\text{rs}} \to L$, and do not match for an x_{rs} further away from L.

Taking a data point specified by the cross in Fig. 3.48b where $\lambda \neq -\Delta'$ provides the variables $\mu = 5$, $k_0 = 1.41421$, in turn represents $m = 1$, $\kappa = -1$. Fig. 3.49 provides a clear interpretation of the stability region discrepancy in terms of resonances from this data point. The sign of λ and $-x_{\text{rs}}\Delta'$ at $x_{\text{rs}} = 0.25$ at the vertical gridline are opposite (λ is stable while $-x_{\text{rs}}\Delta'$ is unstable). This difference is due to the tearing mode treatment which does not consider multiple resonances present for $\mu \geq \pi$ (see Section 3.4). The singularity of $-x_{\text{rs}}\Delta'$ at $x_{\text{rs}} \to 1$ is influenced by the jump in μ across the plasma-vacuum boundary (see Section 3.2), hence always negative and results in identical stability conclusions as λ.

In summary, ideal MHD theory with its singular perturbation $\boldsymbol{\xi}$ in a pressureless plasma slab does not exhibit any ideal nor resistive instabilities. With the introduction of resistive MHD theory, the perturbation is allowed to ‘relax’ and enter a lower energy state which admits resistive instabilities, i.e. tearing instability. The tearing instability criterion of a plasma-vacuum slab smoothly connects with that of a plasma-only slab, with structure differences in stability space (Fig. 3.42) attributed to the existence of the vacuum region. Tearing stability space also only agrees with MRxMHD stability space when the resonant

---

[9] Unless a multi-resonant $-\Delta'$ calculation is utilised.

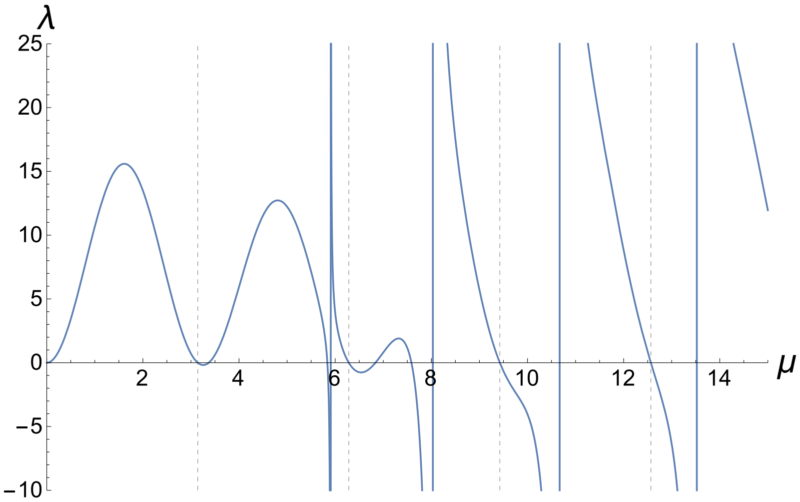

Figure 3.45: The Fig. 3.44a λ slice marked by a horizontal black line, is plotted here across a μ-range, for $m = 0$, $\kappa = 5$ which is equivalent to $k_o = 5, \phi = \pi/2$. The vertical dashed lines label integers of π.

surface of interest is close to $F = 0$ due to the tearing mode treatment not considering multiple resonances. Hence, MRxMHD theory unifies both ideal and resistive MHD perturbations, allowing singular perturbations [33], resistive and ideal instabilities to develop (the latter being dependent upon system geometry). MRxMHD also automatically caters for multiple resonances (in contrast with tearing instability calculations) and provides minimum energy information.

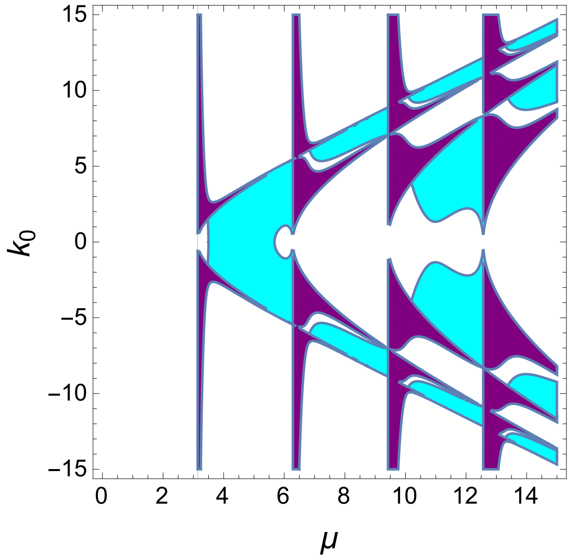

Figure 3.46: Overlapping instability criterion diagrams of $-\Delta'$ for $L = 1, x_{\rm rs} \to 1$ (purple region) and $L = 1, x_{\rm rs} \to 0.5$ (cyan region).

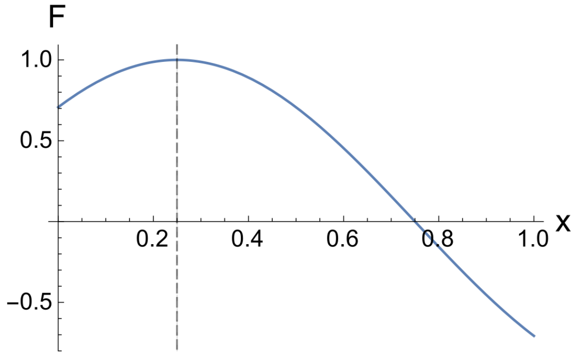

Figure 3.47: The function F across the plasma region for $L = 0.75$, $\phi = \frac{\pi}{4}$, showing the maximum amplitude point labelled by the dashed vertical gridline.

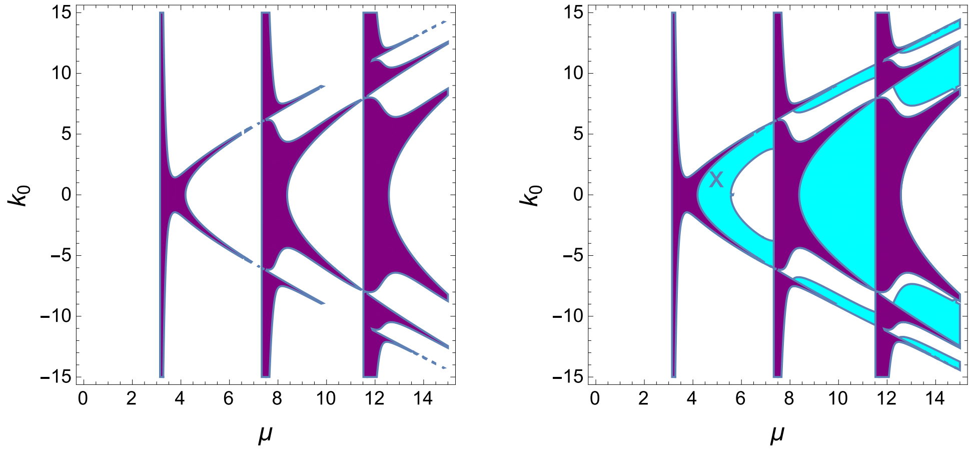

(a) $\lambda(L = 0.75, \phi = \frac{\pi}{4})$ and $-\Delta'(L = 0.75, x_{\rm rs} \to 0.75, \phi = \frac{\pi}{4})$.

(b) $\lambda(L = 0.75, \phi = \frac{\pi}{4})$ and $-\Delta'(L = 0.75, x_{\rm rs} \to 0.25, \phi = \frac{\pi}{4})$.

Figure 3.48: Overlapping instability criterion diagrams of MRxMHD λ (purple) and tearing instability $-\Delta'$ (cyan) for (a) $x_{\rm rs} \to 0.75$ and (b) $x_{\rm rs} \to 0.25$.

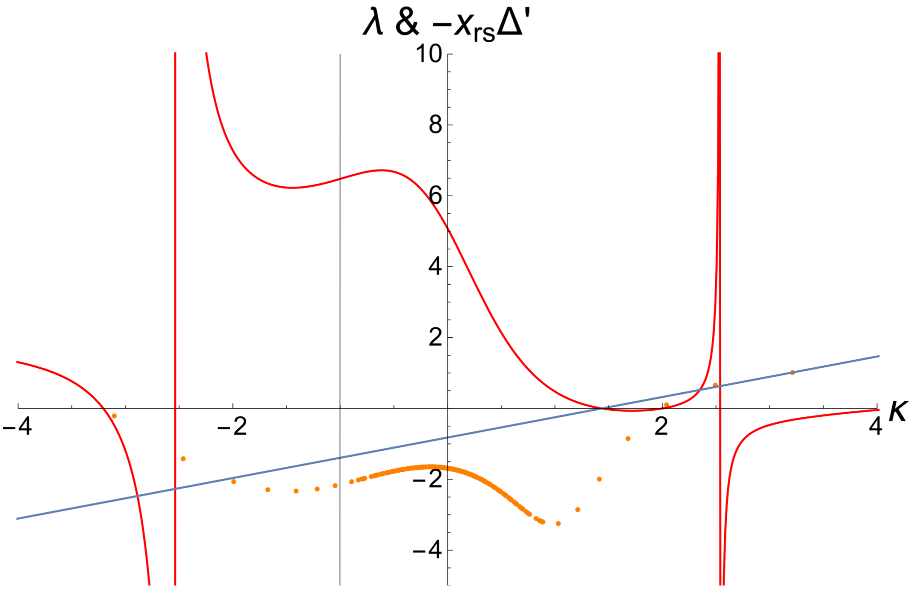

Figure 3.49: The two models, λ and $-\Delta'$ with $m = 1, L = x_{\text{interface}} = 0.75$ over a κ range on the x-axis. The vertical gridline represents $-x_{\text{rs}}\Delta'$ where $x_{\text{rs}} = 0.25$, while the linear blue line is $\boldsymbol{k} \cdot \boldsymbol{B}$ and zero at $x_{\text{rs}} \to 1$.

3.9 Introducing Pressure Effects

The stability conclusion for λ in previous Sections utilise $\beta = 0$ for zero plasma pressure. In Section 3.5.4, it was cited the inclusion of pressure may allow the study of marginal stability at higher wavenumbers. This Section studies the consequence of nonzero plasma pressure on λ, comparing its results to $-\Delta'$ and existing literature for cylindrical, or Bessel function models [21, 25].

We begin by introducing work conducted by Spies and Lortz [36] which encompassed the stability of a relaxed plasma-vacuum slab in terms of μ and wall ratios, or the distance of the vacuum wall from plasma interface. Here, a slab system is stable, $\delta^2\mathcal{W} > 0$ if,

$$\mu_{LN} < \mu < \mu_{SP}, \tag{3.22}$$

$$\tilde{l}\mu L \sin \mu L - 4 \sin \delta \sin(\mu L + \delta) = 0, \tag{3.23}$$

where μ_{LN} is the largest negative root of Eq. (3.23) and μ_{SP} is the smallest positive root, the latter being the root of interest [36]. The variable $\tilde{l}$ is linked to β through the equation $\tilde{l} = l(1-\beta)$ and wall ratio, $l = \frac{(L_x - L)}{L}$ [25]. The vacuum wall distance is L_x, plasma-vacuum interface is L, and the jump in magnetic field rotational transform across the plasma-vacuum interface is δ (see Eq. (2.10))

Fig. 3.50 shows Eq. (3.23) with $\beta = 0$ over a range of l with fixed $L = 1$, and is equivalent to Fig. 1 in Spies and Lortz [36].

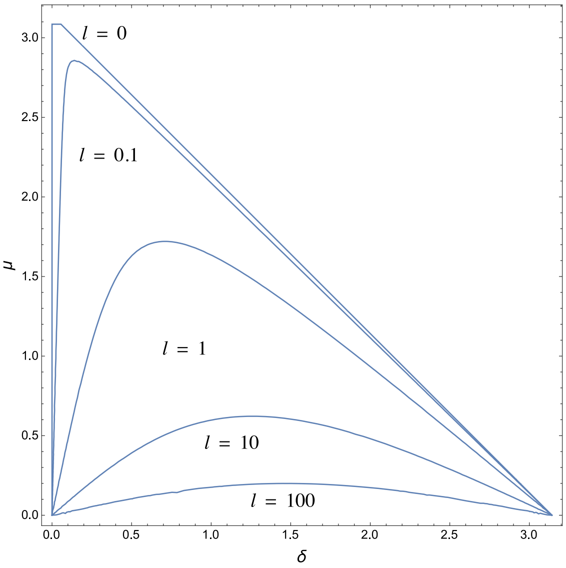

Figure 3.50: Stability space diagram of Eq. (3.23), $\beta = 0$. The region underneath a curve represents stability.

The y-axis of Fig. 3.50 represents μ and the blue curve represents $\mu_{SP}(\delta)$, therefore the region underneath a curve is where $\delta^2\mathcal{W} > 0$. An increase in $\tilde{l}(\beta = 0)$ is akin to moving the vacuum wall location further away from the interface, which results in a reduction of stability space as shown in Fig. 3.50.

With the addition of pressure, and $l = 0.1$ where $L_x = 1.1, L = 1$, Fig. 3.51 illustrates the stability space difference between $\beta = 0$ and $\beta = 0.9$. For $\beta = 0.9$, the stability space has increased and is equivalent to the $l = 0$ curve of Fig. 3.50. This implies that an increase in plasma pressure with fixed vacuum wall correlates to a pressureless plasma slab with a reducing vacuum region, contrary to the Appendix in Kaiser and Uecker [25].

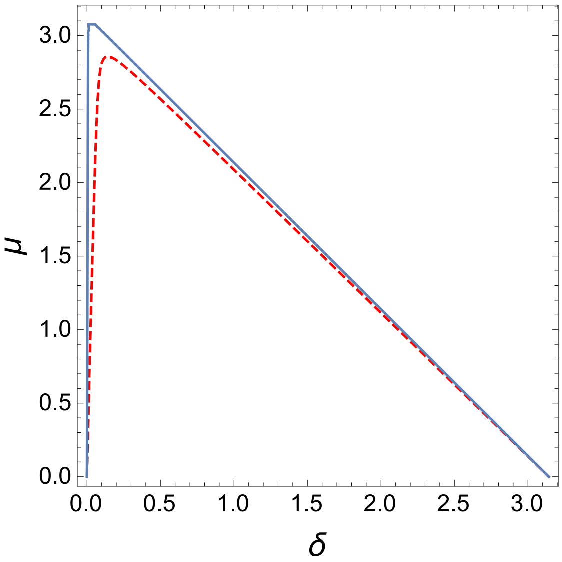

Figure 3.51: Eq. (3.23) for $\beta = 0$ (dashed line) and $\beta = 0.9$ (solid line).

To compare the findings of Eq. (3.23) with MRxMHD λ, recall the pressure jump condition Eq. (2.6b) for nested flux surfaces where $[[p + \frac{1}{2}\boldsymbol{B}^2]]$, and p can be rewritten in terms of β (see Section 2.1). Changes in pressure modifies the magnetic field [42] via,

$$\boldsymbol{J} \times \boldsymbol{B} = \nabla P. \tag{3.24}$$

The term ∇P is constant across a nested flux region in MRxMHD, but a pressure change at the interface of two regions is allowed. The β term also surfaces in Eq. (2.9) and (2.10); nonzero magnetic field strength of $\boldsymbol{B}$ is only dependent on the magnetic field magnitude α, and β via:

$$\boldsymbol{B} = \{0, B_y, B_z\}, \tag{3.25}$$

$$B_P : \pm\alpha, \tag{3.26}$$

$$B_V : \pm\sqrt{\left|\frac{\alpha^2}{1-\beta}\right|}. \tag{3.27}$$

As decreasing l is equivalent to increasing β, Fig. 3.52 presents λ with $\beta = 0$ and three l options. It can be seen that the area of instability over a κ wavenumber range is reduced with lower l. Most importantly, marginal stability $\lambda = 0$ at $\boldsymbol{k} \cdot \boldsymbol{B} = 0$ is unchanged with different wall ratios; $\beta \neq 0$ does not affect the wavenumbers associated with $\lambda = 0$ at $x_{\text{rs}} \to 1$ and this implies there are no pressure-driven instabilities in the slab. Low-order rationals of marginal stability $\lambda = 0$ at $\boldsymbol{k} \cdot \boldsymbol{B} = 0$ (see Section 3.5.4) are therefore unchanged with increasing plasma pressure.

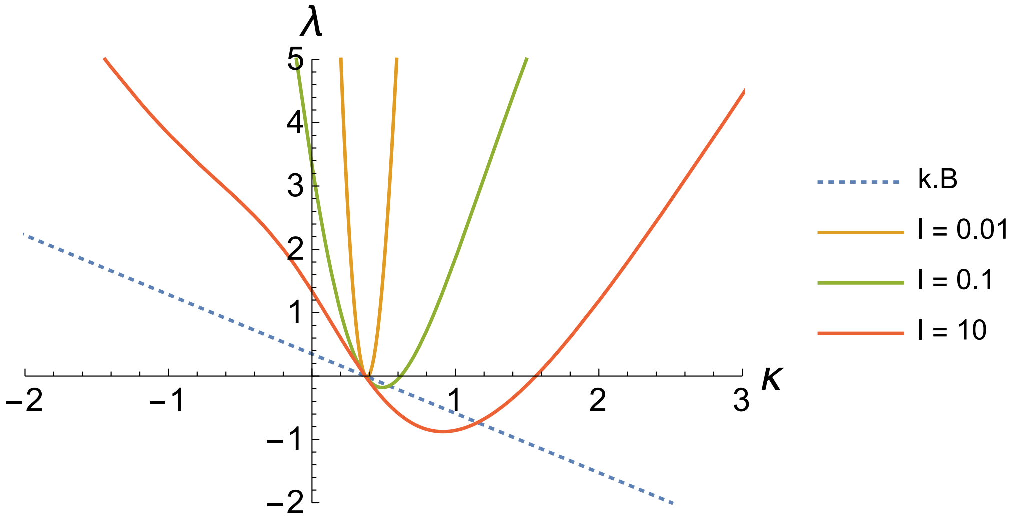

Figure 3.52: Stability of λ with various wall ratios, using $m = 1, \mu = 2, \beta = 0, \delta = 0$, and $\theta = -\cot^{-1}\frac{\mu}{2}$.

Fig. 3.53 also shows the minimum stability of MRxMHD λ across a $(\delta - \mu)$ plane from $\beta = 0 - 0.9$, calculated with the following ranges and resolution; $0 < \delta < 3$ with $\Delta\delta = 0.5$, and $0 < \mu < \pi$ with $\Delta\mu = \frac{\pi}{10}$. The range and step size of wavenumbers are $-20 < m < 20$, and $-20 < \kappa < 20$ with $\Delta m = 0.3, \Delta\kappa = 0.3$. The lowest values of λ, or minimum λ are collected and provide data points for marginal stability boundaries to be plotted via Mathematica's *InterpolationOrder* function[10] in Fig. 3.53.

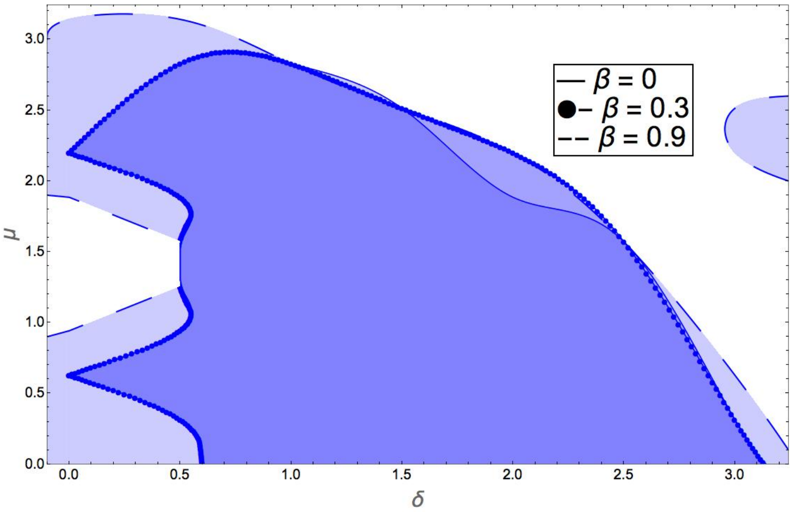

Figure 3.53: Stability space diagram for minimum λ with varying β. Shaded areas represent stability for $\beta = 0, 0.3, 0.9$.

---

[10] The function provides a more accurate representation of stability regions with increasing data points or higher resolution.

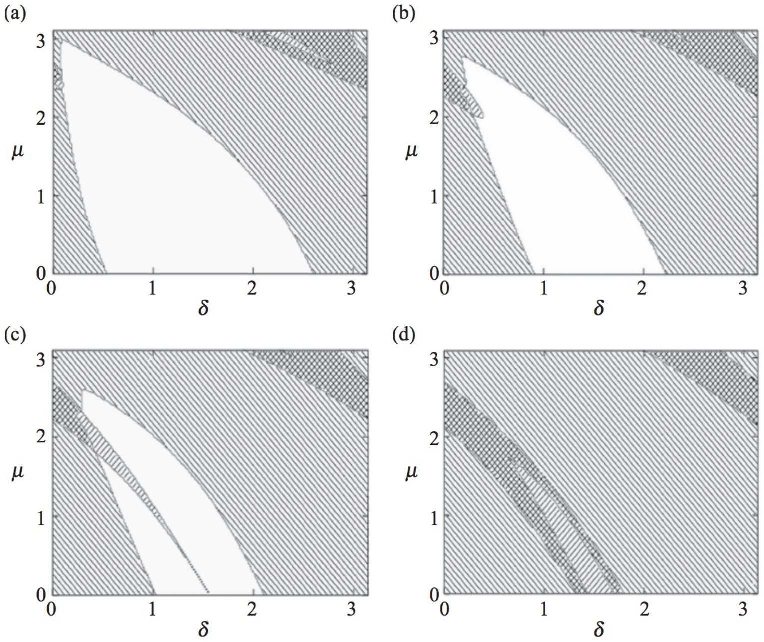

Figure 3.54: Unstable region (shaded) in the $(\delta - \mu)$ plane for a cylindrical model, with fixed vacuum wall distance and (a) $\beta = 0.1$, (b) $\beta = 0.4$, (c) $\beta = 0.5$, (d) $\beta = 0.8$. Kaiser, R. and Uecker, H., 2004. Relaxed plasma–vacuum states in cylinders. *The Quarterly Journal of Mechanics and Applied Mathematics*, 57, 1 (2004), 1–17.

By visual inspection of Fig. 3.53, the stable region of λ across the $(\delta - \mu)$ plane expands with increasing β. This is in contrast to the stability space diagram of cylindrical models where increasing β resulted in a rapidly decreasing stability space, characterised by the total loss of a stable region by $\beta = 0.8$ in Fig. 3 of Kaiser and Uecker [25], reproduced here in Fig. 3.54. From $\beta = 0 - 0.9$, the stability space of λ in Fig. 3.53 has increased in size without a rapid change as depicted in the cylindrical stability space diagrams and corroborated by the relatively small stability space increase between $\beta = 0$ and $\beta = 0.9$ of Fig. 3.51. It is also noted from Fig. 3.53 and Fig. 3.54 that $\delta > 0$ allows for the minimum energy of the slab model to enter a stable region, and is no longer tearing unstable for all non-zero μ as stated in Section 3.5.1.

The increase in stability space of Fig. 3.53 stems from the MRxMHD Eq. (2.6b) where $\xi_i^* \xi_i [[B(\boldsymbol{n} \cdot \nabla) B)]]$ is dependent upon the curvature vector of field lines, or magnetic curvature, $\boldsymbol{\kappa} = (\hat{\boldsymbol{b}} \cdot \nabla)\hat{\boldsymbol{b}}$, where $\hat{\boldsymbol{b}} = \frac{\boldsymbol{B}}{B}$ [36, 43]. For a slab model, $\xi_i^* \xi_i [[B(\boldsymbol{n} \cdot \nabla) B)]] = 0$ as magnetic curvature is zero, simplifying Eq. (2.6b) to $\xi_i^* [[\boldsymbol{B} \cdot \boldsymbol{b}]] - \lambda \xi_i^* \xi_i = 0$. The vacuum region magnetic energy increases with $\beta > 0$ while the plasma region magnetic energy remains unchanged (see Eq. (2.10)), resulting in increased total system energy. However, this is not the case for a cylindrical model where curvature is nonzero. If the component of $\boldsymbol{\kappa}$ normal to the plasma-vacuum interface $(\boldsymbol{\kappa} \cdot \boldsymbol{n})$ is negative, the curvature is directed to the plasma interior. This is termed an unfavourable curvature and becomes a destabilising source, which may result in pressure-driven instabilities [4].

In summary, contrary to cylindrical plasma systems, the presence of non-zero pressure increases plasma-vacuum slab stability due to the lack of field curvature in a slab. Marginal stability for $x_{\mathrm{rs}} \to 1$ does not experience a change in wavenumber conditions, owing to the lack of pressure-driven instabilities without field curvature.

3.9.1 Discrepancy between tearing instability and MRxMHD models for nonzero pressure scenarios

A discrepancy was discovered between the variational method and the tearing mode calculations used for a Bessel model [22] with the inclusion of pressure terms. This discrepancy is confirmed in our working for the Cartesian model by varying the β and α value used in both λ and $-\Delta'$ models for Fig. 3.55. With the $\beta = 0$ case, both models wholly agree, but with increasing β, Fig. 3.55a and Fig. 3.55b show marginal stability discrepancy, observed by the position of $\lambda(\beta = 0.8) = 0$ with respect to the zero crossing of $-x_{\rm rs}\Delta'$. Both models experience a change of marginal stability points along the x-axis, but the rate of change is not identical with varying β.

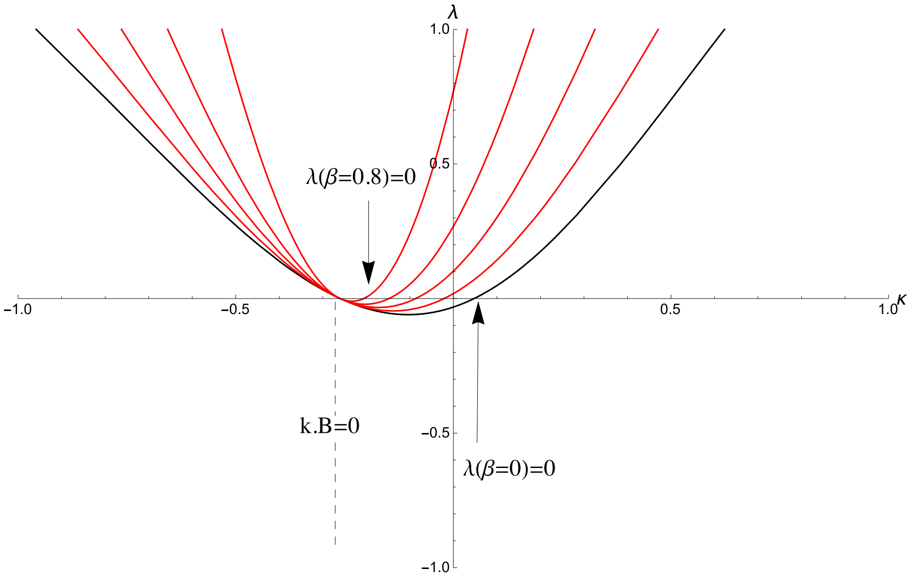

(a) λ with increasing pressure for $\mu = 2.5$. Black line uses $\beta = 0$, increasing $\beta = 0.2, 0.4, 0.6, 0.8$ from right to left.

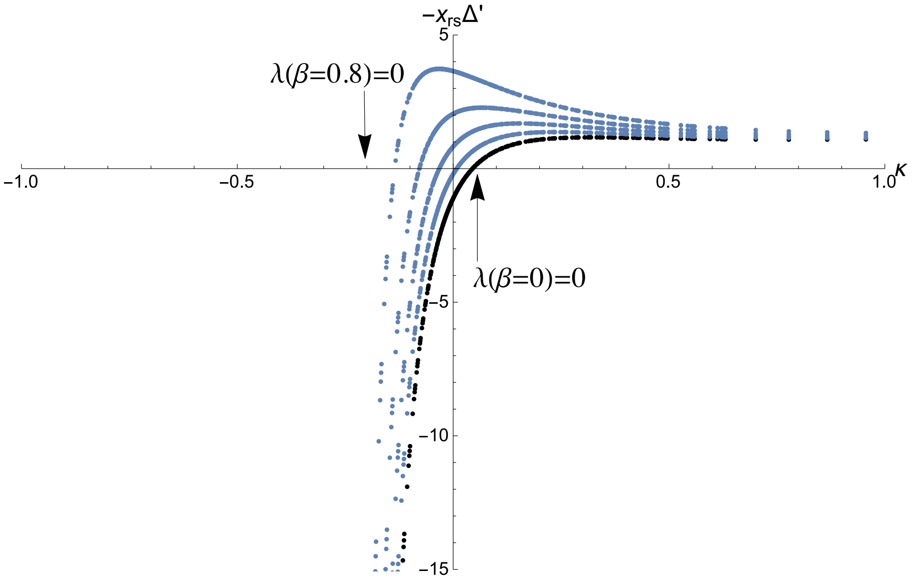

(b) $-x_{\rm rs}\Delta'$ with increasing pressure for $\mu = 2.5$. Black line uses $\beta = 0$, increasing $\beta = 0.2, 0.4, 0.6, 0.8$ from right to left.

Figure 3.55

Assessment of this discrepancy firstly investigates pressure jump condition effects, Eq. (2.3) on tearing instability flux perturbations. As expected, Fig. 3.56 shows the plasma region flux perturbations are sensitive to pressure change, while the pressureless vacuum region flux perturbations are unchanged. The plasma-vacuum interface is at $x = 1$, and $x_{\text{rs}} = 0.9$.

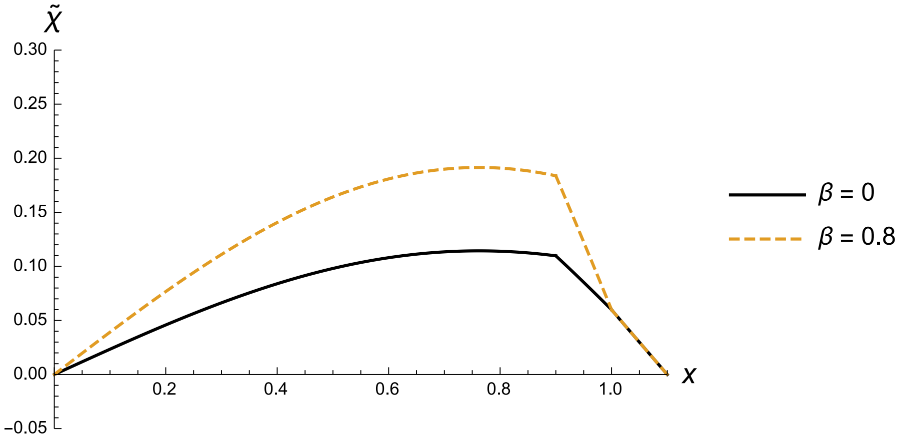

Figure 3.56: $\tilde{\chi}$ across the plasma and vacuum regions with $\kappa = 1, m = 1, \mu = 2.5$. Non-zero β has affected $\tilde{\chi}$ amplitude change only in the plasma region as expected.

Fig. 3.57 shows the disparity between λ and $-x_{\text{rs}}\Delta'$ for $\beta = 0.8$, where the zero crossings for both models are no longer identical as seen for $\beta = 0$ scenarios. While $\lambda = 0, x_{\text{rs}} < 1$ no longer corresponds to $-x_{\text{rs}}\Delta'$ for $\beta \neq 0$, the wavenumbers associated with $\lambda = 0, x_{\text{rs}} \to 1$ are unaffected by changes in pressure, as previously shown by Fig. 3.52, and is also displayed in Fig. 3.55a with the location of $\boldsymbol{k}\cdot\boldsymbol{B} = 0$ along the wavenumber axis.

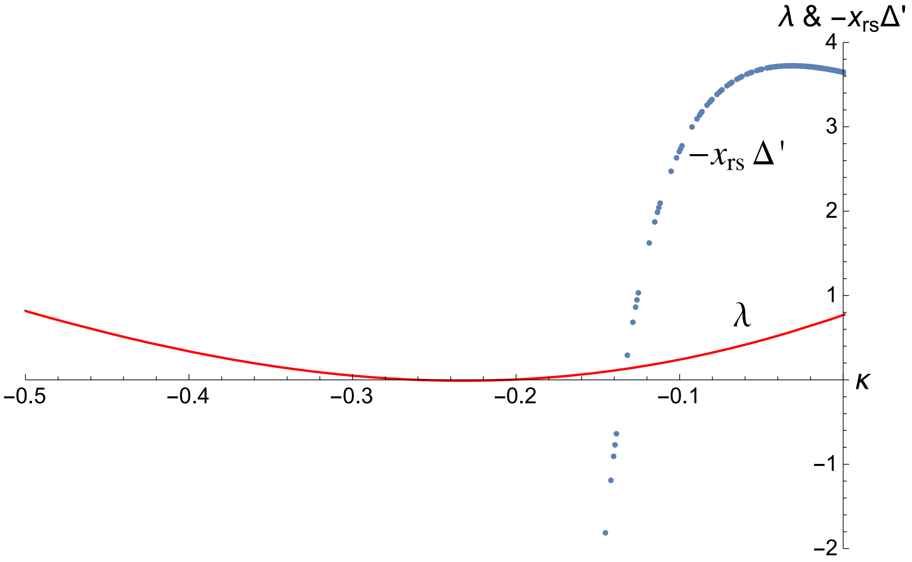

Figure 3.57: λ and $-x_{\text{rs}}\Delta'$ zero crossings for $\beta = 0.8$ are no longer in agreement.

The discrepancy may lie in Taylor's relaxation theory, in which kinetic energy terms have been removed [36]. Efforts to incorporate kinetic energy into the MRxMHD framework have been outlined in Section 4.1.

Chapter 4

Conclusions and Future Work

In conclusion, the work in this Thesis has demonstrated MRxMHD theory is equivalent to tearing instability theory for pressureless plasma-volume regions in terms of wavenumbers and system stability. The method outlined in the Results present a general numerical option for identifying high and low-order rationals to measure rotational transforms in a slab model, along with its effect upon λ.

To summarise the main findings in this Thesis:

1. The minimised energy state of a plasma-vacuum slab system is driven by resonant surfaces within the plasma and not purely by interface rotational transforms; resonant surfaces with large rational denominators and numerators p and q, or high-order rationals contribute to λ values which signify system stability. Therefore, MRxMHD has inbuilt tearing instability information such as the existence of magnetic islands.

2. Marginally stable solutions of $\lambda = 0$ at $\boldsymbol{k} \cdot \boldsymbol{B} = 0$, or $\boldsymbol{b} = 0$ have the smallest p and q integers, which are the lowest-order rationals and represent the interface rotational transform. In contrast, a 3D equilibria requires irrational interface rotational transforms (see Section 1.2).

3. Both variational and tearing instability methods are in agreement for zero-pressure scenarios, and instabilities in the slab model are identified as tearing instabilities only (no ideal instabilities exist). In contrast, a cylindrical model exhibits tearing and ideal instabilities [13].

4. Resistive MHD and MRxMHD stability values may differ, due to multiple resonances in the plasma region of the slab not accounted for by resistive MHD calculations. The fine structures found in the plasma-vacuum slab stability space (Fig. 3.42) are attributed to the existence of the vacuum region which provides more freedom for plasma-vacuum interface perturbation. Via resistive MHD calculations, plasma-vacuum stability space converges back into a plasma-only stability space when vacuum region is decreased (Fig. 3.43). MRxMHD unifies existing ideal MHD and resistive MHD theories, additionally providing minimum energy information and automatically catering for multiple resonances.

5. The inclusion of plasma pressure has resulted in increasing system stability for a slab model which is opposite to the decreasing stability effect of pressure in a cylindrical model; this result is attributed to the lack of curvature in the slab model. The interface rotational transform of an MRxMHD plasma-vacuum slab is unaffected by pressure change.

6. The discrepancy between MRxMHD and tearing instability theory previously found for a cylindrical model in Hole et al. [22] has been confirmed to also exist in a plasma-vacuum slab model. Future work is required to resolve the discrepancy between the MRxMHD variational method and the tearing mode instability method when pressure is non-zero, possibly via a new method prescribed by Dewar et al. [11] in which pressure perturbations contribute to ω^2, or λ.

These findings may have applications to the SPEC code and other research based upon energy minimisation and flux surface rationality. Marginal stability of MRxMHD is possible at plasma-vacuum interface of low-order rotational transforms.

4.1 Future work: A Lagrangian Variational Principle Method

In Dewar et al. [11], a new approach to the variational principle was put forth, utilising a Lagrangian formulation of MRxMHD to provide Euler-Lagrange equations and boundary conditions. Kinetic energy terms have been incorporated into MRxMHD dynamical equations and provides a new physical normalisation. The authors show that within relaxation regions, MRxMHD supports steady flows and sound waves due to the decoupling of $\boldsymbol{v}$ from $\boldsymbol{B}$. A sample of the work is presented as follows:

A Lagrangian density, $\boldsymbol{L}$ is posited for a plasma system, where $\boldsymbol{L}$ = Kinetic Energy - Thermal Energy - Magnetic Energy + Fixed Helicity:

$$\boldsymbol{L} = \frac{\rho \boldsymbol{v}\cdot\boldsymbol{v}}{2} - \frac{p}{\gamma-1} - \frac{\boldsymbol{B}\cdot\boldsymbol{B}}{2\mu_o} + \frac{\boldsymbol{A}\cdot\boldsymbol{B}}{2\mu_o}\mu. \tag{4.1}$$

The Euler-Lagrange equations from the first variation of Eq. (4.1) are:

$$p = \tau_i \rho, \tag{4.2}$$

$$\rho\frac{d\boldsymbol{v}}{dt} = -\nabla p, \tag{4.3}$$

$$\left[\left[p + \frac{B^2}{2\mu_0}\right]\right] = 0, \tag{4.4}$$

$$\frac{d\rho}{dt} = -\rho\nabla\cdot\boldsymbol{v}, \tag{4.5}$$

where τ_i is identified as the temperature of a plasma region, ρ is mass density, with all other variables identical to Eq. (2.1). Velocity, $\boldsymbol{v}$ and mass density, ρ can be written as plane wave solutions, i.e.:

$$\boldsymbol{v_1} = \dot{\xi} e^{i(\boldsymbol{kx}-\omega t)}, \tag{4.6}$$

for a 3-dimensional Cartesian frame, where $\boldsymbol{k} = k_x + k_y + k_z$ and $\boldsymbol{x} = x\boldsymbol{e_x} + y\boldsymbol{e_y} + z\boldsymbol{e_z}$. The term ω represents oscillations in a system, t represents a point in time, and $\dot{\xi}$ represents complex amplitude for interface displacement. Substituting Eq. (4.2) into (4.3), and linearising (4.3) and (4.5) gives the first order terms,

$$\rho \frac{\partial \boldsymbol{v_1}}{\partial t} = -\tau_i \frac{\partial \rho_1}{\partial \boldsymbol{x}}, \tag{4.7}$$

$$\frac{\partial \rho_1}{\partial t} = -\rho_0 \frac{\partial \boldsymbol{v_1}}{\partial \boldsymbol{x}}. \tag{4.8}$$

Eq. (4.7) and (4.8) are multiplied with $\frac{\partial}{\partial t}$ and $\frac{\partial}{\partial x}$ respectively:

$$\rho \frac{\partial^2 \boldsymbol{v_1}}{\partial t^2} = -\tau_i \frac{\partial \rho_1}{\partial \boldsymbol{x} \partial t}, \tag{4.9}$$

$$\frac{\partial \rho_1}{\partial \boldsymbol{x} \partial t} = -\rho_0 \frac{\partial^2 \boldsymbol{v_1}}{\partial \boldsymbol{x}^2}, \tag{4.10}$$

and substituting Eq. (4.10) into (4.9) with $\frac{\partial}{\partial t} = -i\omega$ and $\frac{\partial}{\partial \boldsymbol{x}} = i\boldsymbol{k}$ results in the dispersion relation $\omega = \sqrt{\tau}\boldsymbol{k}$, where $\tau = C_s^2$, the isothermal sound speed, and $\boldsymbol{k}$ is a wavenumber vector.

The boundary conditions are $v_1\boldsymbol{e_x} = 0$ at the edge of the plasma and at the vacuum wall, similar to the boundary conditions of the variational method and tearing mode calculations. At the interface, $v_1\boldsymbol{e_x} = \dot{\xi}$.

By linearising the interface condition Eq. (4.4), the eigenvalue ω is consequently a function of pressure perturbations. As $\omega^2 = \lambda$ [4], stability information is gained for comparison against the variational method we have used in this body of work. For positive λ, ω is real and the system is stable, while negative λ results in imaginary ω. In the latter instance, it is expected that the wavenumber k_x is generally complex, and corresponds to radially evanescent or growing waves. This new Lagrangian variational principle method may resolve the difference between tearing and variational calculations in a non-zero pressure system as a suggestion for future work, as Taylor's relaxation theory does not account for thermal and kinetic energy [36].

4.2 Other Avenues for Future Work

Other avenues for future work also include plotting Poincaré plots with the high and low-order rationals of rotational transforms across the plasma-vacuum slab; the formation of magnetic islands or chaotic regions around low order rationals within the plasma region is an expected outcome from this exercise [32]. It may also show that the high-order rationals are sufficient as irrational approximations in terms of flux surface robustness against perturbations.

The slab model may also be modified to include gravitational forces as a way of simulating field curvature found in cylindrical models, as described for ideal MHD with interchange instabilities in plane geometry [4]. This work may allow an analytical link of slab results to cylindrical model results, as well as investigating the effects of gravitational and interchange instabilities on the flux surface rotational transform in the MRxMHD framework.

An interesting branch of study encountered during the course of this Thesis was the theory behind the Devil's Staircase and its emergence in dynamical systems, condensed matter physics [27], and of course, plasma physics [7]. The Devil's Staircase along with its rationals may have deeper connotations for chaotic regions and resonances in plasma systems. As chaotic regions may exist in tokamaks and stellarators, the resonant surface rotational transforms of these models with respect to minimum energy may be worth analysing for any relationship to a Devil's Staircase.

Bibliography

[1] SPEC description. `http://theorycodes.pppl.wikispaces.net/SPEC`. Accessed: 2016-06-15.

[2] ALFVÉN, H., 1942. Existence of electromagnetic-hydrodynamic waves. *Nature*, 150 (1942), 405–406.

[3] BONFIGLIO, D.; ESCANDE, D.; ZANCA, P.; AND CAPPELLO, S., 2011. Necessary criterion for magnetic field reversal in the reversed-field pinch. *Nuclear Fusion*, 51, 6 (2011), 063016.

[4] BOYD, T. AND SANDERSON, J., 2003. *The Physics of Plasmas*. Cambridge University Press. ISBN 9780521459129. URL `https://books.google.com.au/books?id=bAmqvuGTUJ4C`.

[5] CELLETTI, A., 2010. *Stability and Chaos in Celestial Mechanics*. Springer Praxis Books. Springer Berlin Heidelberg. ISBN 9783540851462. URL `https://books.google.com.au/books?id=gcU5Fj9uy7IC`.

[6] CHANDRASEKHAR, S. AND KENDALL, P. C., 1957. On Force-Free Magnetic Fields. 126 (Sep. 1957), 457. doi: 10.1086/146413.

[7] CHEN, Q., 1987. Area as a devil's staircase in twist maps. *Physics Letters A*, 123, 9 (1987), 444 – 450. doi: http://dx.doi.org/10.1016/0375-9601(87)90343-4. URL `http://www.sciencedirect.com/science/article/pii/0375960187903434`.

[8] DEIFT, P.; LEVERMORE, C.; AND WAYNE, C. *Dynamical Systems and Probabilistic Methods in Partial Differential Equations: 1994 Summer Seminar on Dynamical Systems and Probabilistic Methods for Nonlinear Waves, June 20-July 1, 1994, MSRI, Berkeley, CA*. Lectures in applied mathematics. American Mathematical Soc. ISBN 9780821897003. URL `https://books.google.com.au/books?id=M2zJfdWzRBMC`.

[9] DENNIS, G. R.; HUDSON, S. R.; DEWAR, R. L.; AND HOLE, M. J., 2014. Multi-region relaxed magnetohydrodynamics with flow. *Physics of Plasmas*, 21, 4 (Apr. 2014), 042501. doi: 10.1063/1.4870008.

[10] DEWAR, R. L.; MILLS, R.; AND HOLE, M. J., 2009. MHD memes. *Journal of Physics Conference Series*, 169, 1 (May 2009), 012004. doi: 10.1088/1742-6596/169/1/012004.

[11] DEWAR, R. L.; YOSHIDA, Z.; BHATTACHARJEE, A.; AND HUDSON, S. R., 2015. Variational formulation of relaxed and multi-region relaxed magnetohydrodynamics. *ArXiv e-prints*, (Sep. 2015).

[12] FINN, J. M.; NEBEL, R.; AND BATHKE, C., 1992. Single and multiple helicity ohmic states in reversed field pinches. *Physics of Fluids B*, 4, 5 (1992).

[13] Gibson, R. and Whiteman, K., 1968. Tearing mode instability in the bessel function model. *Plasma Physics*, 10, 12 (1968), 1101.

[14] Goedbloed, J.; Keppens, R.; and Poedts, S., 2010. *Advanced Magnetohydrodynamics: With Applications to Laboratory and Astrophysical Plasmas.* Cambridge University Press. ISBN 9781139487283. URL `https://books.google.com.au/books?id=wHDyYpsqp04C`.

[15] Goedbloed, J. and Poedts, S., 2004. *Principles of Magnetohydrodynamics: With Applications to Laboratory and Astrophysical Plasmas.* Cambridge University Press. ISBN 9780521626071. URL `https://books.google.com.au/books?id=FvM6rMJob-cC`.

[16] Goedbloed, J. P. and Dagazian, R. Y., 1971. Kinks and tearing modes in simple configurations. *Phys. Rev. A*, 4 (Oct 1971), 1554–1560. doi: 10.1103/PhysRevA.4.1554. URL `http://link.aps.org/doi/10.1103/PhysRevA.4.1554`.

[17] Goldston, R. and Rutherford, P., 1995. *Introduction to Plasma Physics.* Institute of Physics Publishing.

[18] Hartmann, D., 2004. Stellarators. *Fusion Science and Technology*, 45, 2T (2004), 64–76.

[19] Hassani, S., 2011. *From Atoms to Galaxies: A Conceptual Physics Approach to Scientific Awareness.* Taylor & Francis. ISBN 9781439808504. URL `https://books.google.com.au/books?id=oypZ_a9pqdsC`.

[20] Helander, P.; Beidler, C.; Bird, T.; Drevlak, M.; Feng, Y.; Hatzky, R.; Jenko, F.; Kleiber, R.; Proll, J.; Turkin, Y.; et al., 2012. Stellarator and tokamak plasmas: a comparison. *Plasma Physics and Controlled Fusion*, 54, 12 (2012), 124009.

[21] Hole, M.; Hudson, S.; and Dewar, R., 2007. Equilibria and stability in partially relaxed plasma-vacuum systems. *Nuclear Fusion*, 47, 8 (2007), 746.

[22] Hole, M.; Mills, R.; Hudson, S.; and Dewar, R., 2009. Relaxed mhd states of a multiple region plasma. *Nuclear Fusion*, 49, 6 (2009), 065019.

[23] Hudson, S., 2004. Destruction of invariant surfaces and magnetic coordinates for perturbed magnetic fields. *Physics of Plasmas (1994-present)*, 11, 2 (2004), 677–685.

[24] Hudson, S., 2006. Calculation of cantori for hamiltonian flows. *Physical Review E*, 74, 5 (2006), 056203.

[25] Kaiser, R. and Uecker, H., 2004. Relaxed plasma–vacuum states in cylinders. *The Quarterly Journal of Mechanics and Applied Mathematics*, 57, 1 (2004), 1–17.

[26] Kappraff, J., 2002. *A Guided Tour Through Nature, Myth, and Number.* World Scientific.

[27] Lam, L., 1998. *Nonlinear Physics for Beginners: Fractals, Chaos, Solitons, Pattern Formation, Cellular Automata, Complex Systems.* World Scientific. ISBN 9789810201418. URL `https://books.google.com.au/books?id=pfEATHvL-uYC`.

[28] Leissa, A. W., 2005. The historical bases of the rayleigh and ritz methods. *Journal of Sound and Vibration*, 287, 4 (2005), 961–978.

[29] Lifshits, A., 2012. *Magnetohydrodynamics and Spectral Theory*. Developments in Electromagnetic Theory and Applications. Springer Netherlands. ISBN 9789400925618. URL `https://books.google.com.au/books?id=ivfnCAAAQBAJ`.

[30] Loizu, J.; Hudson, S.; Bhattacharjee, A.; and Helander, P., 2015. Magnetic islands and singular currents at rational surfaces in three-dimensional magnetohydrodynamic equilibria. *Physics of Plasmas (1994-present)*, 22, 2 (2015), 022501.

[31] Marek-Crnjac, L., 2009. A short history of fractal-cantorian space-time. *Chaos, Solitons & Fractals*, 41, 5 (2009), 2697–2705.

[32] McGann, M.; Hudson, S.; Dewar, R.; and Von Nessi, G., 2010. Hamilton–jacobi theory for continuation of magnetic field across a toroidal surface supporting a plasma pressure discontinuity. *Physics Letters A*, 374, 33 (2010), 3308–3314.

[33] Mills, R.; Hole, M.; and Dewar, R., 2009. Magnetohydrodynamic stability of plasmas with ideal and relaxed regions. *Journal of Plasma Physics*, 75, 05 (2009), 637–659.

[34] Nazikian, R.; Paz-Soldan, C.; Callen, J. D.; deGrassie, J. S.; Eldon, D.; Evans, T. E.; Ferraro, N. M.; Grierson, B. A.; Groebner, R. J.; Haskey, S. R.; Hegna, C. C.; King, J. D.; Logan, N. C.; McKee, G. R.; Moyer, R. A.; Okabayashi, M.; Orlov, D. M.; Osborne, T. H.; Park, J.-K.; Rhodes, T. L.; Shafer, M. W.; Snyder, P. B.; Solomon, W. M.; Strait, E. J.; and Wade, M. R., 2015. Pedestal bifurcation and resonant field penetration at the threshold of edge-localized mode suppression in the diii-d tokamak. *Phys. Rev. Lett.*, 114 (Mar 2015), 105002. doi: 10.1103/PhysRevLett.114.105002. URL `http://link.aps.org/doi/10.1103/PhysRevLett.114.105002`.

[35] Newcomb, W. A., 1960. Hydromagnetic stability of a diffuse linear pinch. *Annals of Physics*, 10, 2 (1960), 232–267.

[36] Spies, G. and Lortz, D., 2001. Relaxed plasma-vacuum systems. *Physics of Plasmas*, 8, 8 (2001), 3652–3663. doi: 10.1063/1.1383286.

[37] Tassi, E.; Hastie, R.; and Porcelli, F., 2007. Linear stability analysis of force-free equilibria close to taylor relaxed states. *Physics of Plasmas (1994-present)*, 14, 9 (2007), 092109.

[38] Taylor, J. B., 1974. Relaxation of toroidal plasma and generation of reverse magnetic fields. *Phys. Rev. Lett.*, 33 (Nov 1974), 1139–1141. doi: 10.1103/PhysRevLett.33.1139. URL `http://link.aps.org/doi/10.1103/PhysRevLett.33.1139`.

[39] Taylor, J. B., 1974. Relaxation of toroidal plasma and generation of reverse magnetic fields. *Phys. Rev. Lett.*, 33 (Nov 1974), 1139–1141. doi: 10.1103/PhysRevLett.33.1139. URL `http://link.aps.org/doi/10.1103/PhysRevLett.33.1139`.

[40] Unterberg, E. *Accesing High Normalized Current in an Ultra-low-aspect-ratio Torus*. ISBN 9780549385226.

[41] Voslamber, D. and Callebaut, D., 1962. Stability of force-free magnetic fields. *Physical Review*, 128, 5 (1962), 2016.

[42] Wesson, J. and Campbell, D., 2011. *Tokamaks*. International Series of Monographs on Physics. OUP Oxford. ISBN 9780199592234. URL `https://books.google.com.au/books?id=BH9vx-iDI74C`.

[43] White, R., 2013. *The Theory of Toroidally Confined Plasmas*. Imperial College Press. ISBN 9781783263639. URL `https://books.google.com.au/books?id=cgOAngEACAAJ`.